MEASUREMENT OF THE B QUARK AND B MESON CROSS-SECTIONS IN PROTON-ANTIPROTON COLLISIONS AT 1.8 TEV USING FULLY RECONSTRUCTED DECAYS

A Thesis

Submitted to the Faculty

of

Purdue University

by

Mark W. Bailey

In Partial Fulfillment of the

Requirements for the Degree

of

Doctor of Philosophy

May 1994

AAD6440

ACKNOWLEDGMENTS

I would like to express respect and gratitude to my major professor, Art Garfinkel, both for his help in conducting the research described in this thesis and for sharing many useful physics insights, as well as for his good advice in other matters. I would also like to thank Slawek Tkaczyk for being a good ally and mentor, both in hardware DAQ tribulations and in the physics analysis. I also am thankful to Daniela Bortoletto and Alvin Laasanen for many useful discussions on this analysis. I genuinely appreciate the support all of you have given me.

TABLE OF CONTENTS

Page

LIST OF TABLES v

LIST OF FIGURES vi

ABSTRACT xi

1. INTRODUCTION 1

2. THEORETICAL FRAMEWORK 3

3. THE COLLIDER DETECTOR AT FERMILAB 16

3.1 Central Tracking Chamber 17
3.2 Central Fast Track Processor 21
3.3 Silicon Vertex Detector 22
3.4 VTX Detector 26
3.5 Central Muon Detector 26

4. DATA SAMPLE SELECTION 32

4.1 Di-muon J/ψ Trigger 32
4.2 SVX Tracking Algorithm 34
4.3 Offline J/ψ Selection 35
4.4 B Meson Selection Requirements 37
4.5 Integrated Luminosity 40
4.6 Observed B Meson Signals 41

5. DETECTOR ACCEPTANCE AND RECONSTRUCTION EFFICIENCY 44

5.1 The CDF Detector Acceptance for B mesons 44
5.1.1 Monte Carlo Event Generator 44
5.1.2 Detector Simulation 46
5.1.3 J/ψ Trigger Simulation 46
5.1.4 Combined Geometrical Acceptance and Trigger Efficiency . . 49
5.2 Efficiency of the Offline Selection Requirements 53
5.2.1 J/ψ Selection Requirements 53
5.2.2 Other Offline Selection Requirements 55
5.3 Tracking Efficiencies 65
5.3.1 Online Tracking Efficiency 65

Page

5.3.2 CTC Offline Tracking Efficiency 68
5.3.3 SVX Tracking Efficiency 69
5.3.4 Muon Chamber Tracking Efficiency 79
5.4 Summary of the Reconstruction Efficiencies 83

6. CROSS-SECTION CALCULATION 86

6.1 Total Cross-section 86
6.2 Differential Cross-section 96

BIBLIOGRAPHY 106

VITA 109

LIST OF TABLES

Table Page

5.1 SVX individual layer hit efficiencies from muon tracks for which the other three layers had hits. 72

5.2 Probability for an SVX track to be found with 2, 3, or 4 hits, calculated from the individual layer hit efficiencies. 72

5.3 Summary of reconstruction efficiencies for B meson reconstructed using the $B^{\pm} \rightarrow J/\psi K^{\pm}$ and $B^0 \rightarrow J/\psi K^{*0}$ decay channels. 84

5.4 Summary of systematic uncertainties in the cross-section measured using the $B^{\pm} \rightarrow J/\psi K^{\pm}$ and $B^0 \rightarrow J/\psi K^{*0}$ decay channels. 85

6.1 B^- meson integrated cross-sections, for selected values of p_{Tmin}. 87

6.2 $\overline{B^0}$ meson integrated cross-sections, for selected values of p_{Tmin}. 93

6.3 Correspondence between $p_{Tmin}(b)$ for the b quark and $p_{Tmin}(B)$ for the B meson. 93

6.4 b quark integrated cross-sections using the $B^{\pm} \rightarrow J/\psi K^{\pm}$ decay channel, for selected values of p_{Tmin}. 94

6.5 b quark integrated cross-sections using the $B^0 \rightarrow J/\psi K^{*0}$ decay channel, for selected values of p_{Tmin}. 96

6.6 Mean B meson p_T for the five transverse momentum ranges used to determine the differential cross-section 102

6.7 B^- meson differential cross-sections using the $B^{\pm} \rightarrow J/\psi K^{\pm}$ decay channel. 103

6.8 $\overline{B^0}$ meson differential cross-sections using the $\overline{B^0} \rightarrow J/\psi \overline{K^{*0}}$ decay channel. 103

LIST OF FIGURES

Figure Page

2.1 QCD representation of inclusive heavy quark production via hadron collisions. 4

2.2 Feynman diagrams for a) leading order, and b) next-leading-order parton-parton interactions. 5

2.3 Feynman diagrams for gluon-splitting and flavor-excitation interactions. 6

2.4 Quantum electrodynamic description of lepton-proton deep inelastic scattering. 7

2.5 Dependence of the theoretical b quark cross-section on the choice of the renormalization scale, μ. 9

2.6 J/ψ production diagram used to determine the gluon structure function in lepton-proton scattering experiments. 10

2.7 Dependence of the theoretical cross-section on choice of proton structure function set. 11

2.8 Structure function measurements from the H1 and ZEUS detectors at the HERA *ep* collider, compared to the MRS D_0' and D_-' predictions. 12

2.9 Preliminary CDF measurement of the same-side/opposite-side dijet ratio, compared to the MRS D_0' and D_-' predictions. 13

2.10 Peterson parameterization of the b quark fragmentation function, D(z), for $\epsilon = 0.006$. 15

3.1 Cross-section view of the CDF detector layout for the 1992-93 collider run. 18

3.2 A CTC endplate, showing the location of the axial and stereo drift cells. 19

3.3 Particle drift trajectories in the CTC, with respect to the radial direction indicated by the arrow. 20

Figure Page

3.4 A set of roads recognized by the CFT for a 5-GeV/c track, defined by a hit in the outermost superlayer. 22

3.5 A cut-away view of the SVX detector, showing ladder arrangement and the support frame. 23

3.6 An SVX ladder, composed of 3 silicon microstrip detectors, readout electronics, and support structure. 24

3.7 Cross-section of the VTX detector, which exposes the 4-cm wide drift regions, and the larger inner radius near $z = 0$ which accomodates the SVX detector. 27

3.8 Location of the central muon chambers within a central calorimeter wedge. 28

3.9 Cross-section of a central muon chamber, as viewed along the beamline direction. 29

3.10 Charged particle trajectory in the transverse plane. The inner circle of radius L represents the CTC within the magnetic field region. 31

4.1 Muon transverse momentum distributions. The top plot is for the lower p_T muon from each muon pair, while the bottom plot is for the higher p_T muon. 36

4.2 J/ψ invariant mass distribution reconstructed from the di-muon decay channel. 38

4.3 $B^{\pm}$ invariant mass distribution reconstructed from the decay $B^{\pm} \rightarrow J/\psi K^{\pm}$ 42

4.4 B^0 invariant mass distribution reconstructed from the decay $B^0 \rightarrow J/\psi K^{*0}$ 43

5.1 Level 1 muon trigger efficiency versus transverse momentum. The right-most bin contains all data for the p_T range 6.75 to 10.0 GeV/c. 48

5.2 Level 2 muon trigger efficiency. The low statistical error on the points is due to the fact that the entire J/ψ data sample is used for the measurement. 50

Figure Page

5.3 Combined acceptance and dimuon trigger efficiency for J/ψ versus the transverse momentum of the B^- meson. 52

5.4 Combined acceptance and dimuon trigger efficiency for J/ψ versus the transverse momentum of the $\overline{B^0}$ meson. 53

5.5 J/ψ mass width for the three tracking combinations (a) SVX-SVX, (b) SVX-CTC, and (c) CTC-CTC. 54

5.6 $(m_{\mu\mu} - m_{J/\psi})/\delta_m$ for the three tracking combinations (a) SVX-SVX, (b) SVX-CTC, and (c) CTC-CTC. 56

5.7 $c\tau$ resolution for sideband regions for the four possible tracking combinations. 58

5.8 $c\tau$ cut efficiency for $B^{\pm}$ lifetime of 483 ± 50 μm as a function of the $c\tau$ resolution. 60

5.9 $c\tau$ cut efficiency for B^0 lifetime of 471 ± 59 μm as a function of the $c\tau$ resolution. 61

5.10 Vertex χ^2 confidence level distribution for the $B^{\pm}$ candidates passing all selection cuts. 62

5.11 B mass distribution, for B candidates which have a vertex χ^2 confidence level > 0.005. 63

5.12 B mass distribution, for B candidates which have a vertex χ^2 confidence level < 0.005. 64

5.13 J/ψ mass distribution, without imposing a cut on the J/ψ vertex χ^2 confidence level. 66

5.14 J/ψ mass distribution, for J/ψ candidates which have a vertex χ^2 confidence level > 0.005. 67

5.15 SVX layer efficiencies for muons from J/ψ versus the transverse momentum of the muon. 70

5.16 Layer hit efficiencies vs ϕ, for tracks passing the z fiducial cut. 73

5.17 Layer hit efficiencies vs z-intercept of the track with the layer. 74

Figure Page

5.18 SVX tracking efficiency for muons from J/ψ. Fit is made to a constant efficiency, between muon transverse momenta of 1 and 12 GeV/c. . . . 75

5.19 SVX tracking efficiency for muons from J/ψ versus L_{xy}, the decay length projected onto the p_T vector. 77

5.20 Number of muons per pair forming a J/ψ candidate for which an SVX track is found. 78

5.21 Movement of J/ψ vertex when SVX information for one or both muon(s) is dropped. 80

5.22 Movement of B vertex when SVX information is dropped for one, two, or all three tracks. 81

5.23 Muon and kaon relative transverse momentum change between SVX and CTC tracking. 82

6.1 $B^{\pm}$ invariant mass distribution for $p_T(B^{\pm}) \geq 9.0$ GeV/c and the results of the fit. 88

6.2 $B^{\pm}$ invariant mass distribution for $p_T(B^{\pm}) \geq 12.0$ GeV/c and the results of the fit. 89

6.3 $B^{\pm}$ invariant mass distribution for $p_T(B^{\pm}) \geq 15.0$ GeV/c and the results of the fit. 90

6.4 B^0 invariant mass distribution for $p_T(B^0) \geq 9.0$ GeV/c and the results of the fit. 91

6.5 B^0 invariant mass distribution for $p_T(B^0) \geq 12.0$ GeV/c and the results of the fit. 92

6.6 b quark integrated cross-section measurements, compared to the next-to-leading order QCD prediction. 95

6.7 $B^{\pm}$ invariant mass distribution for $6.0 < p_T(B^{\pm}) < 9.0$ GeV/c and the results of the fit. 97

6.8 $B^{\pm}$ invariant mass distribution for $9.0 < p_T(B^{\pm}) < 12.0$ GeV/c and the results of the fit. 98

Figure Page

6.9 $B^{\pm}$ invariant mass distribution for $12.0 < p_T(B^{\pm}) < 15.0$ GeV/c and the results of the fit. 99

6.10 B^0 invariant mass distribution for $7.0 < p_T(B^0) < 11.0$ GeV/c and the results of the fit. 100

6.11 B^0 invariant mass distribution for $11.0 < p_T(B^0) < 14.0$ GeV/c and the results of the fit. 101

6.12 B meson differential cross-section measurements, compared to the theoretical prediction. 105

ABSTRACT

Bailey, Mark W. Ph.D., Purdue University, May 1994. Measurement of the b Quark and B Meson Cross-Sections in Proton-Antiproton Collisions at 1.8 TeV Using Fully Reconstructed Decays. Major Professor: Arthur F. Garfinkel.

This thesis describes the measurement of the b quark and B meson production cross-sections at the Collider Detector at Fermilab, using the exclusive decays $B^{\pm} \rightarrow J/\psi K^{\pm}$ and $B^0 \rightarrow J/\psi K^{*0}$. The cross-section for b quarks produced at transverse momentum greater than 7.5 GeV/c is found to be $5.92 \pm 0.78 \pm 1.24$ μb. For B mesons with transverse momentum greater than 6.0 GeV/c, the cross-section is found to be $2.06 \pm 0.27 \pm 0.43$ μb for the B^+ and $2.22 \pm 0.44 \pm 0.64$ μb for the B^0. Differential cross-sections are also presented.

1. INTRODUCTION

The study of heavy flavor production at the highest center-of-mass energy currently available provides the opportunity to check the accuracy of the perturbative expansion of the cross-section in terms of α_s, the QCD coupling constant. There exist QCD calculations at next-to-leading order ($\mathcal{O}(\alpha_s{}^3)$) [1, 2] which, along with recent preliminary parameterizations of the parton distribution functions down to $x \approx 10^{-5}$ [3], predict the b quark cross-section. It is necessary to show that these predictions provide an adequate description of the cross-section at 1.8 TeV before they can be confidently extrapolated to higher energies or more exotic phenomena.

In this thesis the measurement of the B meson and b quark cross-sections in $p\bar{p}$ collisions at $\sqrt{s} = 1.8$ TeV will be described. The analysis uses the exclusive decay channels $B^{\pm} \rightarrow J/\psi K^{\pm}$ and $B^0 \rightarrow J/\psi K^{*0}$, with $J/\psi \rightarrow \mu^+\mu^-$ and $K^{*0} \rightarrow K^+\pi^-$, and their charge conjugates. The data sample used represents an integrated luminosity of $19.4 \pm 0.8 pb^{-1}$ collected by the Collider Detector at Fermilab (CDF) during the 1992-93 Tevatron collider run. A description of the relevant CDF components will be presented. A description of the trigger requirements, which are based on the detection of the two muons from the J/ψ decay, will also be described, along with the sources of contributions to the systematic uncertainty in the measurement.

CDF has measured the integrated cross-sections using these decay channels before [4, 5], but this analysis measures the B cross-section at lower momentum and with higher statistics. It also includes the first measurement of the B meson

differential cross-section as a function of the transverse momentum. The cross-sections will be compared with QCD theoretical prediction.

2. THEORETICAL FRAMEWORK

The study of B quark production in hadron colliders is important for the design of CP violation experiments and is of great theoretical interest because it provides the opportunity to gauge the precision with which quantum chromodynamics (QCD) can be used to calculate the observed cross-sections and hence predict cross-sections for top production.

Figure 2.1 represents the QCD description of heavy quark production. Parton 1 from hadron A, carrying momentum fraction, x_1, of hadron A interacts with parton 2 from hadron B, with momentum fraction x_2. The interaction results in a heavy quark of momentum, k, as well as additional partons. The theoretical calculations that will be described in this chapter are for the specific case that the outgoing quark is a bottom quark.

The shaded region in figure 2.1 is used to indicate all the possible interactions between parton 1 and 2. The QCD calculation of the cross-section, $\hat{\sigma}$, for parton 1 to interact with parton 2 can be thought of as a sum of Feynman diagrams representing increasing numbers of partons involved in the interaction. A selection of these is shown in figure 2.2. Other diagrams involved can be found by crossing the initial or final state partons.

The diagrams in figure 2.2a represent the $2 \rightarrow 2$ or "leading order" interactions. Figure 2.2b shows some of the $2 \rightarrow 3$ or "next-to-leading order" interactions, which consist of diagrams from figure 2.2a with initial or final state gluon emission. In figure 2.3 are the diagrams for the "gluon-splitting" and "flavor-excitation"

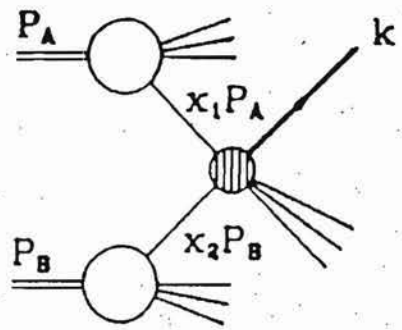

Figure 2.1

QCD representation of inclusive heavy quark production via hadron collisions.

interactions which first enter at next-to-leading order.

The QCD coupling constant, α_s, enters at each vertex in the diagrams. So the contributions to $\hat{\sigma}$ of the Feynman diagrams in figure 2.2a are proportional to α_s^2, while those in figures 2.2b and 2.3 are proportional to α_s^3. Contributions proportional to higher powers of α_s are represented by increasingly complex Feynman diagrams, but currently the calculations of $\hat{\sigma}$ for b quark production have only included the leading order and next-to-leading order diagrams. The value of $\hat{\sigma}$ can thus be taken as a power series expansion in terms of α_s. The accuracy of the estimate for $\hat{\sigma}$ obtained by truncation of the series at $\mathcal{O}(\alpha_s^3)$ directly depends on the scale of the interaction, which determines the size of α_s.

The one-particle inclusive differential cross-section is found by integrating $Ed^3\hat{\sigma}/dk^3$ over all momentum fractions, and summing over all types of partons,

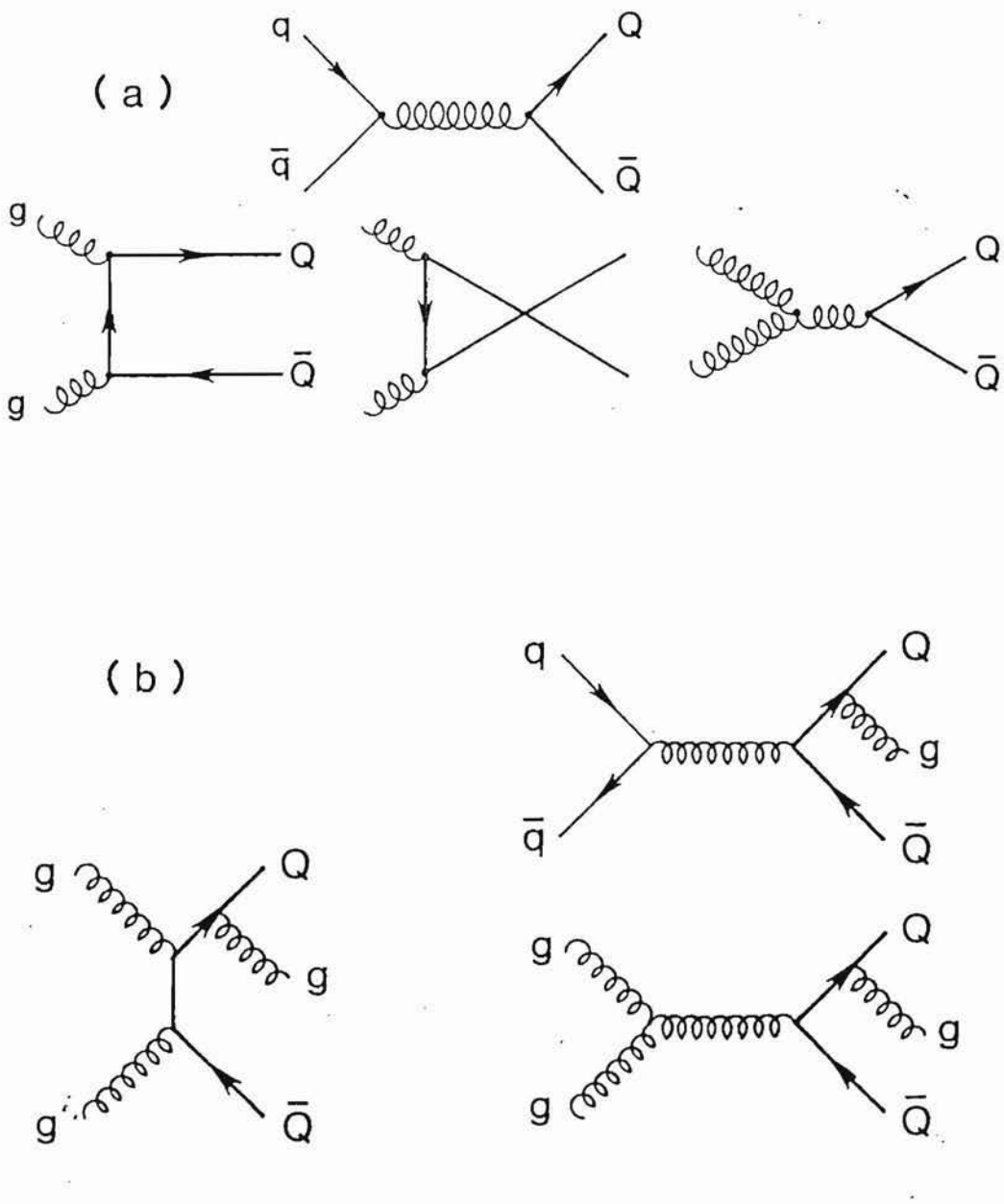

Figure 2.2

Feynman diagrams for a) leading order, and b) next-leading-order parton-parton interactions.

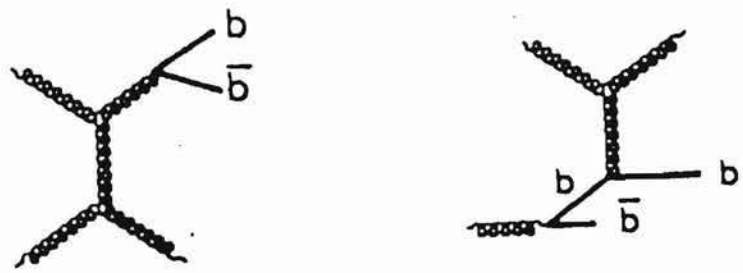

Figure 2.3

Feynman diagrams for gluon-splitting and flavor-excitation interactions.

according to the following equation:

$$\frac{Ed^3\sigma}{dk^3} = \sum_{i,j} \int dx_A dx_B \frac{Ed^3\hat{\sigma}}{dk^3} F_i^A F_j^B \tag{2.1}$$

The structure functions, F^A and F^B, give the probability that a given parton will carry momentum fraction, x, of its parent proton or anti-proton. These are determined experimentally by deep inelastic scattering of leptons off protons. The quantum electrodynamic description of this process, as shown in figure 2.4, treats the inelastic scattering of the virtual photon off the proton as elastic scattering of a free, point-like quark. This leads to the prediction that the structure functions will be independent of the momentum transfer, Q, and are said to "scale". But in the QCD description, the effects of initial and final state gluon radiation are taken into account and the structure functions develop an explicit dependence on Q^2. This dependence introduces additional theoretical uncertainty, since the structure functions are measured at values of Q^2 that are much lower than the Q^2 at which

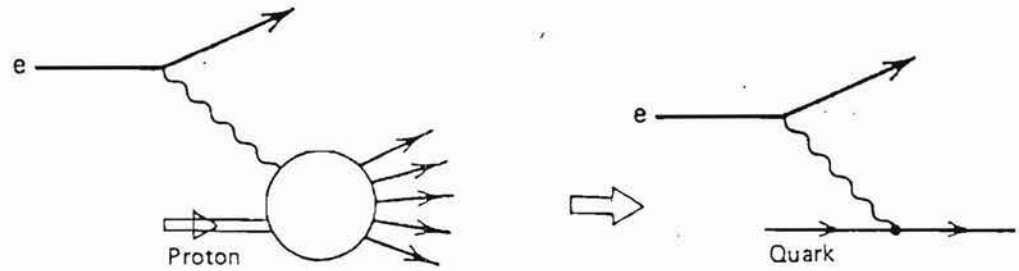

Figure 2.4

Quantum electrodynamic description of lepton-proton deep inelastic scattering.

the cross-section will be calculated.

The most precise structure function measurements have been made at $Q^2 \approx 10GeV^2$. In the past two years structure function measurements have been made at values of x down to about 0.02. The structure function is parameterized as a function of x to allow extrapolation from the measured range to lower values of x [3]. To evolve the structure function to the value of Q^2 at which the cross-section is calculated, one uses the Altarelli-Parisi [6] equations that result from perturbative QCD.

Theoretical uncertainties in the calculation of $\hat{\sigma}$ arise from limited knowledge of the b quark mass; the renormalization scale, μ; and the structure function. The mass of the lightest bound $b\bar{b}$ state, $\Upsilon(1S)$, gives an estimate of 4.75 GeV/c^2 for the mass of the b quark, and this is the value used in the cross-section calculation by Mangano, Nason, and Ridolfi(MNR)[2].

The renormalization scale, μ, is introduced by a prescription to handle divergent

terms that arise in calculating $\hat{\sigma}$ at finite order in α_s. In a calculation to all orders of α_s, the divergent terms cancel out, so the calculation of $\hat{\sigma}$ would be independent of the choice of the renormalization scale. μ is chosen such that the higher order terms that depend on $ln(Q^2/\mu^2)$ are well behaved at the scale involved in the interaction, such as the quark mass and/or transverse momentum of the quark produced. In the MNR cross-section calculation, μ is chosen to be $\sqrt{p_T^2 + m_b^2}$. Figure 2.5 shows the variation in the cross-section that results from dividing μ by a factor of 4. The variation in the total cross-section is large, indicating that still higher powers of α_s are necessary to completely describe b quark production. Nevertheless, the shape is not very strongly dependent on μ, so experimental measurement of the differential cross section can still provide a useful check of the QCD calculation.

Uncertainties in the structure function determination come mainly from the extrapolation to the small x region. A large fraction of b quarks are produced by gluon interactions, but the gluon distribution functions are not as well-determined as the quark distribution functions. This is because in lepton-proton scattering, the photon can directly interact with the quarks, but not with the gluons. Measurements of the gluon distribution at small values of x has depended on charm production in lepton-proton scattering experiments via the process shown in figure 2.6 [7, 8, 9], as well as direct photon production in $p - \overline{p}$ collisions [10].

The dependence of the cross-section calculation on the structure function uncertainty can be illustrated by using the structure function sets $D_0{}'$ and $D_-{}'$ determined by Martin, Roberts, and Stirling (MRS)[11]. The two sets differ only in the assumed form of the gluon distribution at small x. The $D_0{}'$ set uses a gluon distribution function that is finite at x=0, while $D_-{}'$ set uses a function that is singular at x=0. Figure 2.7 shows the cross-section calculations using each structure function set.

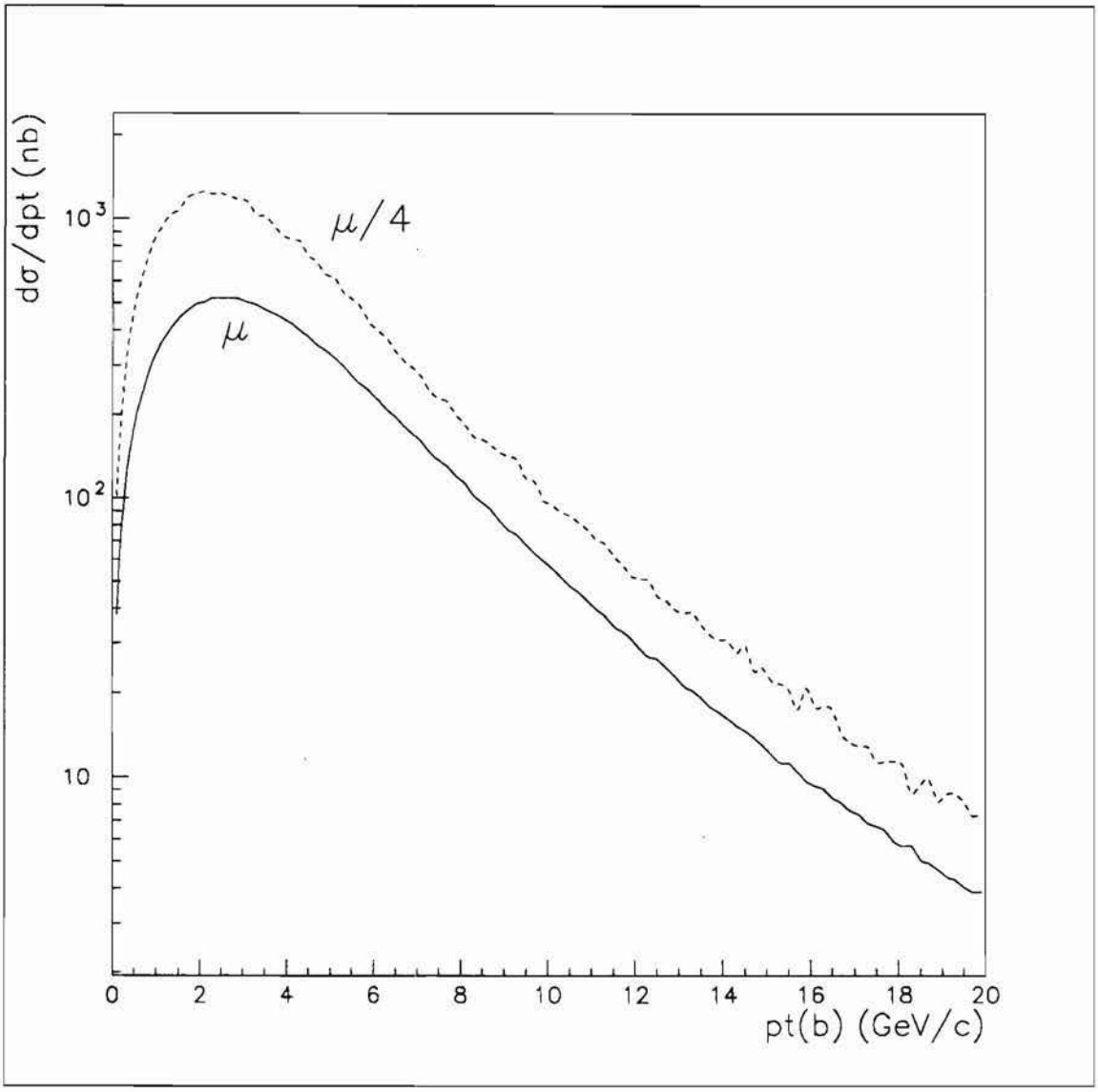

Figure 2.5

Dependence of the theoretical b quark cross-section on the choice of the renormalization scale, μ.

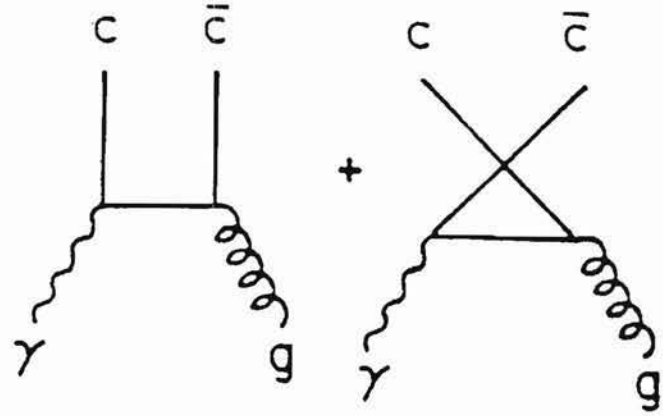

Figure 2.6

J/ψ production diagram used to determine the gluon structure function in lepton-proton scattering experiments.

Recent measurements of quark distribution functions from HERA [12] seem to favor D_-', as shown in figure 2.8, but still are too statistically uncertain to provide conclusive proof. Preliminary results from CDF on the same-side/opposite-side dijet cross-section ratio [13] shown in figure 2.9 also seem to favor the D_-' set, but the measurements are still statistically consistent with D_0' set as well. It is likely that improved direct measurement of the gluon distribution will soon be made at HERA, which will hopefully resolve the question of the small x behavior of the gluons.

In order to confront the theoretical prediction for the b quark cross-section with the B meson cross-section that is directly measured, a prescription for relating the b quark and B meson transverse momenta is needed. The process by which a colored quark becomes part of a colorless, observable hadron is called fragmentation. As the initial quark-antiquark pair travel away from each other, the increasing force

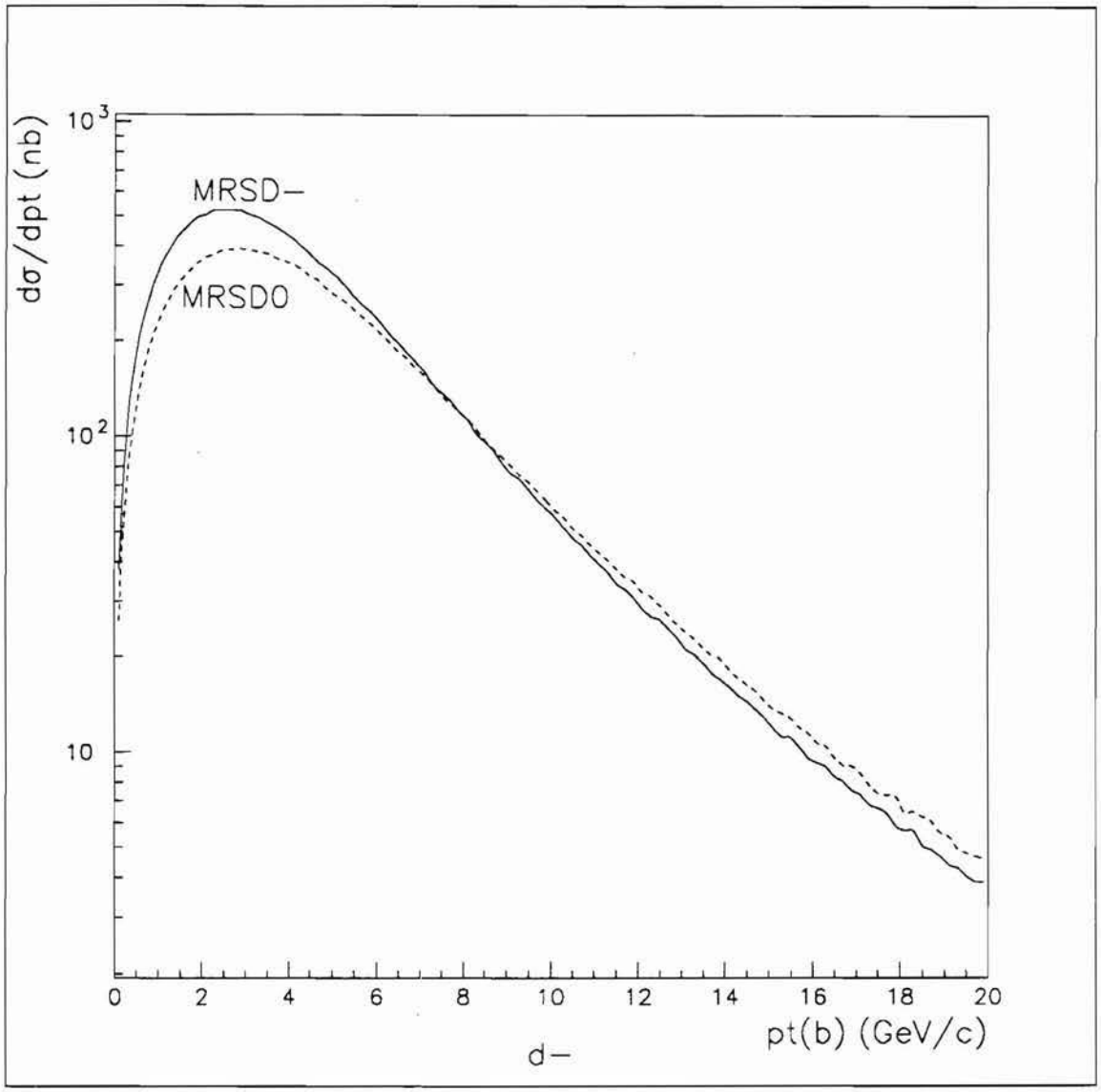

Figure 2.7

Dependence of the theoretical cross-section on choice of proton structure function set.

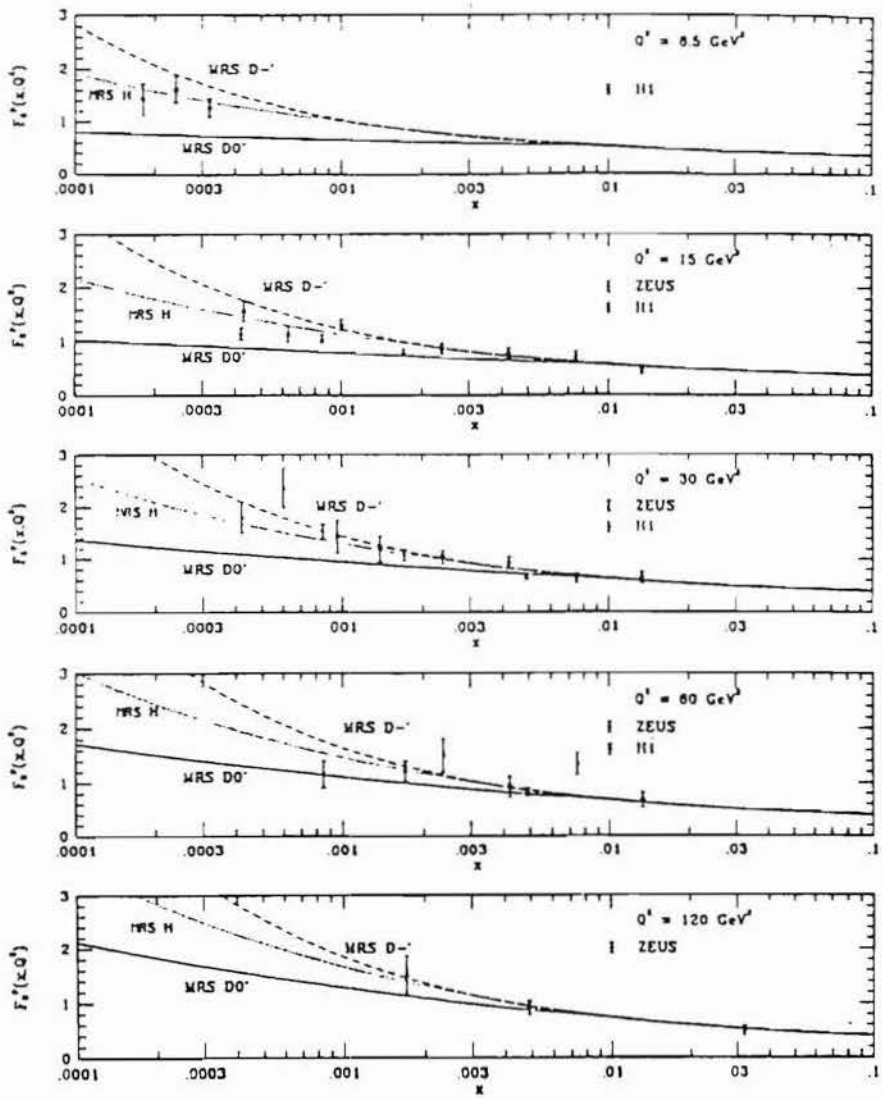

Figure 2.8

Structure function measurements from the H1 and ZEUS detectors at the HERA *ep* collider, compared to the MRS D_0' and D_-' predictions.

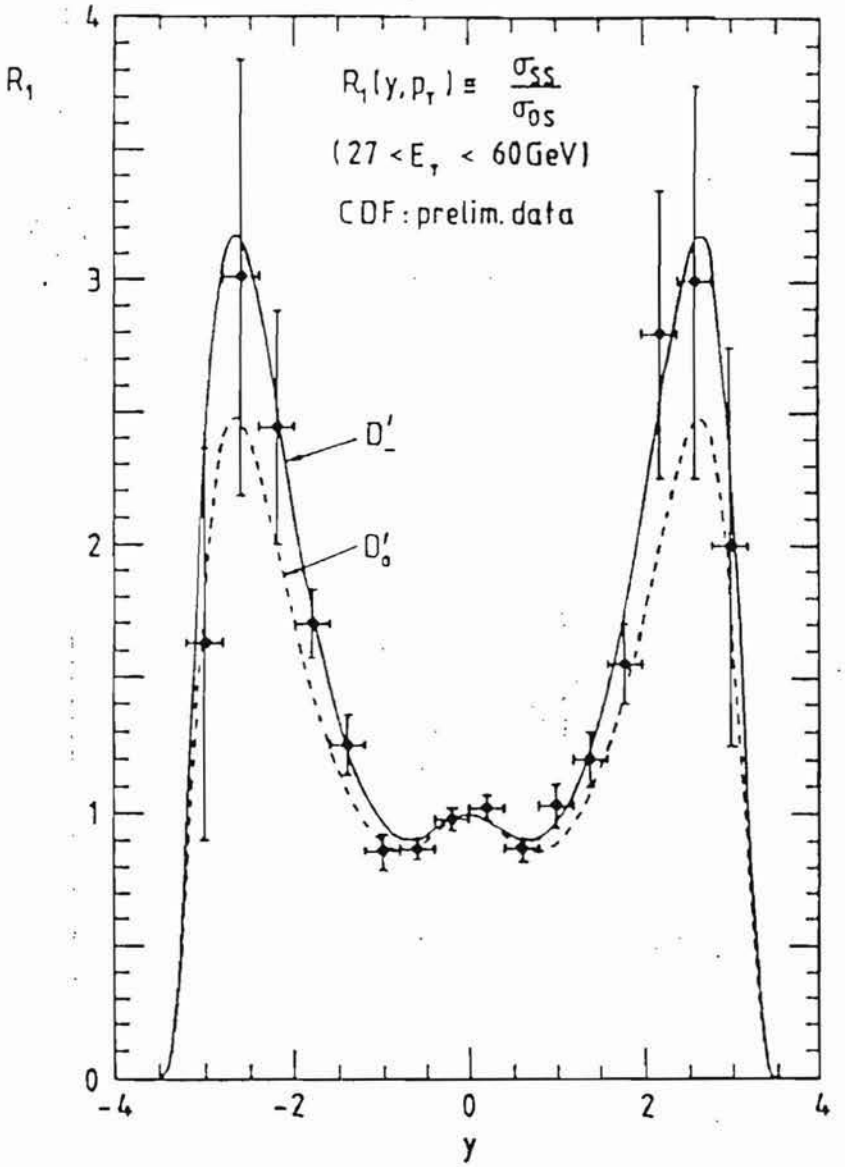

Figure 2.9

Preliminary CDF measurement of the same-side/opposite-side dijet ratio, compared to the MRS D_0' and D_-' predictions.

of the strong interaction causes the emission of gluons which, in turn, emit more gluons as well as quark-antiquark pairs. In the case of a b quark fragmenting into a B^- or $\overline{B^0}$ meson, the quark combines with one of the $\overline{u}$ or $\overline{d}$ quarks formed.

The fragmentation process can be characterized by z, the fraction of the initial b quark transverse momentum that is carried by the B meson. The probability distribution of the B meson p_T is described by a fragmentation function D(z). D(z) is not calculable by perturbative QCD, so a semi-empirical parameterization is used. Because the b quark is so massive, the B meson it forms carries most of its initial p_T, thus D(z) is expected to peak near the maximum value z=1. The parameterization by Peterson, et al. [14] incorporates this expectation:

$$D(z) = \frac{N}{z(1 - 1/z - \epsilon/(1-z))^2}$$

where N is set by the normalization requirement $\int_0^1 D(z)dz = 1$. The term $1 - 1/z - \epsilon/(1-z)$ is the energy lost by the b quark through gluon emission. ϵ depends on the energy of the gluon products and is determined experimentally. In reference [15], ϵ was determined to be 0.006±0.002 by combining the results of several measurements of inclusive lepton production at e^+e^- colliders. Figure 2.10 shows D(z) for this value of ϵ. The most probable value of z is 0.93.

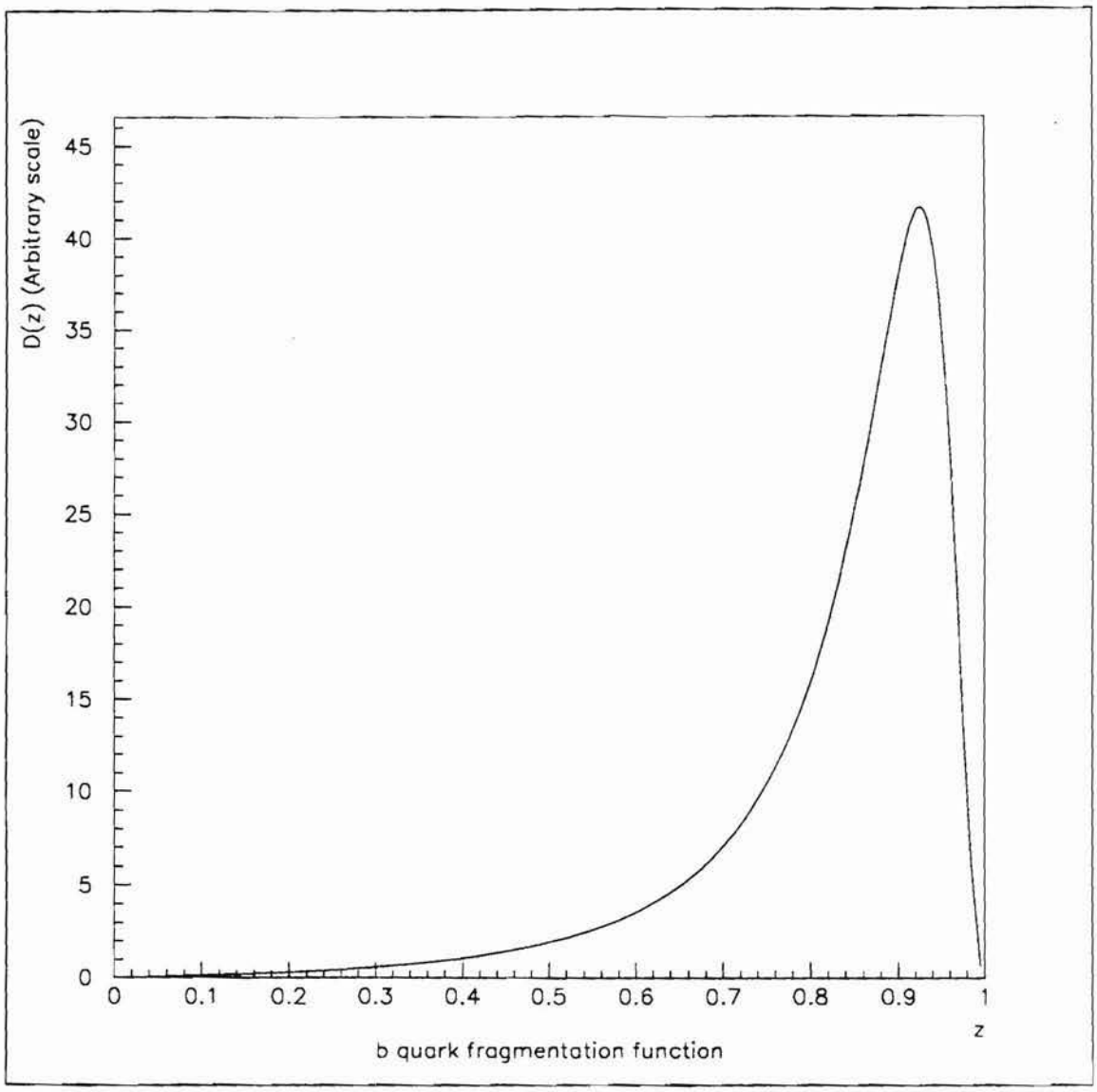

Figure 2.10

Peterson parameterization of the b quark fragmentation function, D(z), for $\epsilon = 0.006$.

3. THE COLLIDER DETECTOR AT FERMILAB

The Collider Detector at Fermilab (CDF) was the first general purpose detector built to study the 1.8 TeV $p - \overline{p}$ collisions at the Fermilab Tevatron accelerator. Its central detector region contains a large high-resolution cylindrical tracking chamber which operates in a uniform 1.4 T magnetic field produced by a superconducting solenoid. Surrounding the tracking chamber are finely-segmented electromagnetic and hadron calorimeters. Beyond the hadron calorimeters are the drift cell modules that comprise the central muon detector.

The magnetic field is oriented along the direction of the proton beam. Since charged particles traversing such a field follow helical trajectories, a cylindrical coordinate system provides the most natural description of the CDF geometry. The z-axis is in the direction of the proton beam, and the zero value of z is defined at the center of the detector. In addition to the standard definitions for the radial direction, r, and azimuthal angle, ϕ, a fourth variable, η, called pseudorapidity, is defined in terms of the polar angle, θ, as $\eta = -\ln \tan \theta/2$.

The tracking chamber covers the pseudorapidity range $|\eta| < 1$, while the central calorimeters cover a slightly larger range, and the muon detector covers the range $|\eta| < 0.6$. Inside the tracking chamber is a vertex time projection chamber which surrounds a four-layer silicon vertex detector. Both of these detectors exceed the pseudorapidity coverage of the CTC. However, due to the variation of the actual interaction point in z (which is distributed according to a Gaussian probability function with mean value z=0, and $\sigma_z = 30cm$), the 58 cm-long silicon vertex

detector provides information for only about half the particles produced.

Figure 3.1 shows a cross-section of the entire detector.

The full reconstruction of the decays of B mesons, on which the analysis that will be described is based, requires high resolution track reconstruction, so each component of the tracking and vertexing system in the central region will be described in more detail in this chapter. The muon detector is used to trigger on the decays of interest and will also be described.

CDF also has calorimeters on each end of the tracking chamber which cover the pseudorapidity range out to $|\eta| = 2.4$, and forward detectors which contain calorimeters that extend coverage out to $|\eta| = 4.2$. Descriptions of these can be found elsewhere [16]. There is also muon detection in the forward region, but since there is no overlap with the tracking chamber, it is not used in this analysis (see ref. [17]).

3.1 Central Tracking Chamber

The central tracking chamber (CTC) is a drift chamber covering the pseudorapidity range $-1 < \eta < 1$. Its active region has an inner radius of 28 cm and an outer radius of 138 cm. Parallel sense wires spaced 10 cm apart are located in drift cells which are tilted at an angle of 45° with respect to the radial direction. In figure 3.2 is shown an endplate of the CTC, indicating the arrangement of the drift cells. For the electric drift field value of $1350 V/cm$ and magnetic field of 1.4 T in the argon/ethane/alcohol gas mixture that fills the chamber, this tilt causes the electrons produced by charged particles to drift in a direction perpendicular to the radial direction, as illustrated in figure 3.3. The tilt also allows cells to be overlapped by about 20% and helps to resolve ambiguities in the pattern recognition.

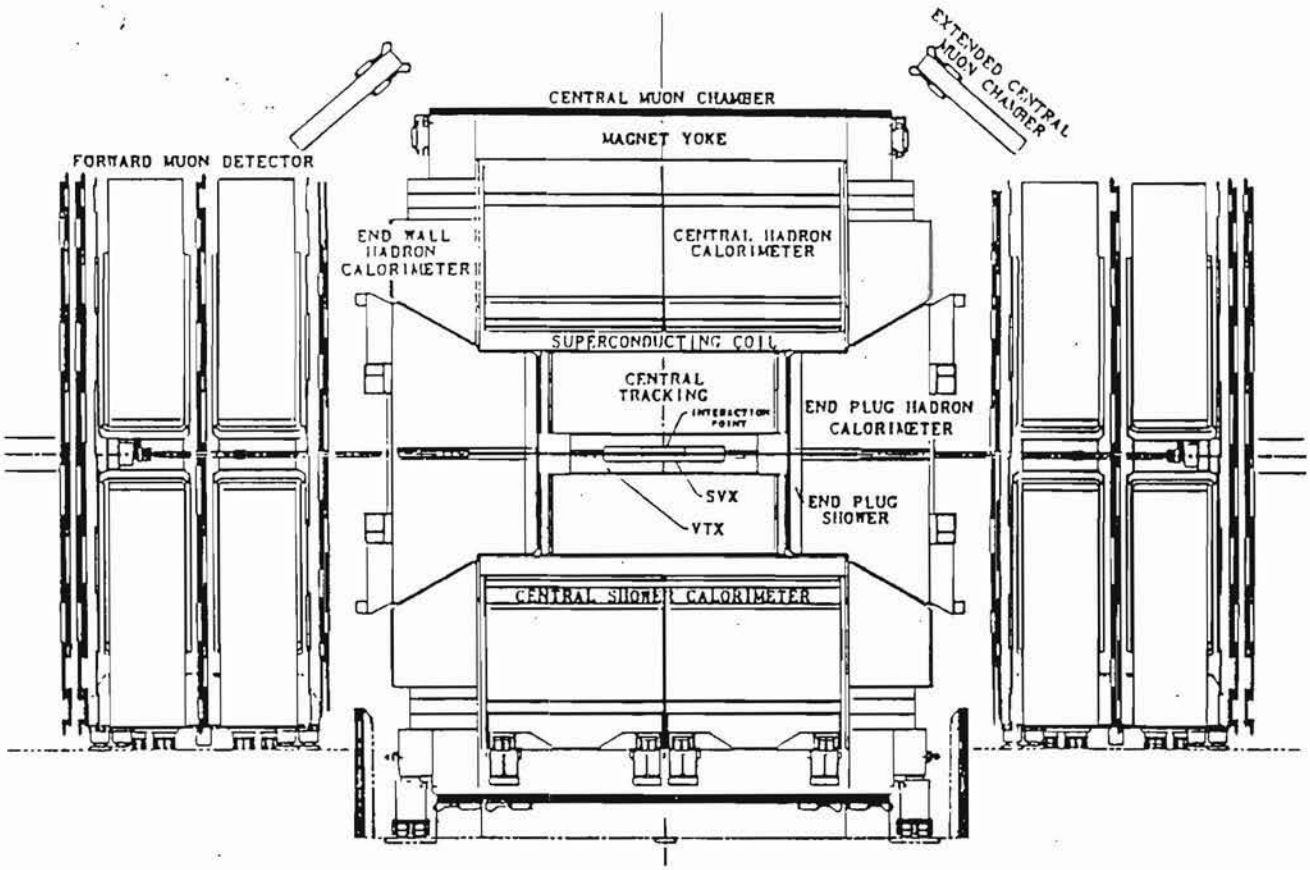

Figure 3.1

Cross-section view of the CDF detector layout for the 1992-93 collider run.

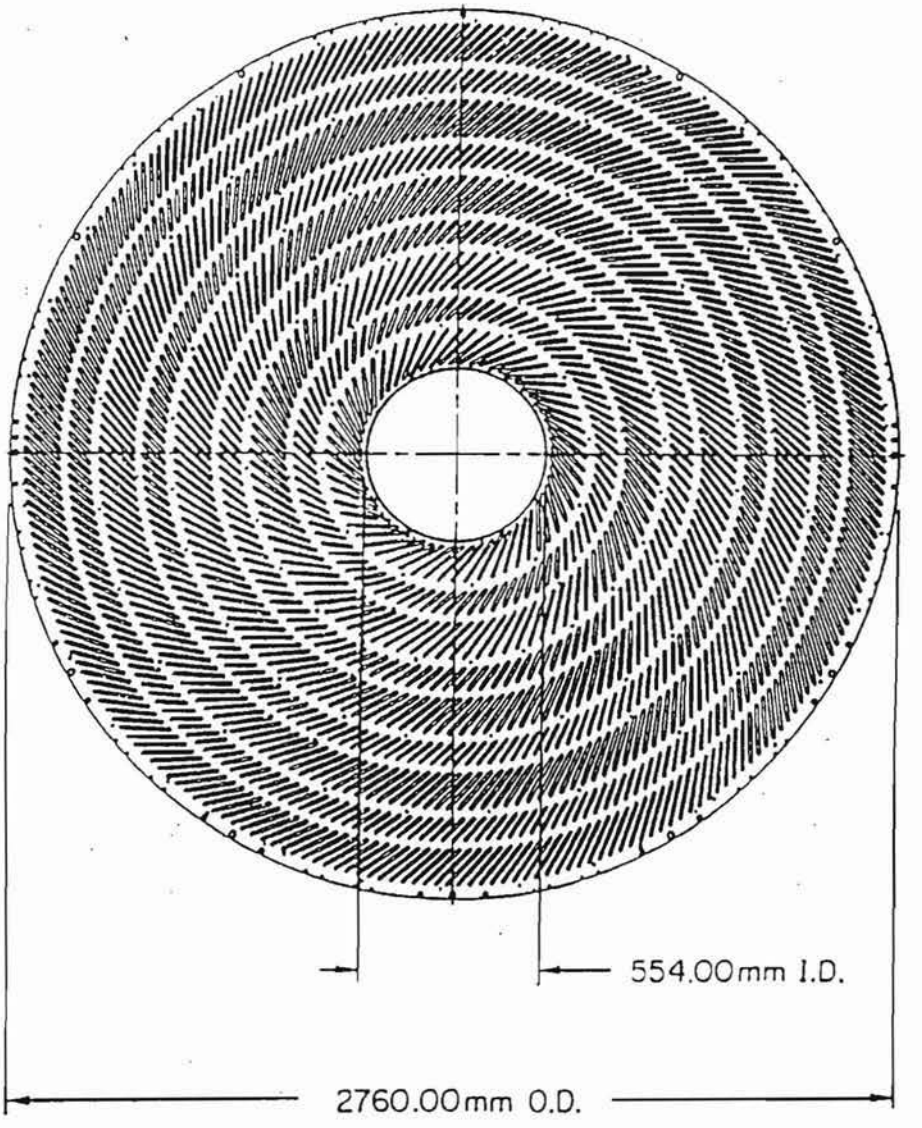

Figure 3.2

A CTC endplate, showing the location of the axial and stereo drift cells.

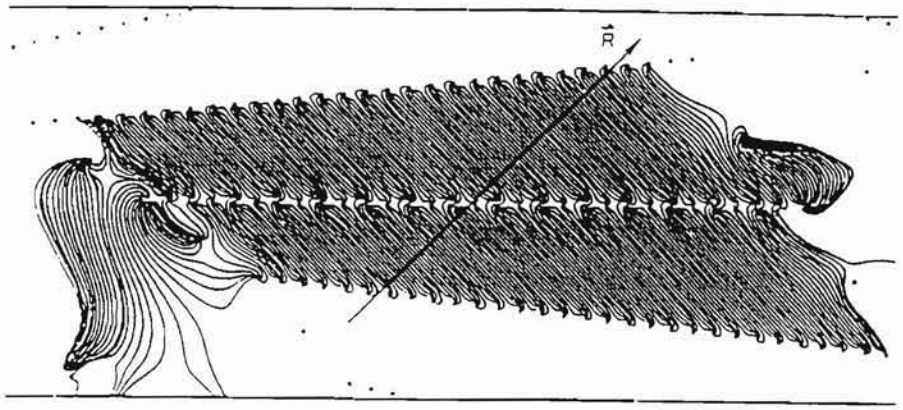

Figure 3.3

Particle drift trajectories in the CTC, with respect to the radial direction indicated by the arrow.

Some drift cells contain 12 sense wires that are parallel to the z-axis; others contain 6 sense wires at a 3° angle with respect to the z-axis. The drift cells are grouped into 9 superlayers, numbered 0-8. Axial superlayers 0, 2, 4, 6, and 8 contain the 12-wire drift cells providing $r - \phi$ information. Stereo superlayers 1, 3, 5, and 7, which contain the 6-wire cells, give $r - \phi$ information and, due to the 3° angle of the sense wires, give z information as well.

The part of a charged particle trajectory that is reconstructed in the CTC is a circular arc in the $r - \phi$ plane. The curvature of the arc varies inversely with the transverse momentum of the particle. As the momentum increases, the curvature of the track becomes more uncertain as the arc becomes close to a straight line. This results in a momentum resolution that is dependent on the tranverse momentum of the particle. The $r - \phi$ resolution of the chamber is better than $200\mu m$ at each wire layer. Constraining tracks from the same particle decay to come from a common

vertex results in a momentum resolution of $\delta p_T/p_T < [(0.0014p_T)^2 + (0.0066)^2]^{1/2}$.

3.2 Central Fast Track Processor

The 45° tilt of the CTC drift cells and 20% overlap of adjacent cells ensures that the approximately radial tracks of particles with high transverse momentum will cross at least one plane of sense wires in each superlayer. This enabled the implementation of a fast track processor (CFT), using the hit information from the 5 axial superlayers.

The CFT track identification process begins by recording the locations of all wires in the outermost superlayer that register a hit within 80 ns after beam crossing, called prompt hits. Hit information from the other superlayers is processed sequentially in ϕ. For each prompt hit identified in the outermost superlayer there is an associated list of possible hit patterns, or "roads", stored in the CFT memory. The prompt hits found in the other four axial superlayers are compared to each such road, and the road which contains the most hit matches is identified. If two or more roads have the same number of hit matches, the road corresponding to the highest momentum is chosen. Additional "delayed hit" information is recorded for wires which register a hit between 500 and 650 ns after beam crossing. These hits are matched to roads to verify high p_T tracks found using the prompt hits. Figure 3.4 shows the hit pattern and road for a representative 5-GeV/c track.

The CFT track identification is combined with information from other detectors, such as the central muon chambers, allowing tighter quality cuts to be used to improve particle identification.

The momentum ranges of tracks identified by the CFT can be varied by changing the set of roads defined in the memory look-up tables, with a minimum allowable p_T of 2.5 GeV/c. A total of 32 roads for each wire in the outermost

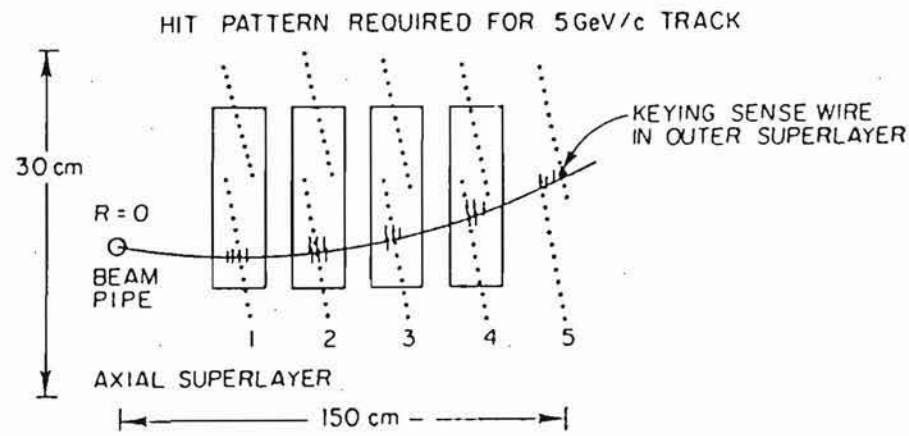

Figure 3.4

A set of roads recognized by the CFT for a 5-GeV/c track, defined by a hit in the outermost superlayer.

superlayer can be defined. These roads are divided into 8 p_T bins, each of which are subdivided into two azimuthal angle ranges for each particle charge.

3.3 Silicon Vertex Detector

The Silicon Vertex Detector(SVX) was a new addition to CDF for run 1a. The detector is divided into two identical modules, called barrels, that surround the beam with one end of each barrel located at z=0. Each SVX Barrel consists of four layers of silicon microstrip detectors arranged concentrically about the beam, with the innermost layer 2.9 cm from the center of the beam. Each layer consists of twelve ladders which lie parallel to the beam. A cut-away view of the detector is shown in figure 3.5. A ladder is composed of three detectors which are bonded together to form a single unit with an active length of 25.5 cm, as shown in figure 3.6.

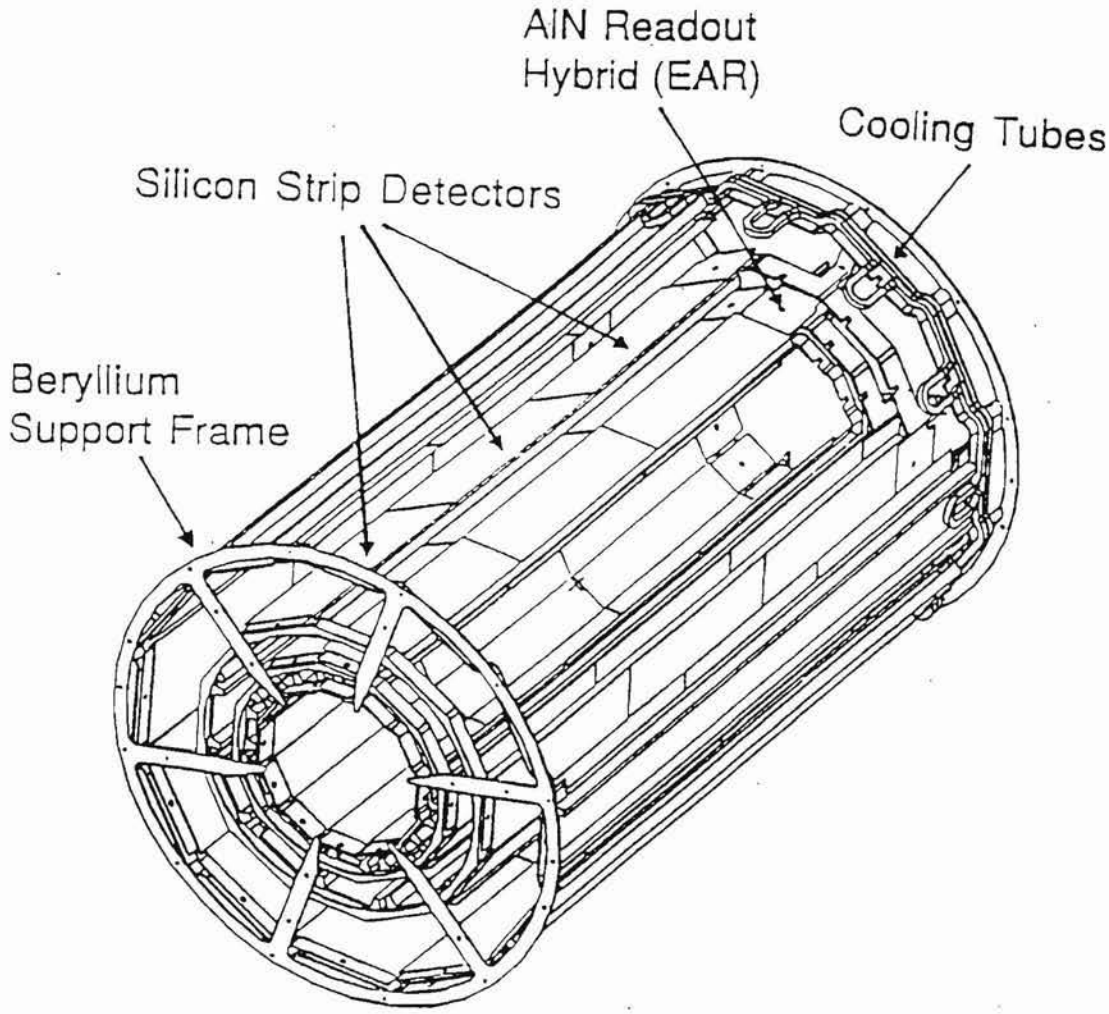

Figure 3.5

A cut-away view of the SVX detector, showing ladder arrangement and the support frame.

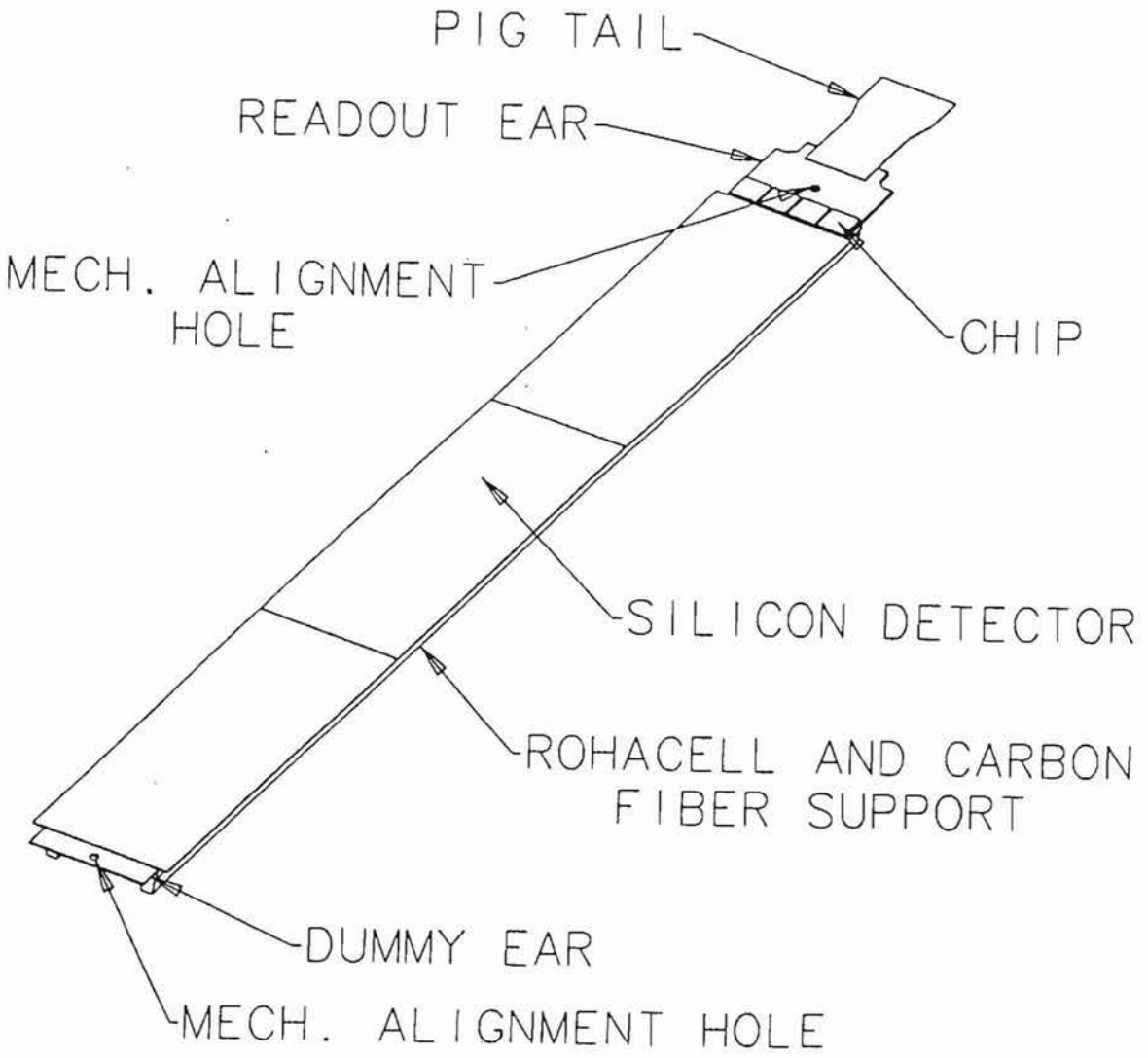

Figure 3.6

An SVX ladder, composed of 3 silicon microstrip detectors, readout electronics, and support structure.

The detectors are composed of p-type silicon strips deposited in an n-type silicon substrate. A bias voltage is applied across the p-n junction to fully deplete the material of free charge carriers. When charged particles pass through the detector, pairs of electrons and holes are created which cause a current pulse. The energy required to produce an electron-hole pair is 3.6 eV, so for a minimum ionizing particle depositing a most probable energy of 110 KeV, about 30,000 pairs are produced. Each of the electrons drifts to its nearest strip, which often induces current in more than one strip. The actual magnitude of the liberated charge for each strip can be read out, enabling a "center-of-gravity" calculation of the most probable hit location to finer accuracy than the 60 μm pitch of the strips. This data is read out through an "ear" located at one end of each ladder, which contains the readout electronics and also serves to attach the ladder to a beryllium bulkhead support structure. On the opposite end is a dummy ear(containing no electronics), which attaches the ladder to another bulkhead positioned at approximately z=0. The barrels are positioned so that the readout bulkheads are located at z=29.5 cm and z=-29.5 cm.

All three detectors in a ladder are bonded together, so there is no z information provided by this detector. However, very fine segmentation in ϕ provides a resolution of 8 μm at each layer[18].

Pattern recognition in the SVX first requires the part of the track contained in the CTC to be reconstructed. The track is then extended to the best fitting point in the outermost SVX layer(layer 3), and the track covariance matrix is updated to define roads in which to search for a hit in layer 2. If a hit is found, the procedure continues for layers 1 and 0. The impact parameter resolution thus achieved is better than 25 μm for charged particles with $p_T > 2GeV/c$ [19].

3.4 VTX Detector

The vertex time projection chamber(VTPC) was operated successfully in the 88-89 run, and was upgraded for run 1a. This upgraded version (VTX) consists of 28 separate modules covering between $\pm$ 1.4m in z, and out to 21 cm in r. The modules are octagonal, and each octant is aligned with an octant of the CTC. High voltage grids in the center of the modules divide each octant into two drift regions 4 cm long in z. Sense wires equally spaced in r are arranged perpendicular to the beam line, and are read out at the ϕ boundary between octants. The detector cross-section is shown in figure 3.7. For the five modules at either end of the VTX, there are 24 of these sense wires, with the innermost one positioned at $r = 6.8cm$. The innermost 18 modules surround the SVX and have 16 of the sense wires. Cathode pads are located at the z boundary between modules.

The principle utility of the VTX is to provide z information of the primary interaction point, and to determine the angle of a track in the θ direction, which complements the $r - \phi$ information provided by the CTC and the SVX detector. The z vertex measurement is also used to enhance the CTC pattern recognition in cases where the hit information in the CTC stereo superlayers is insufficient. The resolution in the r-z plane is 200 μm at $\eta = 0$, and the z-vertex resolution is 2 mm.

3.5 Central Muon Detector

The CDF cental muon detector consists of 24 wedges in each of two identical halves, one covering the region z= 0 to 2.26m and the other covering z=0 to -2.26m. Each wedge is mounted on the top of a hadronic calorimeter wedge, at a radial distance of 3.47 m from the beam line. The location is diagrammed in figure 3.8. Particles detected in the chamber must have traversed an amount of material representing about 5 absorption lengths for pions at normal incidence. A wedge

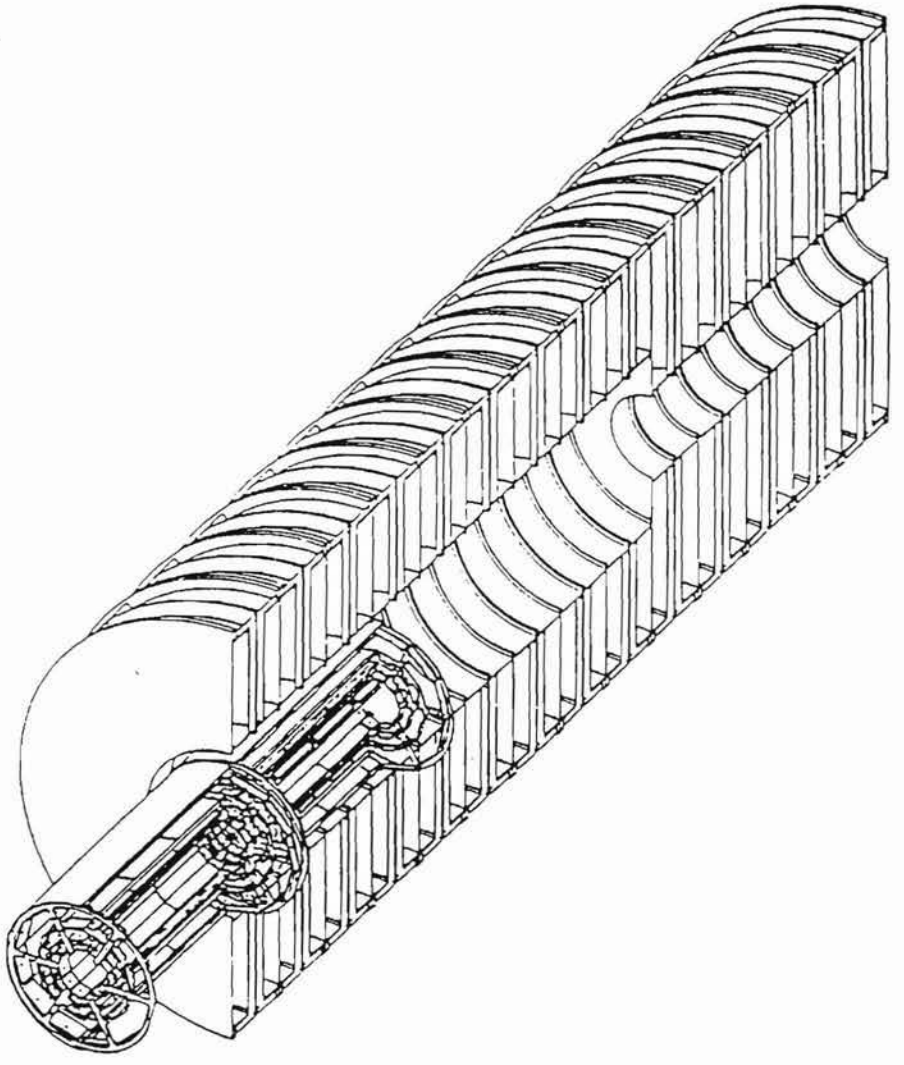

Figure 3.7

Cross-section of the VTX detector, which exposes the 4-cm wide drift regions, and the larger inner radius near $z = 0$ which accomodates the SVX detector.

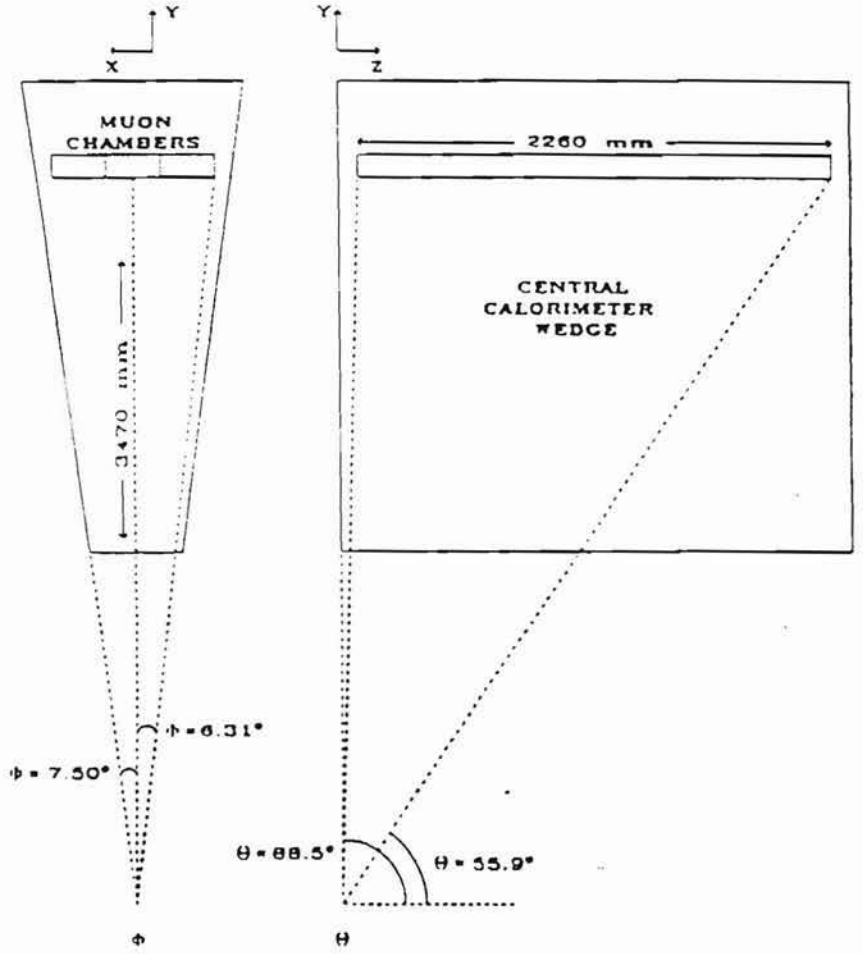

Figure 3.8

Location of the central muon chambers within a central calorimeter wedge.

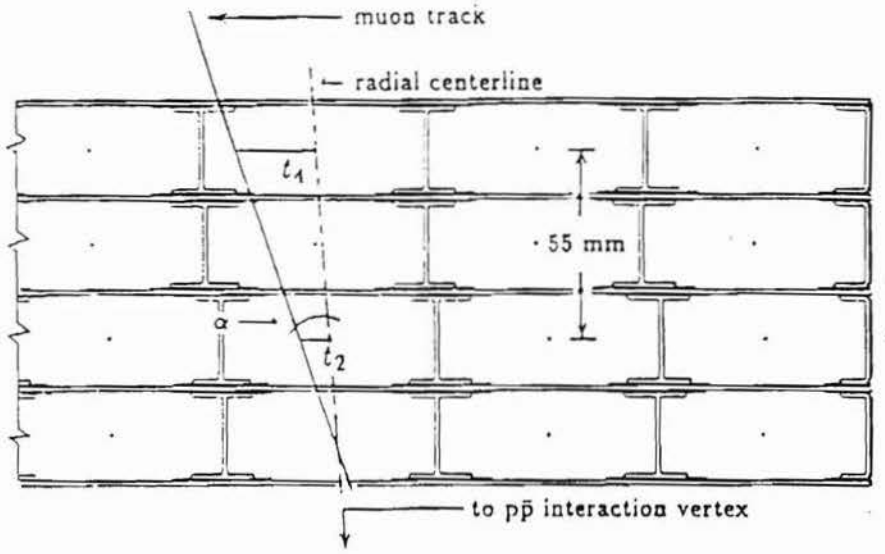

Figure 3.9

Cross-section of a central muon chamber, as viewed along the beamline direction.

consists of three modules, each of which covers 4.2° in ϕ. This leaves a 2.4° gap in ϕ between each wedge. The modules consist of four radial layers of four drift cells each. Near the center of each is located a sense wire which extends parallel to the beam line. The $r - \phi$ location of the sense wire is offset by 2 mm for alternate layers. The alternate pair of sense wires which is hit first determines on which side of the wires a particle has passed. The cross-section of a module, as viewed along the beam line, is shown in figure 3.9.

TDCs record the drift time of charged particles to each sense wire. A track in at least three layers determines the angle in the $r - \phi$ plane of the particle trajectory. Figure 3.10 shows an idealized muon trajectory in the transverse plane. The angle α between the radial direction and the muon chamber track segment is related to the muon transverse momentum as follows:

$$\alpha \approx sin(\alpha) = \frac{eL^2B}{2Dp_T}$$

where e is the muon charge, B is the magnetic field, L is the radius of the solenoidal coil, and D is the radius of the innermost sense wire plane of the muon chambers. The relationship between the TDC values and the particle p_T allows implementation of a level 1 trigger, which will be discussed in the next chapter. ADCs record the pulse height at each end of the sense wire, allowing the position of the particle track in z to be determined by charge division. The resolution achieved is 250 μm in $r - \phi$ and 1.2 mm in z.

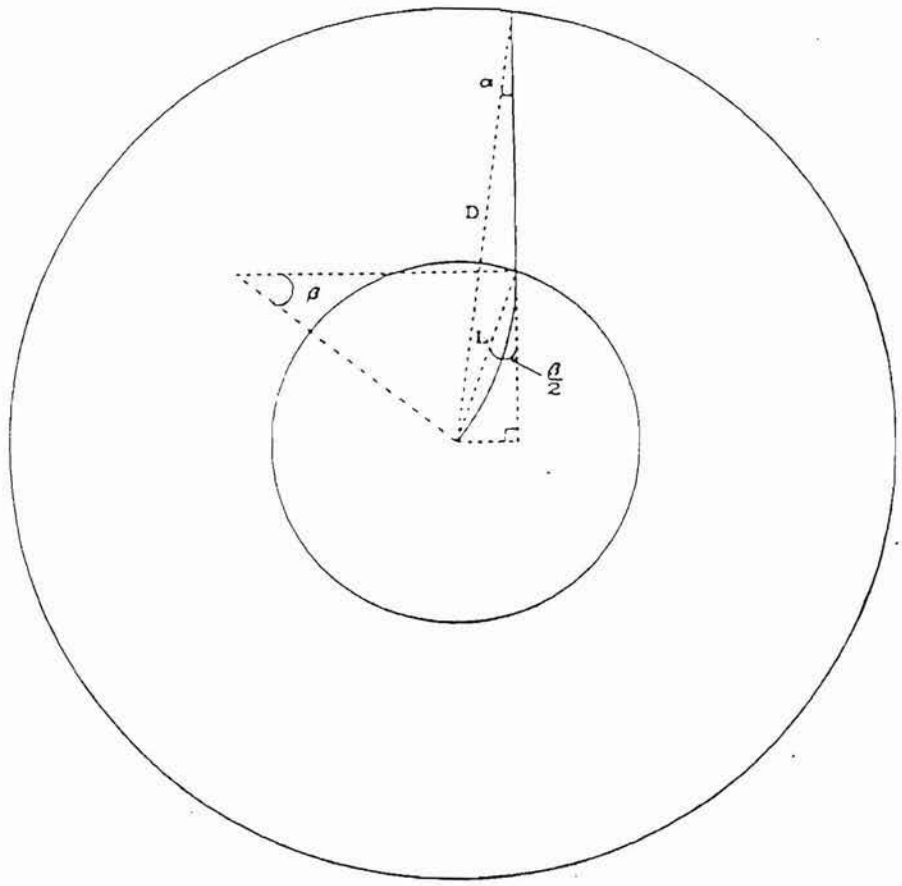

Figure 3.10

Charged particle trajectory in the transverse plane. The inner circle of radius L represents the CTC within the magnetic field region.

4. DATA SAMPLE SELECTION

In this chapter, the method of selecting B meson candidates will be described. For the decay channels used in this analysis, there is required to be a J/ψ decaying to two muons in the final state. Hardware triggers and quality cuts on the muons are used to obtain a sample of J/ψ candidates. After this sample is obtained, precise track reconstruction is performed and the muon tracks are refitted to a common vertex, and required to have an invariant mass consistent, within errors, with $m_{J/\psi}$, the average J/ψ mass measured in CDF.

The muons and the other B decay product candidates are required to pass transverse momentum cuts. The decay product tracks are then refitted to a common vertex, while constraining the invariant mass of the muon pair to equal the J/ψ mass. A cut is made on the confidence level of the of the vertex fit χ^2 and on the B decay length. Finally, the invariant mass of the B candidate is formed, and the mass distribution is fitted to determine the number of B mesons over background.

4.1 Di-muon J/ψ Trigger

For the 1992-93 run, there were three levels of trigger requirements that must have been passed for any event to be recorded. For this analysis, only the subset of events that have passed one of the triggers dedicated to tagging J/ψ are used. The Level 1 trigger requires two separate muon chamber track segments in the central muon chambers, each of which must have a muon chamber angle, α (see

figure 3.10), smaller than a value which corresponds to a nominal muon p_T of 2 GeV/c. Multiple Coulomb scattering and energy lost by the muons as they pass through the calorimeters degrades the relationship between α and the p_T of the muon, so some muons with p_T below 2 GeV/c fire the trigger, and some with p_T above 2 GeV/c fail.

The Level 2 trigger requires that at least one of the muons identified at Level 1 is matched to a track identified by the CFT.

At Level 3 of the trigger system a majority of the software event reconstruction is performed, including CTC tracking, and linking track segments in the muon chambers with CTC tracks. In linking the segments, a χ^2 of the fit in both the $r-\phi$ and z directions is calculated. Both $\chi^2(r-\phi)$ and $\chi^2(z)$ of a muon candidate are required to be less than 16. If two such muon candidates of opposite sign are identified, the invariant mass is formed. If the mass lies within a 600 MeV/c^2 window about the J/ψ mass, the event is written out for further analysis offline.

The event reconstruction at Level 3 is only a subset of the full reconstruction that is done offline. This is due to a compromise between the desire to minimize detector deadtime due to a full DAQ pipeline, and the need to make selections based on track momenta and invariant masses of multi-particle systems. The time constraint requires that, for example, the addition of SVX information to CTC tracks is not done at Level 3.

The offline event reconstruction repeats the Level 3 reconstruction, and uses an enhanced CTC track reconstruction algorithm. As a consequence, it is sometimes the case that a different CTC track is linked to a muon chamber track segment than was done online. For these cases, the same requirements that were made at Level 3 are imposed. The possibility of false tracks in the CTC, which consists of five axial superlayers with 12 wire layers each and four axial superlayers with 6 wire

layers each must be considered. In order to remove such false tracks formed from accidental combinations of noise hits and to ensure that the track is adequately reconstructed in 3 dimensions, each track is required to contain at least 4 hits in each of at least 2 axial superlayers, and at least 2 hits in each of at least 2 stereo superlayers. For all tracks passing these requirements, SVX track reconstruction is attempted.

4.2 SVX Tracking Algorithm

SVX track reconstruction begins with a track that has been reconstructed in the CTC. The CTC track is extrapolated to the outermost layer of the SVX, layer 3. SVX clusters are searched for in a road of width four times the error (including multiple scattering) on the intersection of the extrapolated track with layer 3 of the SVX. For any clusters found in this road, the CTC track covariance matrix is updated, and the track is further extrapolated into the next layer of the SVX, layer 2. It may happen that more than one cluster is found in the road on the layer 3; if so, each such cluster can be used to define a separate road in which to search for clusters on layer 2. Similarly, any cluster found in the road(s) on layer 2 is used to update the track parameters and define a search road on layer 1, and so on.

If this method results in more than one set of clusters being associated with a given extrapolated CTC track, the set which forms the SVX track candidate with the lowest fit χ^2 is selected. For this candidate, a quantity called $\delta\chi^2_{03}$ is determined. $\delta\chi^2_{03}$ is the difference in the χ^2 of the track fit using the CTC plus all four layers of the SVX, and the χ^2 using the CTC and only the outermost layer of the SVX. It was shown in reference [20] that $\delta\chi^2_{03}$ is distributed as a χ^2 with 3 degrees of freedom for real tracks. Assuming 3 degrees of freedom, the probability

distribution for $\delta\chi^2_{03}$ is found to be flat in the data sample, except for a spike near 0. The spike is presumably due to tracks which have a coincidental assignment of a noise cluster to the track. Such tracks are removed by requiring that the value of $\delta\chi^2_{03}$ have a probability greater than 0.01%.

If no 4-hit track candidates are found which pass the probability cut, a second search is made for all 3-hit combinations. Again, the track candidate with the lowest χ^2 is selected, and required to pass a similar $\delta\chi^2$ cut. If no such 3-hit tracks are found, a final search is made for 2-hit tracks passing the $\delta\chi^2$ cut. If there are no 2-hit tracks found, then no SVX information is added to the CTC track.

4.3 Offline J/ψ Selection

After the full event reconstruction has been performed offline, more strict requirements are imposed on J/ψ candidates. The χ^2 cut on the match between the CTC track and the muon chamber track segment is tightened by the requirements $\chi^2(r-\phi) < 9$ and $\chi^2(z) < 12$. Also, both of the muons are required to have $p_T \geq 1.8$ GeV/c, and at least one muon must have $p_T \geq 2.8$ GeV/c. As shown figure 4.1, these cuts are chosen at the peaks of the muon transverse momentum distributions, which represent the points at which the Level 1 and Level 2 trigger efficiencies overtake the falling muon p_T distributions.

The muon tracks are then refitted to a common vertex, and the invariant mass is required to satisfy the following condition:

$$\left|\frac{m_{\mu\mu} - m_{J/\psi}}{\delta m}\right| \leq 4.1,$$

where $m_{\mu\mu}$ is the invariant mass of the muon pair, $m_{J/\psi}$ is the CDF average J/ψ mass, and δm is the estimated mass error from the vertex fit. The choice of the value 4.1 will be discussed in the next chapter, but basically represents a 3σ cut on the fitted distribution.

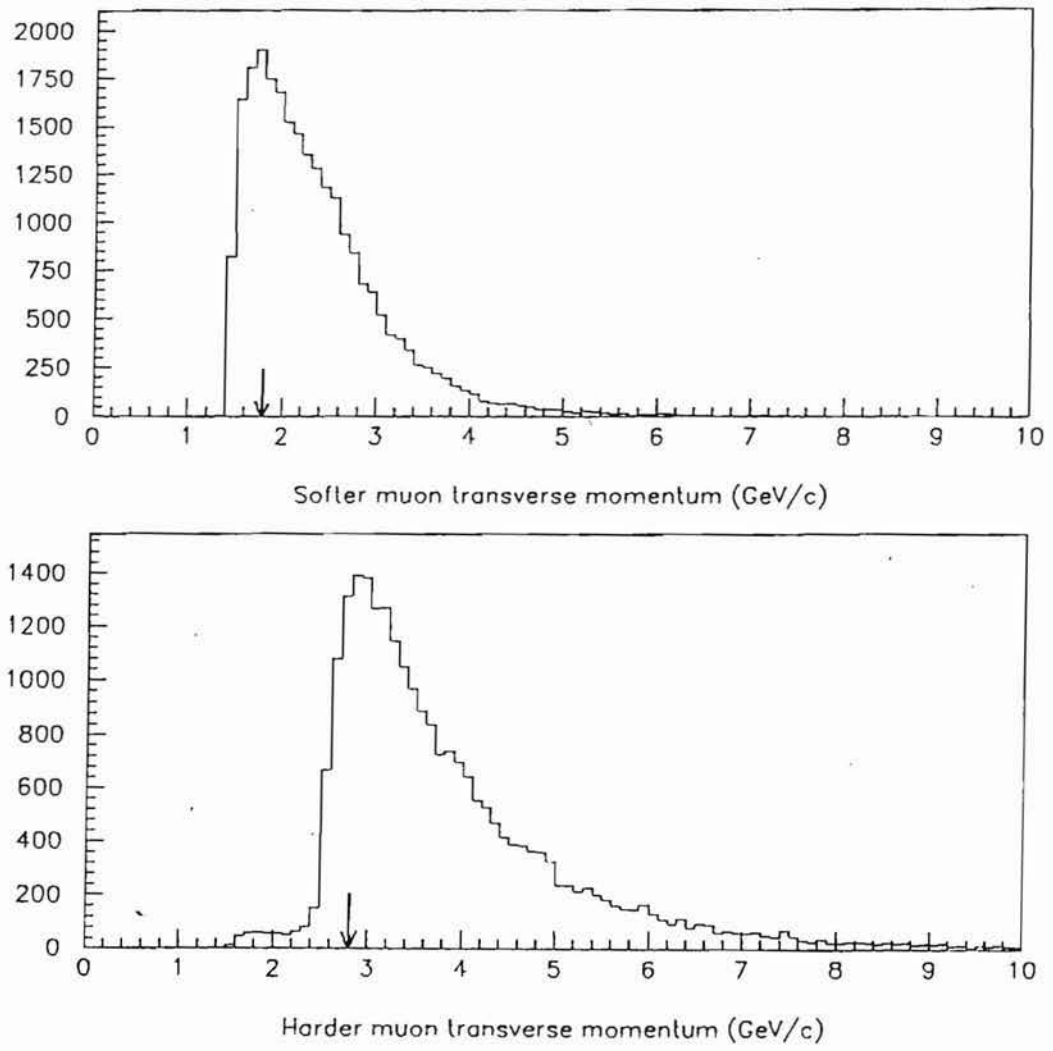

Figure 4.1

Muon transverse momentum distributions. The top plot is for the lower p_T muon from each muon pair, while the bottom plot is for the higher p_T muon.

Figure 4.2 shows the mass distribution of J/ψ candidates after all the selection requirements have been imposed. The J/ψ width varies as a function of p_T, so the mass distribution is non-Gaussian. Therefore, the mass distribution is fitted with a sum of two Gaussians, plus a flat background. The fitted number of J/ψ is 61690 $\pm$ 580 over background, with a mass of $m_{J/\psi} = 3.0932 \pm 0.0001$ GeV/c^2. The fitted widths of the two Gaussians are 16.4 $\pm$ 0.4 MeV/c^2 and 34.2 $\pm$ 0.8 MeV/c^2.

4.4 B Meson Selection Requirements

After the sample of J/ψ candidates has been obtained, the process of finding the remaining decay products to reconstruct the B candidate begins. CDF has limited particle identification which uses measurements of the energy deposited by a particle as it passes through the CTC superlayers. But this method can only resolve kaons from pions below a transverse momentum of about 800 MeV/c. Decay products from B meson decay tend to have a higher transverse momentum than other unassociated tracks in an event, such as those from the underlying event, so imposing p_T cuts is a more efficient means of enhancing the signal to background ratio. Therefore, any charged track in an event, except for the two J/ψ muons, is considered to be a kaon candidate from B decay.

So, to reconstruct the $B^{\pm} \rightarrow J/\psi K^{\pm}$ decay, the muons forming a J/ψ candidate and any third track are refitted to a common vertex, while simultaneously constraining the dimuon invariant mass to the average J/ψ mass. For reconstructing the $B^0 \rightarrow J/\psi K^{*0}$ decay, K^{*0} candidates are identified by taking pairs of oppositely charged tracks in an event(excluding the muons) and refitting them to a common vertex. The invariant mass is formed by arbitrarily assigning the kaon mass to one track and the pion mass to the other. It is required to be between

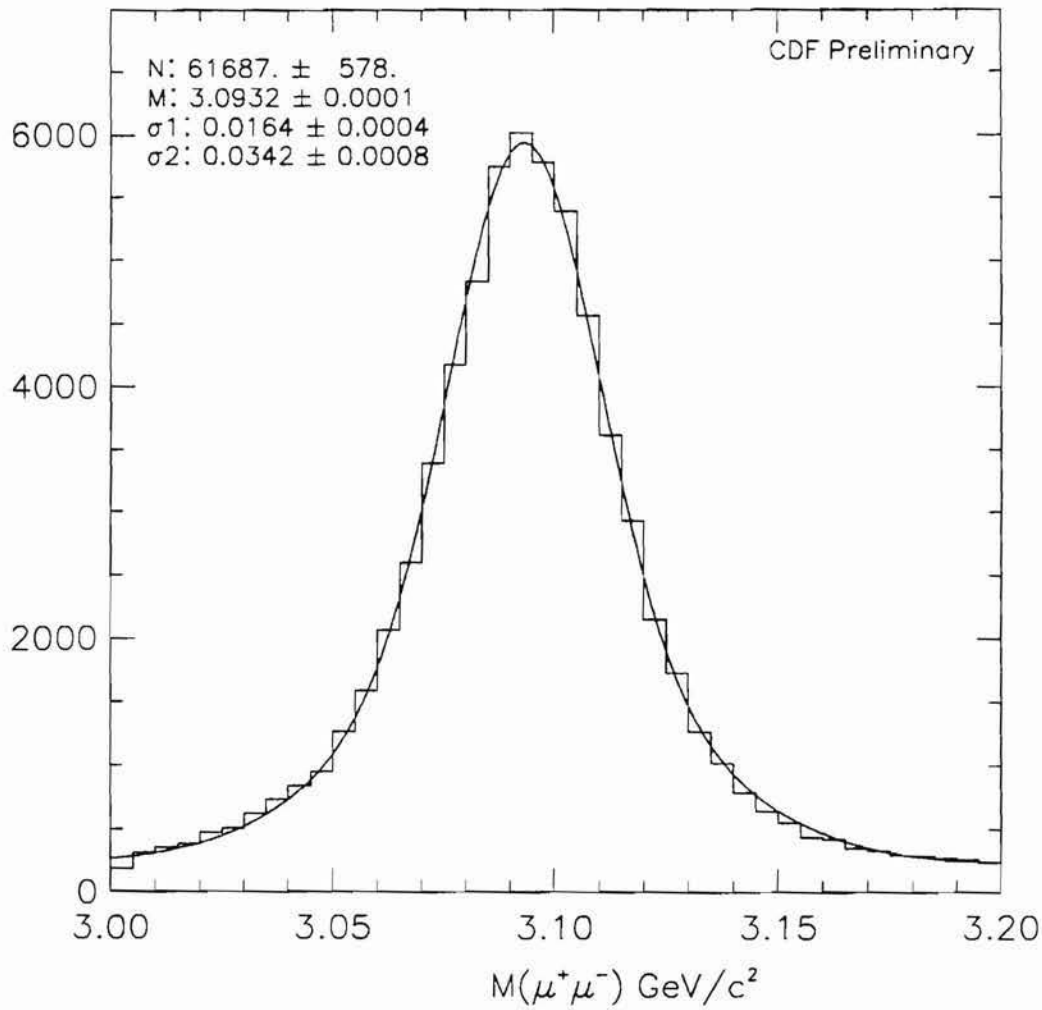

Figure 4.2

J/ψ invariant mass distribution reconstructed from the di-muon decay channel.

846 and 946 MeV/c^2. This represents the range $m(K^{*0}) \pm \Gamma$, where $m_(K^{*0})$ is the world average K^{*0} mass of 896 MeV/c^2, and Γ is the K^{*0} width of 49.8 MeV/c^2. Then, the kaon and pion mass assignments are reversed, and the invariant mass of the track pair is recalculated. In case both choices of mass assignments results in a two-track invariant mass within the K^{*0} mass window, the mass assignment choice that forms the K^{*0} candidate closest to the world average mass is selected. After pairs of tracks forming K^{*0} candidates are selected, they are refitted to a common vertex with the muons forming the J/ψ candidate, while the dimuon invariant mass is constrained to the the average J/ψ mass.

Given the number of degrees of freedom of the vertex fit, the confidence level of the χ^2 is calculated. Track combinations which are inconsistent with originating from the same vertex have very large χ^2, which results in candidates with χ^2 confidence levels near zero. The confidence level of the vertex fit χ^2 is required to be greater than 0.005 to remove such combinations.

If SVX information has been used in the tracks forming the B candidate vertex, an additional cut is made to enhance the signal-to-background ratio by requiring that the B vertex be distinct from the primary event vertex. The signed decay length in the B rest frame, $c\tau$, is calculated as follows:

$$c\tau = \frac{L_{xy} \cdot m_B}{p_T},$$

where L_{xy}, the projected decay length in the lab frame, is found by projecting the secondary vertex displacement vector onto the B transverse momentum. The factor m_B/p_T results from the Lorentz transformation of L_{xy} from the lab frame to the B rest frame.

In order to determine the appropriate momentum cut to apply to the kaon candidates, a sample of B mesons generated by Monte Carlo is compared to a sample of background events from the data. A description of the Monte Carlo sample can

be found in the next chapter. For the $B^{\pm} \rightarrow J/\psi K^{\pm}$ decay, the background sample consists of combinations of J/ψ candidates passing all selection cuts with any other track in the event. For the $B^0 \rightarrow J/\psi K^{*0}$ decay, the background consists of combinations of J/ψ candidates with any other pair of oppositely charged tracks in the event. A cut on the kaon p_T is applied, and the quantity S^2/B is calculated, where S is the fraction of signal events surviving the cut, and B is the fraction of background events passing the cut. The S^2/B distributions indicate a p_T cut of 1.25 GeV/c for both the $K^{\pm}$ from the $B^{\pm} \rightarrow J/\psi K^{\pm}$ decay and the K^{*0} from the $B^0 \rightarrow J/\psi K^{*0}$ decay. In addition, the transverse momentum of each $B^{\pm}$ and B^0 candidate is required to be greater than 6.0 GeV/c, which is the Monte Carlo prediction for the minimum B momentum necessary to produce decay products which pass all the other selection cuts.

4.5 Integrated Luminosity

The integrated luminosity at CDF is determined by directly measuring the number of $p - \overline{p}$ interactions. Scintillator paddles are placed around the beam pipe in the forward and backward regions of the detector. These are called the beam-beam counters, or BBC. A scaler is incremented each time a forward and a backward scintillator record a hit within a loose time window. The number of counts is then corrected for the angular acceptance of the scintillators, and for the detection efficiency and the efficiency of the time window requirement. The corrected number of counts is converted to the integrated luminosity using a recent measurement of the total $p - \overline{p}$ cross-section of 80.6 $\pm$ 2.3 mb [21]. This results in a measured total integrated luminosity for run 1A of (21.0 $\pm$ 0.8) pb^{-1} [22]. Portions of the data having problems with the online trigger system, the central muon chambers, or the CTC are excluded from the analysis. So the data sample

used for this analysis corresponds to an integrated luminosity of (19.4 ± 0.8) pb^{-1}.

Uncertainty in the determination of the integrated luminosity is dominated by uncertainty in correcting for the angular acceptance of the BBCs and for the efficiency of the time coincidence window required to register a BBC trigger. Another component comes from the uncertainty in the measurement of the $p-\overline{p}$ total cross-section.

4.6 Observed B Meson Signals

Figures 4.3 and 4.4 show the $B^{\pm}$ and B^0 invariant mass distributions after all the selection requirements have been applied. Each distribution is fitted to a Gaussian function, plus a flat background. The widths, σ, of the Gaussians are determined from Monte Carlo studies to be 12.4 MeV for $B^{\pm} \rightarrow J/\psi K^{\pm}$ and 11.1 MeV for $B^0 \rightarrow J/\psi K^{*0}$. The fit results in mass determinations of 5.2737 $\pm$ 0.0023 for $B^{\pm}$ and 5.2785 $\pm$ 0.0029 for B^0. Some $B^{\pm} \rightarrow J/\psi K^{\pm}$ candidates could be incompletely reconstructed $B^0 \rightarrow J/\psi K^{*0}$ decays, and with perfect mass resolution the invariant mass formed for these partially reconstructed B^0 mesons would lie at least one pion mass (140 MeV/c^2) below the B mass. A similar source of background for the $B^0 \rightarrow J/\psi K^{*0}$ decay arises from the decay $B^{\pm} \rightarrow J/\psi K^{\pm}$ $\pi^{\mp}\pi^{\pm}$. However, due to the finite mass resolution of 20 ± 10 MeV/c^2, some of the partially reconstructed decays may lie even closer to the B mass signal region. So to avoid overestimating the combinatoric background under the B mass peak, the invariant mass region below 5.20 GeV/c^2 is excluded from the fits. The fits result in a determination of 122 ± 16 $B^{\pm}$ and 75 ± 15 B^0 candidates over background.

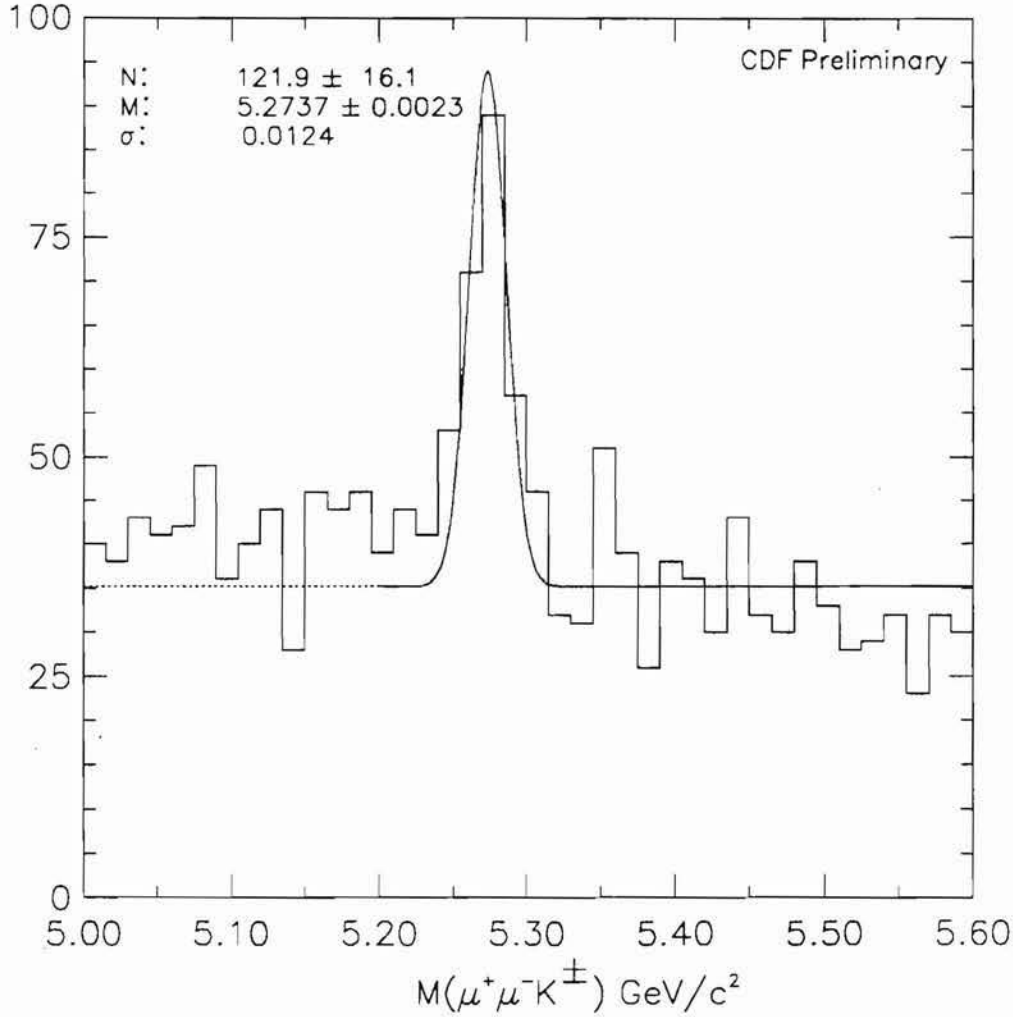

Figure 4.3

$B^{\pm}$ invariant mass distribution reconstructed from the decay $B^{\pm} \rightarrow J/\psi K^{\pm}$

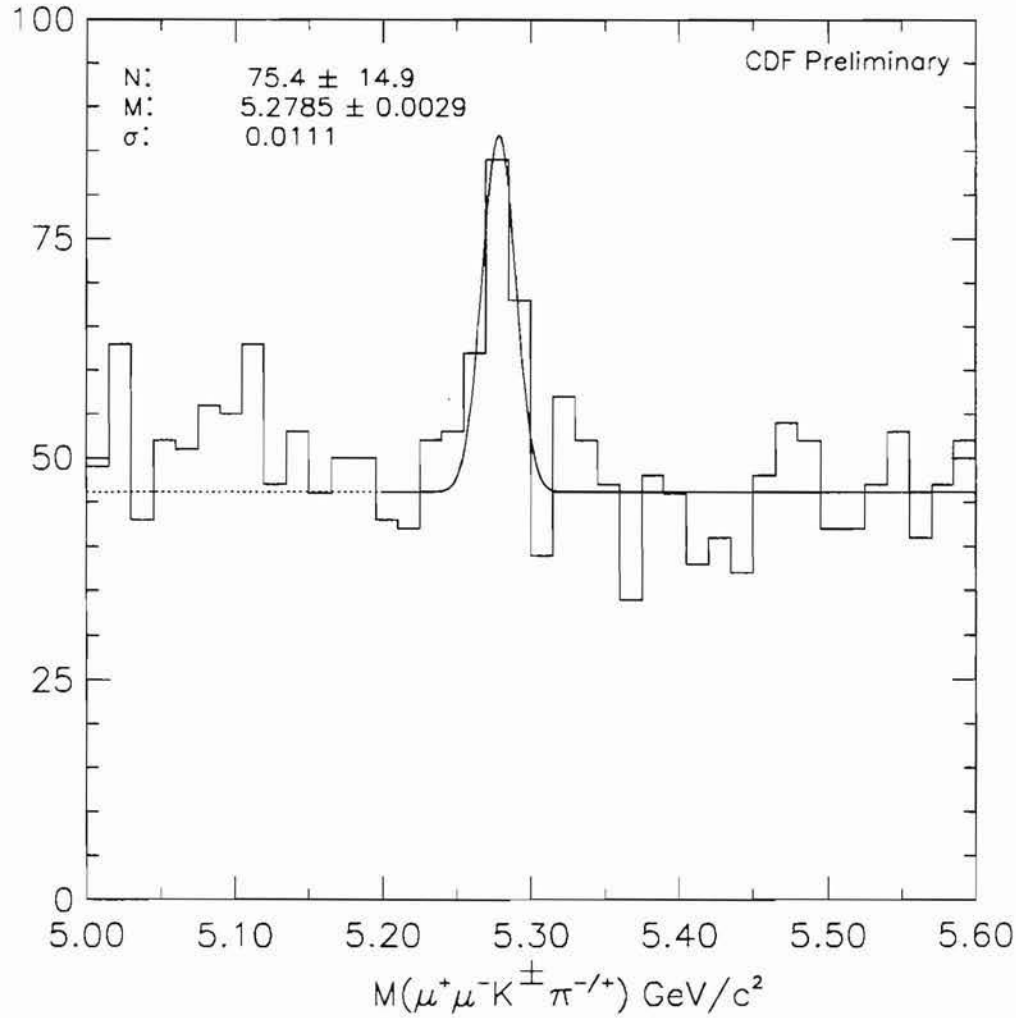

Figure 4.4

B^0 invariant mass distribution reconstructed from the decay $B^0 \to J/\psi K^{*0}$

5. DETECTOR ACCEPTANCE AND RECONSTRUCTION EFFICIENCY

Once the number of B meson candidates over background has been measured, measurements of the geometrical acceptance of the detector and reconstruction efficiencies are used to determine the total number of B mesons that were produced. In this chapter the method of determining the detector acceptance from a Monte Carlo event generator with a detector simulation is described, along with the methods of determining the track reconstruction, trigger, and selection cut efficiencies.

5.1 The CDF Detector Acceptance for B mesons

A Monte Carlo event generator, as well as detector and trigger simulations are used to determine the fraction of B mesons which have all their decay products reconstructed in the detector. This fraction will presented as a function of the B meson and b quark transverse momenta.

5.1.1 Monte Carlo Event Generator

To generate the B decays of interest, a Monte Carlo program is used. The Monte Carlo program employed for this analysis begins by generating a sample of b quarks with a transverse momentum distribution determined by the next-to-leading order QCD calculation described in chapter 2 using the MRSD'_- structure functions. After the b quark is produced, it is forced to fragment into a B^- or $\overline{B^0}$ meson. The fraction of the b quark momentum carried by the B meson is dis-

tributed according to the Peterson fragmentation function described in chapter 2. Measurements from several different inclusive leptons studies [15] give a combined result of $\epsilon = 0.006 \pm 0.001 \pm 0.002$ for the fragmentation function parameter. The B^- and $\overline{B^0}$ mesons are decayed with lifetimes of 1.61 ps and 1.57 ps, respectively, which are the lifetimes measured by CDF using exactly the same decay channels [23]. A decay package developed at CLEO, called QQ [24], is used to force the mesons to decay via the channels $B^- \rightarrow J/\psi K^-$ and $\overline{B^0} \rightarrow J/\psi \overline{K^{*0}}$, followed by $J/\psi \rightarrow \mu^+\mu^-$ and $\overline{K^{*0}} \rightarrow K^-\pi^+$. The results are later corrected for the most recent CLEO measurements of the branching ratios for the $B^\pm \rightarrow J/\psi K^\pm$ and $B^0 \rightarrow J/\psi K^{*0}$ decays, which are $(1.12 \pm 0.17) \times 10^{-3}$ and $(1.53 \pm 0.37) \times 10^{-3}$ [25], respectively. The decay package includes the measured polarization [25] of the $B^0 \rightarrow J/\psi K^{*0}$ decay products.

As discussed in chapter 2, the principal uncertainties in the b quark production are in the choice of scale, μ, and in the structure functions. The acceptance was calculated by using the scale $\mu_0 = \sqrt{{p_T}^2 + {m_b}^2}$. To see how the acceptance depends on the choice of μ, it is recalculated using $\mu = \mu_0/4$ and $\mu = 4\mu_0$. The structure function fit gave a value of the QCD parameter λ_4 of 230 ± 55 MeV [11]. λ_4 is varied within its errors and the acceptance is recalculated. With these variations, the acceptance changes by no more than $\pm 5\%$, which is taken as a contribution to the systematic uncertainty.

The B meson momentum spectrum depends on the value used for the fragmentation parameter, ϵ. The change in the acceptance found by varying ϵ within its error limits of 0.004 and 0.008 indicates a contribution to the systematic uncertainty of 7%.

For the $B^\pm \rightarrow J/\psi K^\pm$ decay, the fact that the B meson and the kaon are pseudo-scalar particles forces the vector J/ψ particle to be purely longitudinally

polarized. The decay package, QQ, incorporates this behavior. However, for the $B^0 \rightarrow J/\psi K^{*0}$ decay, having a pseudo-scalar particle decaying to two vector particles, the J/ψ polarization is not well determined *a priori*. The theoretical predictions are highly model dependent, and the best estimate for the J/ψ polarization comes from experimental measurements made at CLEO [25]. The latest such measurement determined that the J/ψ is $(84 \pm 10)\%$ longitudinally polarized in this decay. Varying the polarization used in simulating this decay within the errors changes the acceptance by 7%, which is taken as a contribution to the systematic uncertainty.

5.1.2 Detector Simulation

After the momenta of the B decay products have been generated, the particle tracks are simulated using a program called QFL. QFL propagates the particles through the magnetic field and uses the known resolutions of each detector component to smear out the measured track helix parameters. It also incorporates the geometrical distribution of matter in the detector to simulate multiple Coulomb scattering and energy lost by particles as they pass through matter.

A contribution to the systematic uncertainty of 4% is assigned to the kaon reconstruction efficiency determined in the detector simulation. The simulation predicts that 8% of kaons decay in flight, and half of these are successfully reconstructed in the simulated data. It is believed that the ability to reconstruct such tracks is modeled realistically in the simulation, but due to possible discrepancies between the amount and distribution of material in the simulation compared to the actual detector, the systematic uncertainty is taken to be equal to half the fraction of simulated kaon decays in flight.

5.1.3 J/ψ Trigger Simulation

The geometrical acceptance for muons from the B meson decays being studied is taken to be the fraction of all muons simulated by QFL which have a central muon chamber track segment. However, the muons in the data sample used for this analysis were also required to pass the J/ψ Level 1 and Level 2 trigger requirements. So a simulation of the triggers has been included in the acceptance calculation. This simulation randomly rejects muon candidates with a probability determined by the trigger inefficiencies.

The level 1 muon trigger efficiency was determined by analyzing a data sample containing events that passed a single muon trigger. Some of these events also contained a second muon. The invariant mass of the trigger muon and any other muon in the event was formed. J/ψ candidates were identified in the mass distribution, and the second (non-trigger) muon leg was considered to be a good muon candidate. Since the second muon was not required to pass the Level 1 trigger, it could be used to provide an unbiased estimate of the trigger efficiency. The fraction of non-trigger J/ψ muon legs that passed Level 1 was calculated as a function of the muon transverse momentum, and is shown in figure 5.1 [26].

It was shown in chapter 4 that the angle between a muon chamber track segment and the radial direction is a measure of the muon transverse momentum. But due to multiple scattering and energy lost by the muon when passing through the calorimeters, the angle of the track only approximates the initial p_T of the muon, which results in the broad turn-on evident in figure 5.1. The trigger efficiency was parameterized by fitting the points in figure 5.1 to an error function, where the fitted parameters are the plateau efficiency and $p_{T_{crit}}$, the transverse momentum value that would correspond to the angle cut in the absence of material.

The level 2 trigger efficiency is simply a measure of the CFT tracking efficiency,

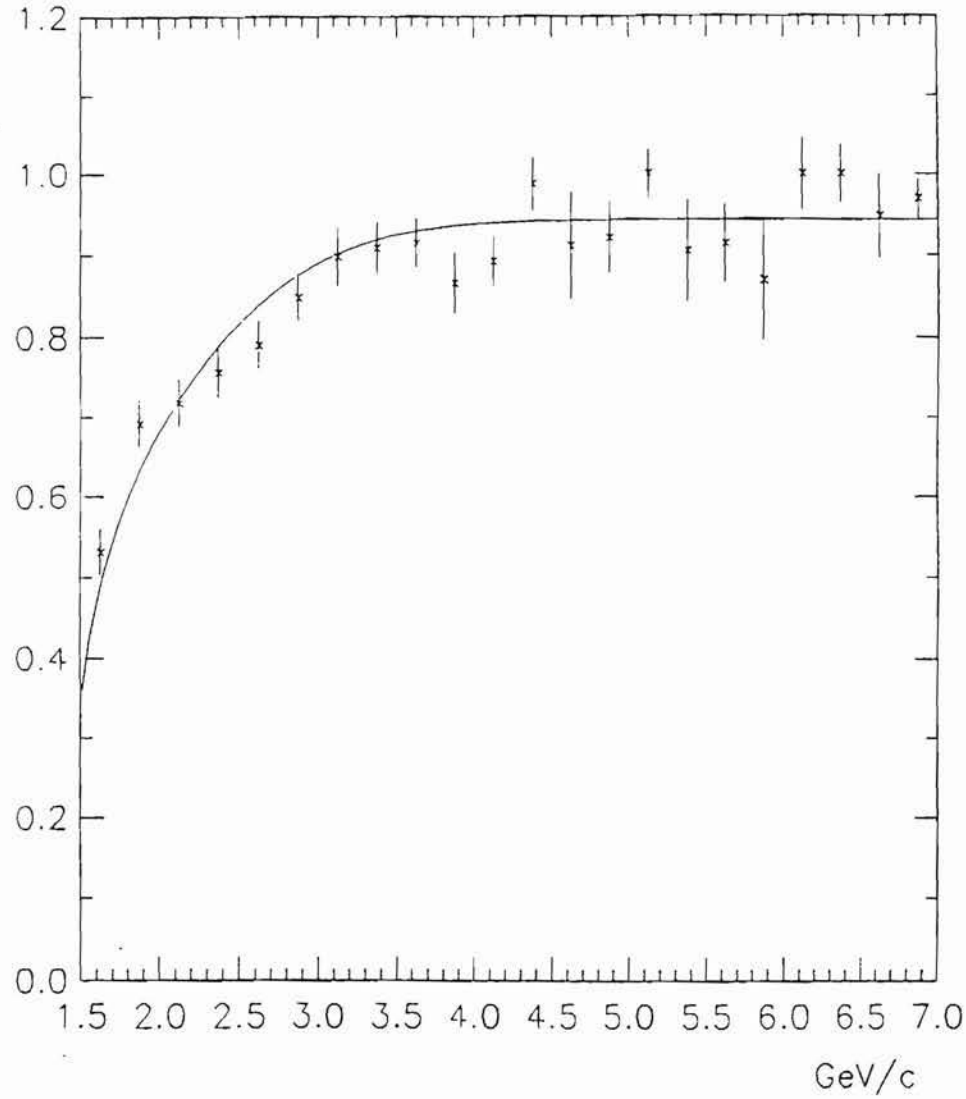

Figure 5.1

Level 1 muon trigger efficiency versus transverse momentum. The rightmost bin contains all data for the p_T range 6.75 to 10.0 GeV/c.

which is determined by the roads that have been defined for the CFT pattern recognition algorithm. The efficiency was determined directly from the J/ψ data sample used for the cross-section analysis. For all J/ψ candidates, one muon leg which had an associated CFT track, and therefore passed level 2, was identified. Then, the fraction of second legs which also have an associated CFT track was determined. This efficiency was also fit to an error function, and in this case the fitted parameters were the plateau efficiency and the nominal minimum p_T allowed by the roads that have been defined. The Level 2 trigger efficiency parameterization is shown as a function of p_T in figure 5.2.

A final step in the trigger simulation incorporates a limitation of the Level 1 trigger hardware. If adjacent muon chamber modules both have track segments, these are considered to form only one muon candidate at Level 1. So any simulated dimuon pairs which are not separated by at least one empty muon chamber module are removed from the sample.

The change in the simulated trigger efficiency that results from varying the Level 1 and Level 2 parameterizations by $\pm 1\sigma$ indicates a contribution to the systematic uncertainty of 4%.

5.1.4 Combined Geometrical Acceptance and Trigger Efficiency

If the detector simulation results in two muons detected in the muon chambers which pass the trigger simulation filter, then the fraction of B mesons for which the other decay particles were reconstructed in the CTC is determined. The combined acceptance and trigger efficiencies versus the B^- and $\overline{B^0}$ meson p_T are shown in figures 5.3 and 5.4, respectively. These acceptance curves are combined in the Monte Carlo with the momentum distribution to get the total acceptance for B mesons above the minimum momentum cut-off. The combined acceptance and

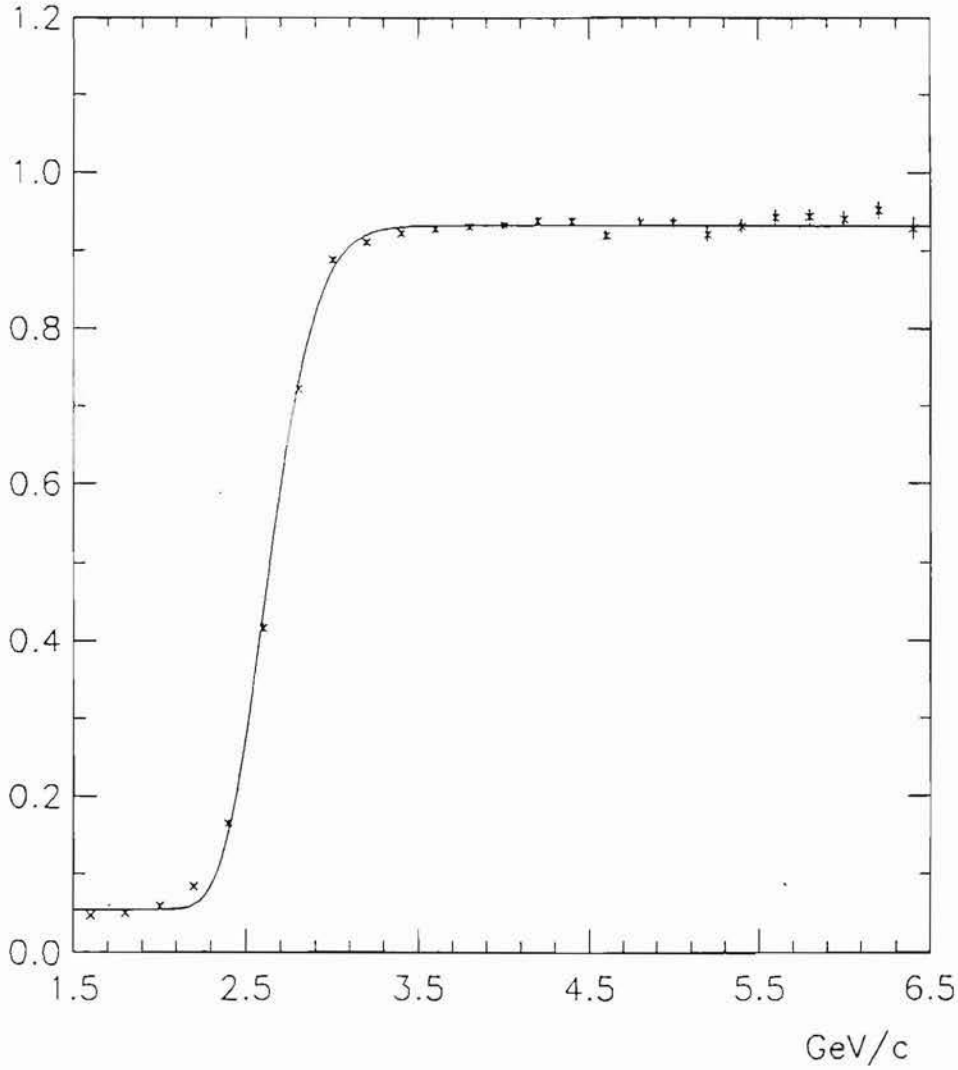

Figure 5.2

Level 2 muon trigger efficiency. The low statistical error on the points is due to the fact that the entire J/ψ data sample is used for the measurement.

muon trigger efficiency for B^- mesons with $p_T \geq 6.0$ GeV/c is determined to be 6.48 ± 0.06 % and for $\overline{B^0}$ mesons with $p_T \geq 6.0$ GeV/c is determined to be 4.93 ± 0.04 %, where the uncertainty comes from the statistical error in the Monte Carlo sample.

5.2 Efficiency of the Offline Selection Requirements

5.2.1 J/ψ Selection Requirements

Muons forming J/ψ candidates were required to pass selection cuts based on the χ^2 of the match between the intercepts of the muon chamber track segment and the CTC track, in both the $r-\phi$ and z directions. The matching cuts applied are $\chi^2(r-\phi) < 9.0$ and $\chi^2(z) < 12.0$. The efficiency of these cuts was determined from a sample of J/ψ candidate events containing muons which were only required to pass the looser Level 3 matching requirements of $\chi^2(r-\phi) < 16.0$ and $\chi^2(z) < 16.0$. In each event, a muon was randomly chosen, and if it passed the matching cuts, the invariant mass of the dimuon pair was calculated. The efficiency of the cuts was found by dividing the number of J/ψ for which the second muon leg also passed the cuts by the number of J/ψ for which at least the first leg passed the cuts. The efficiency of requiring both J/ψ muons to pass the cuts is then the product of the efficiency for each muon to pass the cuts, and was determined to be 98.7 $\pm$0.2% [27]. The uncertainty is due to the statistical error on the fits to the J/ψ invariant mass distributions.

The J/ψ mass resolution depends on whether or not SVX information is used for tracking the muons. Figure 5.5 shows the J/ψ width for all three combinations of tracks that can be used to reconstruct a J/ψ candidate. The width varies by 30% depending on whether two CTC-only or two SVX tracks are used. The normalized

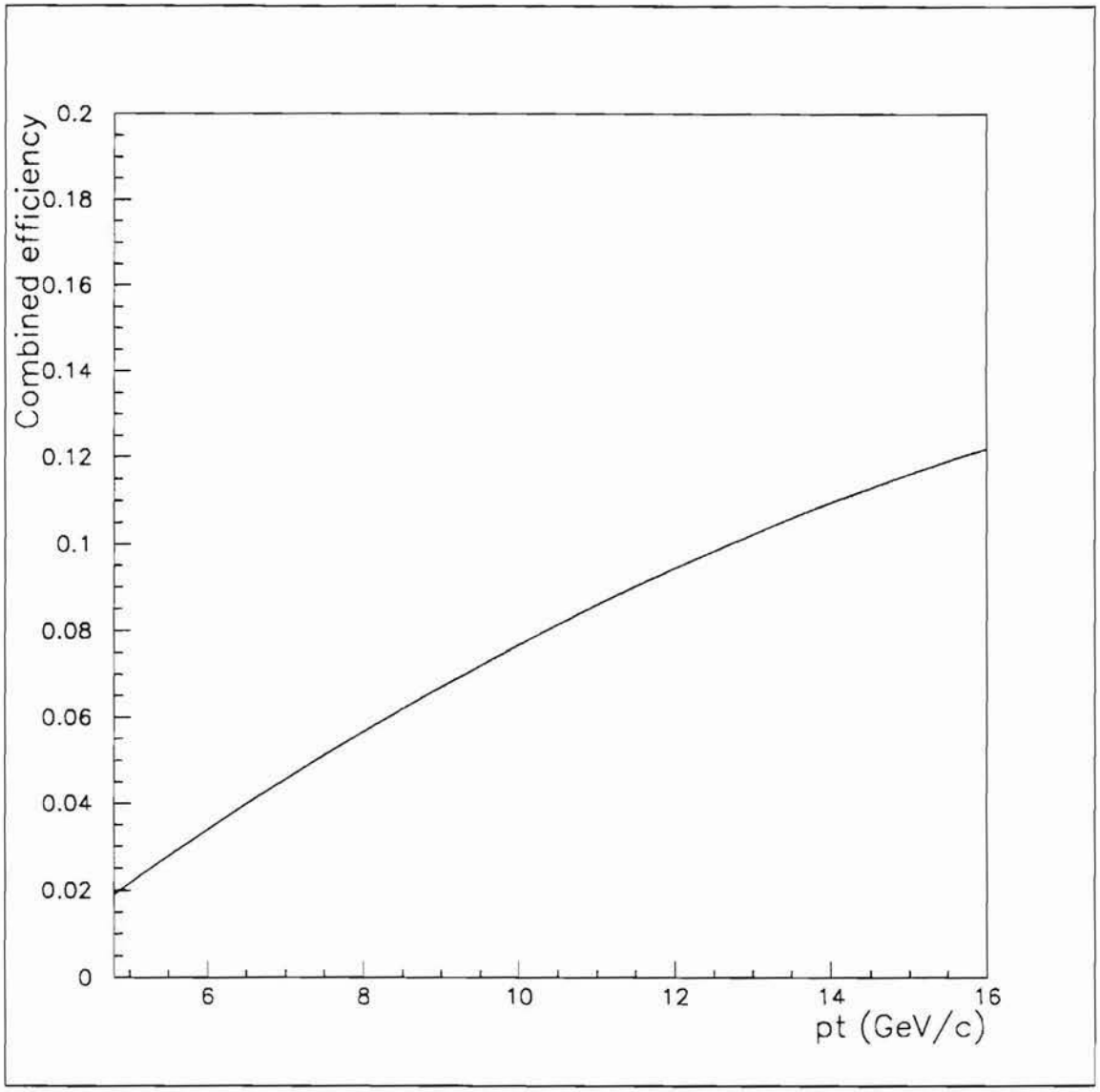

Figure 5.3

Combined acceptance and dimuon trigger efficiency for J/ψ versus the transverse momentum of the B^- meson.

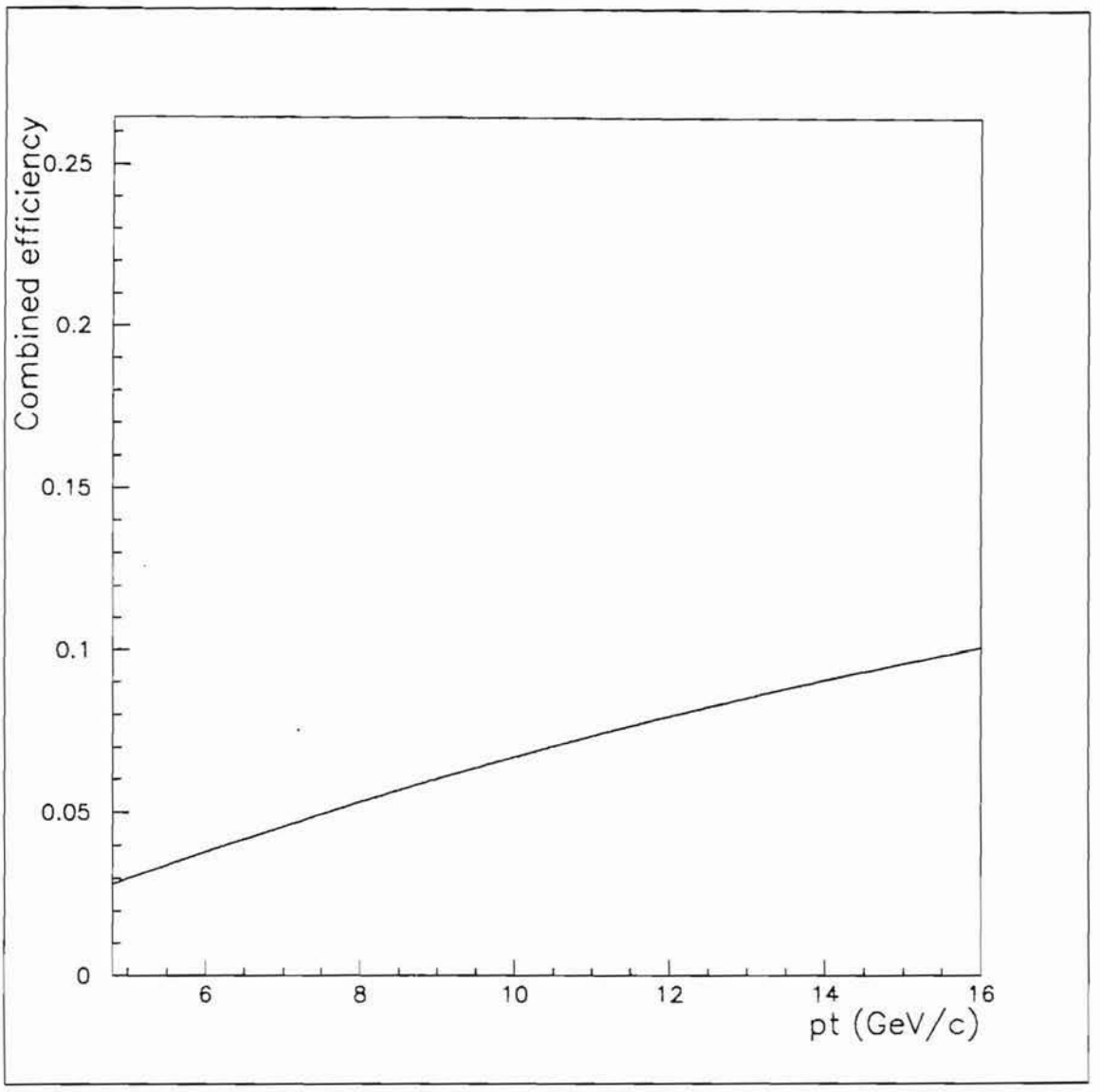

Figure 5.4

Combined acceptance and dimuon trigger efficiency for J/ψ versus the transverse momentum of the $\overline{B^0}$ meson.

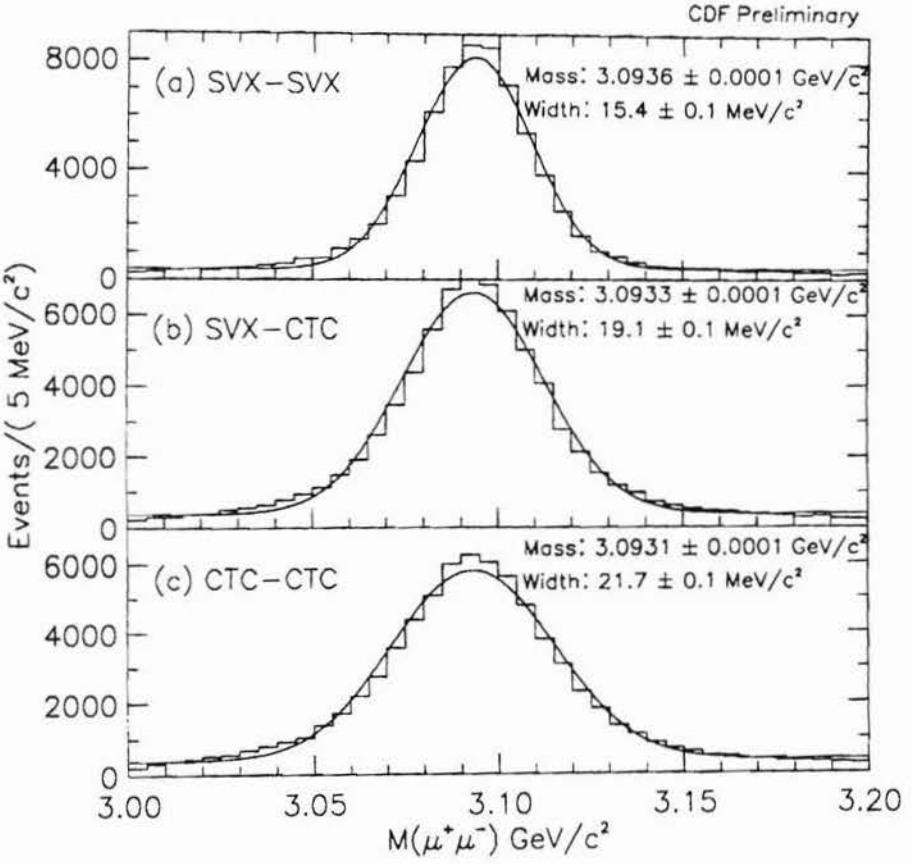

Figure 5.5

J/ψ mass width for the three tracking combinations (a) SVX-SVX, (b) SVX-CTC, and (c) CTC-CTC.

J/ψ mass is defined as

$$\frac{\Delta m}{\delta m} \equiv \frac{m_{\mu\mu} - m_{J/\psi}}{\delta_m}$$

where δ_m is the estimated error on the invariant mass calculation. The normalized mass distribution has a width which is less sensitive to what tracking information is used than the absolute J/ψ mass distribution, since the difference in CTC and SVX tracking errors is reflected in δ_m. Figure 5.6 shows the normalized mass distributions for all three tracking combinations. The widths of these distributions vary by 15%. The mass window cut was chosen to be $\pm 3\hat{\sigma}$, where $\hat{\sigma} = 1.37 \pm 0.01$ is taken from the width of the Gaussian fitted to the SVX-SVX distribution, which is the widest of the three distributions. Given this choice, the efficiency of the mass window cut for J/ψ reconstructed from two SVX tracks is simply the fraction of the area of the Gaussian lying within the mass window, which is 99.7%. For J/ψ reconstructed from other track combinations, the efficiency can be up to 0.3% higher. Ideally, if the error on the mass determination were correctly estimated, the width of these distributions would be 1. The fact that these widths are greater than 1 indicates that some of the tracking parameter errors are underestimated.

5.2.2 Other Offline Selection Requirements

The efficiency of the other selection requirements is determined directly from the B Monte Carlo simulation. A decay length cut and the kaon transverse momentum cuts are applied to the simulated data sample, and the fraction passing each cut is determined. The motivation for the selection cuts and the associated systematic uncertainties are discussed in the next sections.

5.2.2.1 Decay Length Requirement

Since less than 20% of J/ψ in the data sample are from B decays, a cut on the

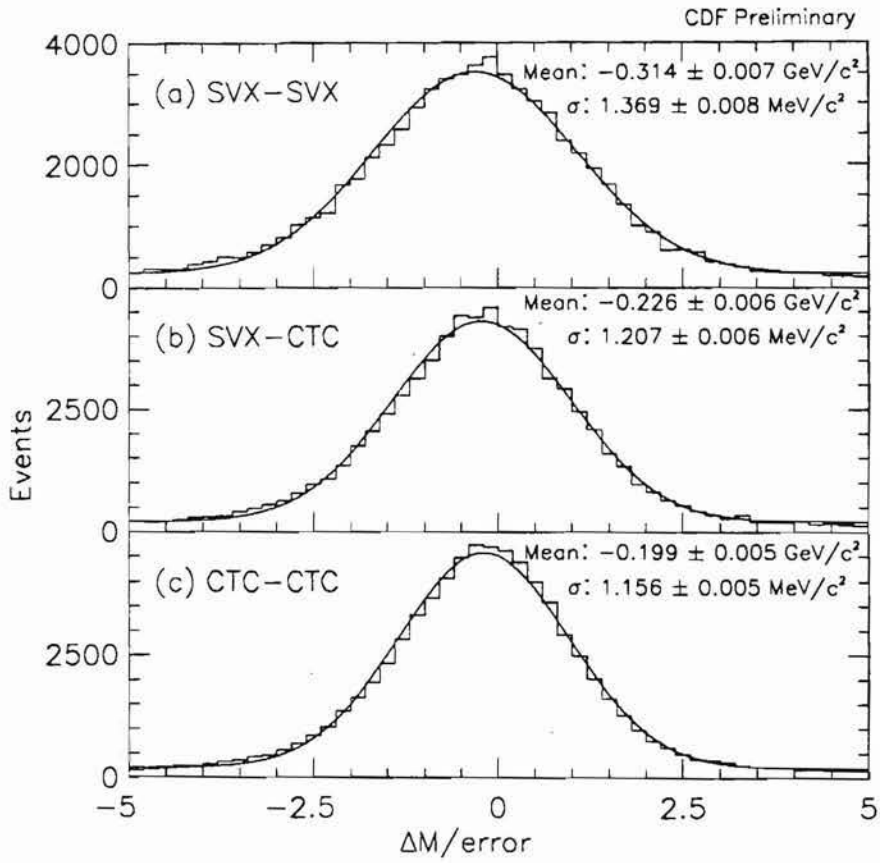

Figure 5.6

$(m_{\mu\mu} - m_{J/\psi})/\delta_m$ for the three tracking combinations (a) SVX-SVX, (b) SVX-CTC, and (c) CTC-CTC.

decay length of the B candidate serves to greatly reduce the principal source of background, which is a prompt J/ψ combined with other tracks originating from the primary vertex.

CDF has already submitted for publication new measurements of the B meson lifetime, using exactly the same decays that are used for the cross-section measurement[23]. Given the lifetime for $B^{\pm}$ mesons of $c\tau_{\pm} = 483 \pm 50\mu m$, the efficiency of a selection cut on $c\tau$ of 100 μm is approximately $exp(-100/483) = 81.3\%$. The exact efficiency of the cut depends on the resolution of the $c\tau$ measurement, which, in turn, depends on how many tracks forming the vertex have SVX information. The resolution for each combination was determined by fitting the width of the distribution of the $c\tau$ measurements for B candidates in the lower and upper sideband mass regions of $5.145 - 5.22 GeV/c^2$ and $5.34 - 5.415 GeV/c^2$. Since these are background events, they have an average $c\tau$ of 0. The measured $c\tau$ distributions are shown in figure 5.7 for the cases where 3, 2, 1, and 0 SVX tracks are used to reconstruct the B vertex. The widths of these distributions are approximately 75, 95, 250, and 350 μm, respectively.

The $c\tau$ cut efficiency is calculated as a function of the $c\tau$ resolution. The probability for a B meson which decays at an actual $c\tau$ less than the cut of $100\mu m$ to have a measured $c\tau$ which passes the cut is determined by the Gaussian resolution of the measured $c\tau$ and on the difference between the actual value of $c\tau$ and the cut of 100 μm. The probability for a B meson with actual $c\tau$ greater than 100 μm to fail the cut is determined in the same manner. To determine the overall effect on the efficiency of the cut, the probability of passing the cut is integrated over all values of $c\tau$. Figure 5.8 shows the calculated efficiency versus resolution, using the charged B lifetime measurement of $c\tau_{\pm} = 483 \pm 50\mu m$[23]. A similar plot is shown in figure 5.9, using the neutral B lifetime measurement of $c\tau_0 = 471 \pm 59\mu m$. The

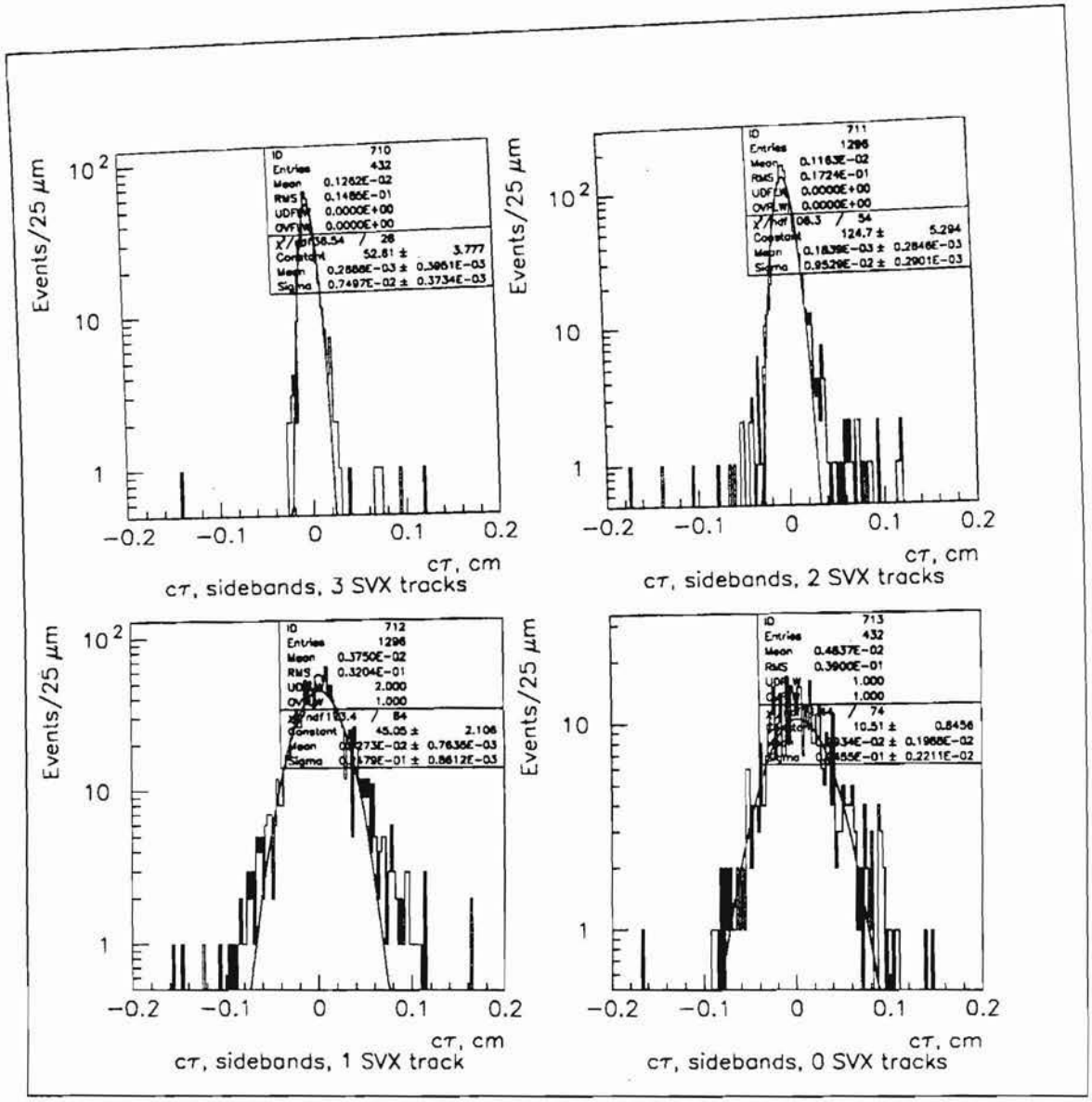

Figure 5.7

$c\tau$ resolution for sideband regions for the four possible tracking combinations.

efficiency varies by 8% over the resolution range from 0 to 350 μm. The Monte Carlo simulation is used to determine the $c\tau$ cut efficiency, and the $\pm 4\%$ variation with the $c\tau$ resolution is taken as the size of the contribution to the systematic uncertainty.

5.2.2.2 Vertex Selection Efficiency

After applying the $c\tau$ cut, the sample of B candidates is enriched with J/ψ from displaced secondary vertices. The remaining background is largely composed of such J/ψ vertexed with tracks coming from the primary vertex. This source of background is reduced by applying a cut on the confidence of the vertex fit χ^2.

The fact that the $\Delta m/\delta m$ distributions do not have width one is an indication that some of the errors on the track helix parameters may be underestimated. If so, this could also cause the vertex fits of tracks from real B decays to have larger than expected χ^2. In figure 5.10, the confidence level of the vertex fit χ^2 for the $B^{\pm}$ candidates in the sample is shown. B candidates reconstructed from sets of tracks which clearly do not belong to the same vertex have very large χ^2, which is reflected in the spike in the confidence near zero. The vertex fit χ^2 probability is required to be greater than 0.005 to eliminate such candidates. But the rise in the distribution below 0.2 is indicative of the underestimation of the tracking errors. In figures 5.11 and 5.12 the $B^{\pm}$ candidate mass distribution for tracks passing and failing the probability cut is shown. The B invariant mass distribution for candidates passing the probability cut is fitted to a Gaussian plus a linear background. Then the fit is applied to candidates failing the probability cut, fixing the mean and width of the fitted Gaussian to be the same as was found for the distribution of candidates passing the cut. There is no evidence for a B signal among these candidates; although the size of the background is twice as

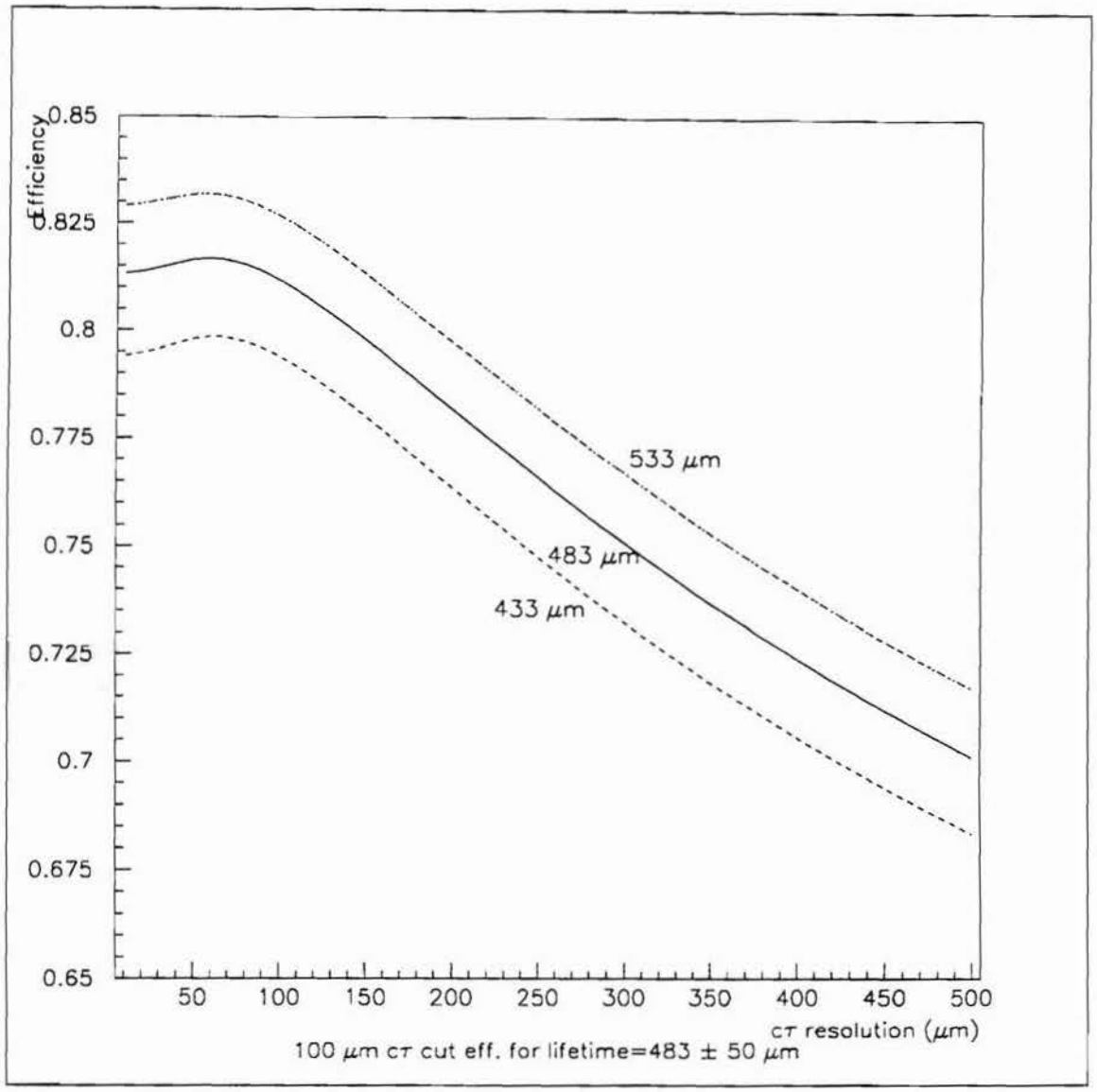

Figure 5.8

$c\tau$ cut efficiency for $B^{\pm}$ lifetime of $483 \pm 50\ \mu m$ as a function of the $c\tau$ resolution.

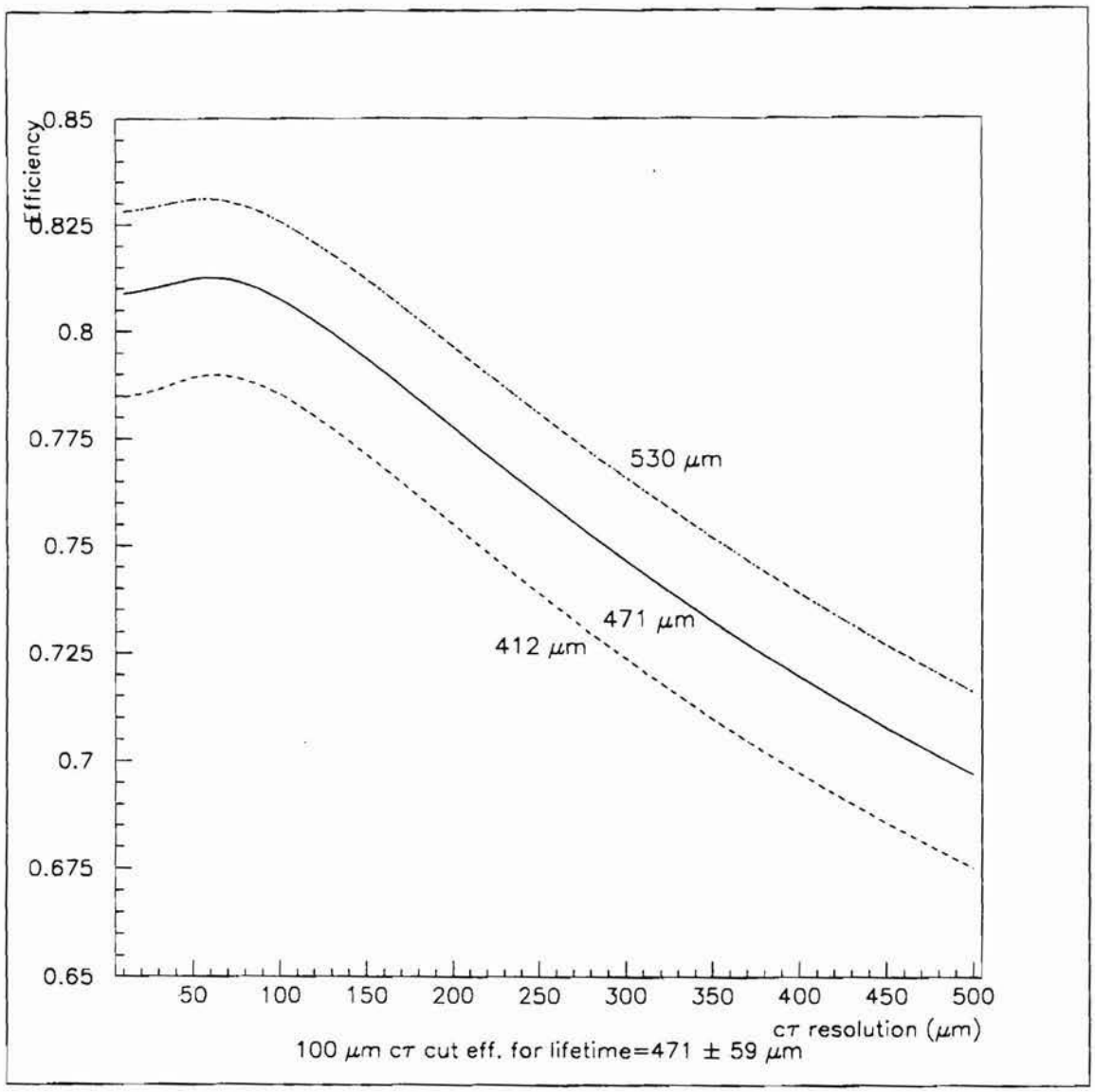

Figure 5.9

$c\tau$ cut efficiency for B^0 lifetime of 471 ± 59 μm as a function of the $c\tau$ resolution.

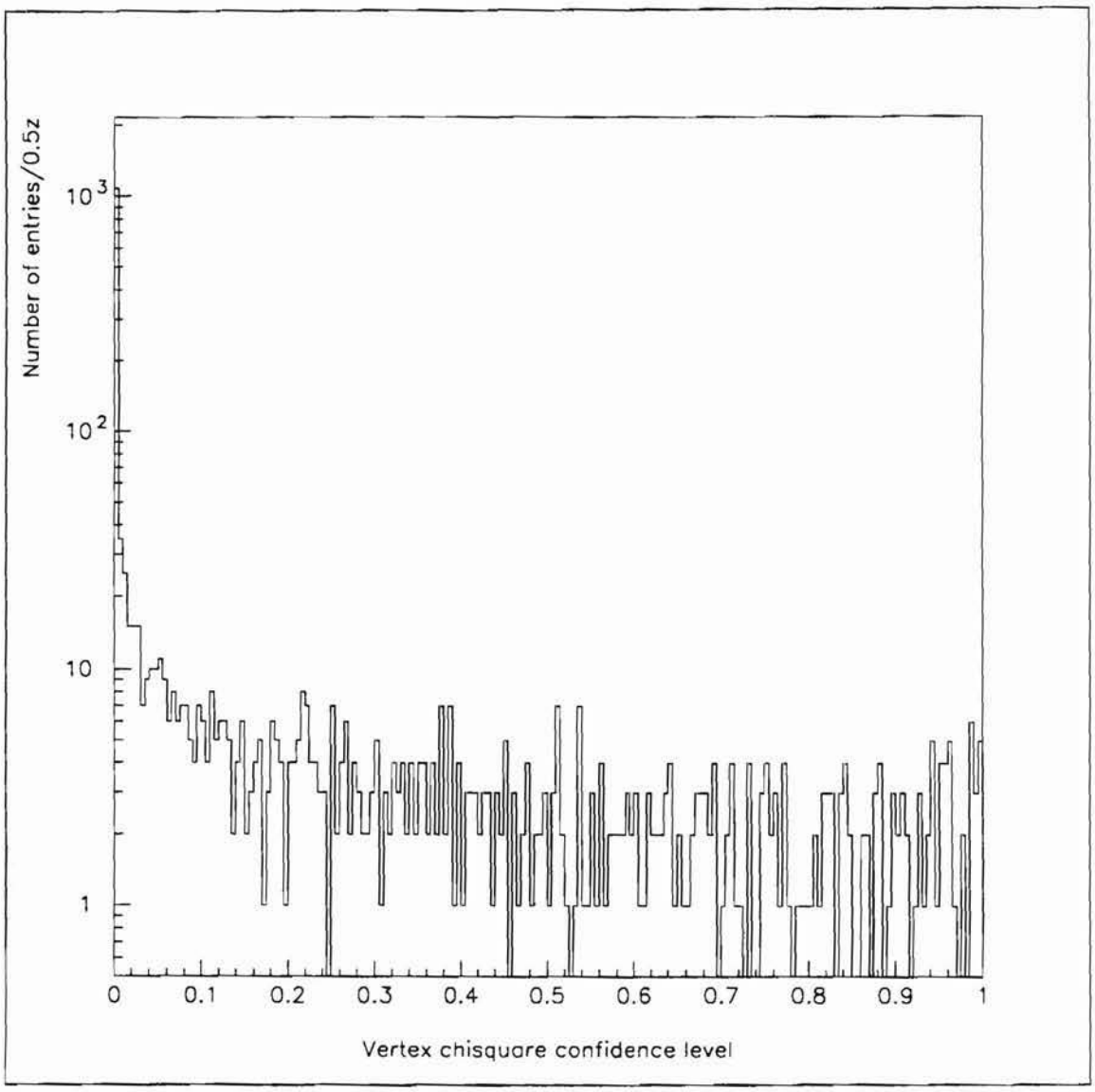

Figure 5.10

Vertex χ^2 confidence level distribution for the $B^{\pm}$ candidates passing all selection cuts.

MINUIT χ^2 Fit to Plot 555&0
MASS, PROB .GT.0.005
File: [MWB]BMASS_PROB.HST;1
Plot Area Total/Fit 1281.0 / 978.95 Fit Status 3
Func Area Total/Fit 1213.6 / 941.95 E.D.M. 2.211E−06
χ^2= 28.5 for 31 − 5 d.o.f., C.L.= 33.6%

Errors		Parabolic	Minos	
Function 1: Gaussian Distribution (sigma)				
AREA	143.85	±18.88	−0.0000E+00	+0.0000E+00
MEAN	5.2793	±2.1325E−03	−0.0000E+00	+0.0000E+00
SIGMA	1.55113E−02	±2.1699E−03	−0.0000E+00	+0.0000E+00
Function 2: Polynomial of Order 1				
NORM	26.743	±1.221	−0.0000E+00	+0.0000E+00
POLY01	−10.696	±7.152	−0.0000E+00	+0.0000E+00
★OFFSET	5.3000	±0.0000E+00	−0.0000E+00	+0.0000E+00

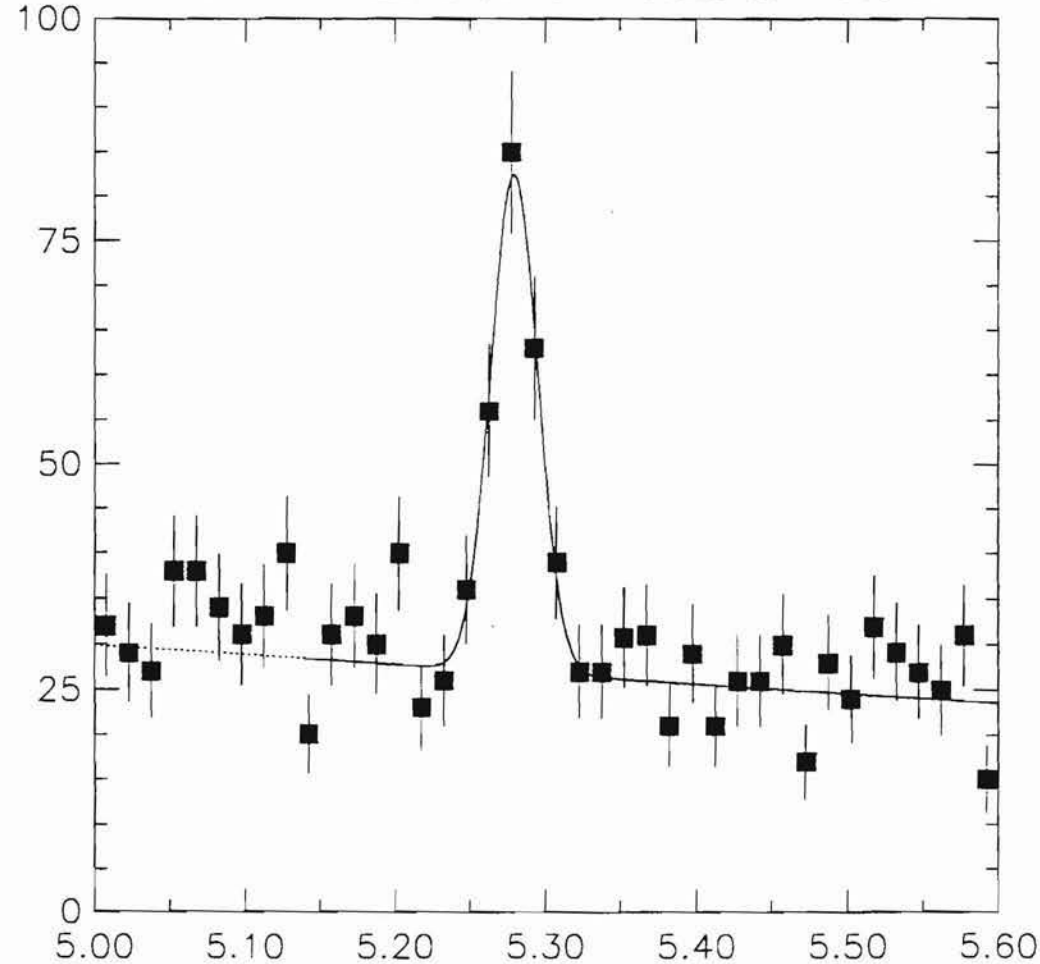

Figure 5.11

B mass distribution, for B candidates which have a vertex χ^2 confidence level > 0.005.

MINUIT χ^2 Fit to Plot 444&0
MASS, PROB .LT.0.005
File: [MWB]BMASS_PROB.HST;1
Plot Area Total/Fit 1600.0 / 1203.0 Fit Status 3
Func Area Total/Fit 1550.7 / 1165.3 E.D.M. 4.450E−24
χ^2= 23.9 for 31 − 2 d.o.f., C.L.= 73.2%

Errors		Parabolic	Minos	
Function 1: Gaussian Distribution (sigma)				
AREA	−8.3763	±12.26	−12.26	+12.26
★MEAN	5.2793	±0.0000E+00	−0.0000E+00	+0.0000E+00
★SIGMA	1.55109E−02	±0.0000E+00	−0.0000E+00	+0.0000E+00
Function 2: Polynomial of Order 1				
NORM	38.977	±1.178	−1.178	+1.178
★POLY01	−10.693	±0.0000E+00	−0.0000E+00	+0.0000E+00
★OFFSET	5.3000	±0.0000E+00	−0.0000E+00	+0.0000E+00

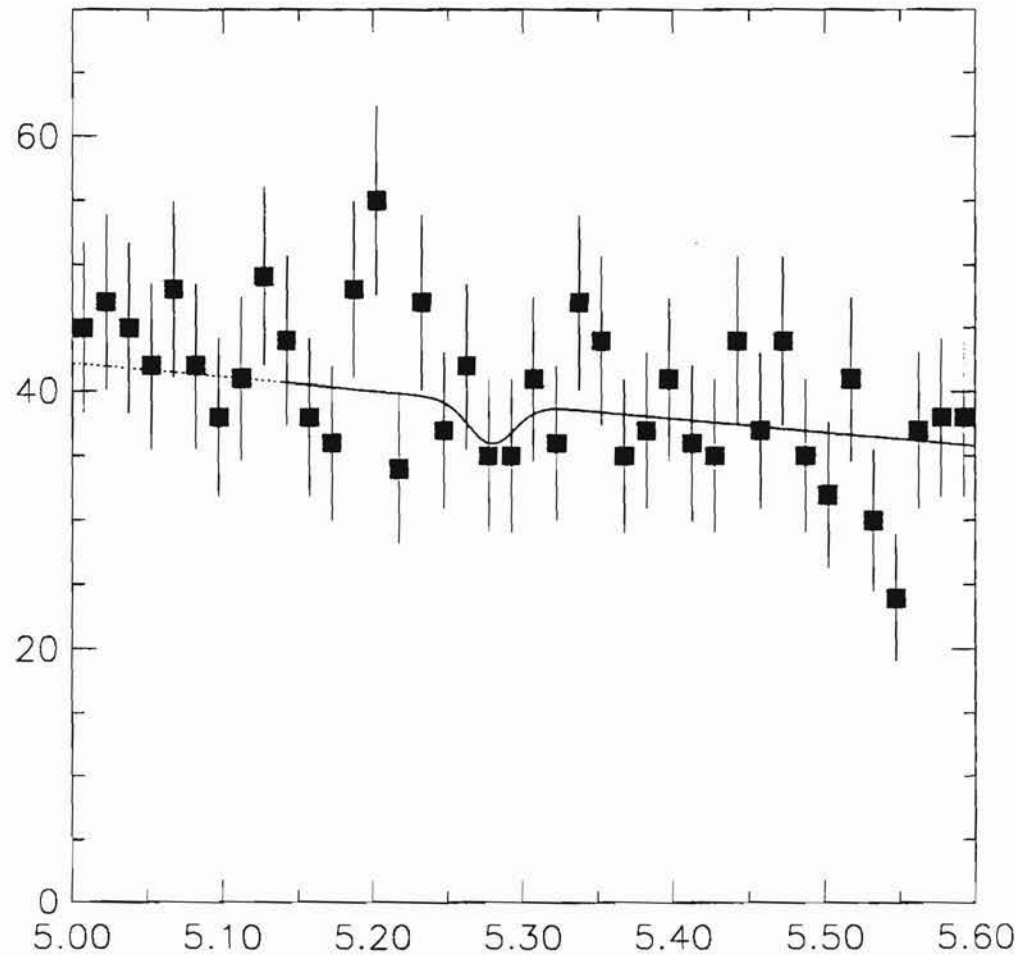

Figure 5.12

B mass distribution, for B candidates which have a vertex χ^2 confidence level < 0.005.

large as for candidates passing the cut. However, the statistical uncertainty in this fit allows there to be up to three signal events in the the sample failing the probability cut.

A similar probability distribution is observed for the J/ψ vertex. The high statistics allows the efficiency of the probability cut to be determined directly. In figure 5.13 the J/ψ mass distribution is shown before applying the cut and in figure 5.14 is the mass distribution after the probability cut of 0.005 has been applied. The distributions are fit to two gaussians plus a constant background. 64070 $\pm$ 620 J/ψ pass the cut, out of a total of 64990 $\pm$ 650, indicating an efficiency of 98.6 $\pm$ 1 %.

Since this number is statistically consistent with the efficiency of 99.5% expected for perfectly determined track errors, and since no B candidates are apparent in the sample failing the cuts, the efficiency of the probability cut on the B vertex is also taken to be 98.6 $\pm$ 1 %.

5.3 Tracking Efficiencies

One drawback of the QFL detector simulation, is that it is perfectly efficient at reconstructing any particle tracks that is contained within the detector volume. Since the true detector tracking efficiency is not perfect, it is necessary to apply an additional correction for this.

The tracking efficiencies can be broken down into three parts. The first part is the efficiency of the tracking that is done at Level 3 of the trigger system. Inefficiencies in the tracking of the muons at this stage can cause the event to be rejected from the data sample. Once an event has been accepted at Level 3, the second part is the efficiency of CTC retracking which is done offline. This stage may improve the track quality, or find new tracks that were missed at level 3. The

MINUIT χ^2 Fit to Plot 200&0
J/ψ mass, prob gt. 0.005
File: [MWB]PSIMASS_PASSFAILPROB.HST;1
Plot Area Total/Fit 73410. / 73410. Fit Status 1
Func Area Total/Fit 73273. / 73273. E.D.M. 1.220E−14
χ^2= 136.1 for 40 − 6 d.o.f., C.L.=0.373E−11%

Errors		Parabolic	Minos	
Function 1: Two Gaussians (sigma)				
AREA	64067.	±624.2	−0.0000E+00	+0.0000E+00
MEAN	3.0932	±1.0394E−04	−0.0000E+00	+0.0000E+00
SIGMA1	1.63463E−02	±3.5776E−04	−0.0000E+00	+0.0000E+00
AR2/AREA	0.46818	±2.5220E−02	−0.0000E+00	+0.0000E+00
★DELM	0.00000E+00	±0.0000E+00	−0.0000E+00	+0.0000E+00
SIG2/SIG1	2.1265	±4.9547E−02	−0.0000E+00	+0.0000E+00
Function 2: Polynomial of Order 0				
NORM	233.68	±13.55	−0.0000E+00	+0.0000E+00

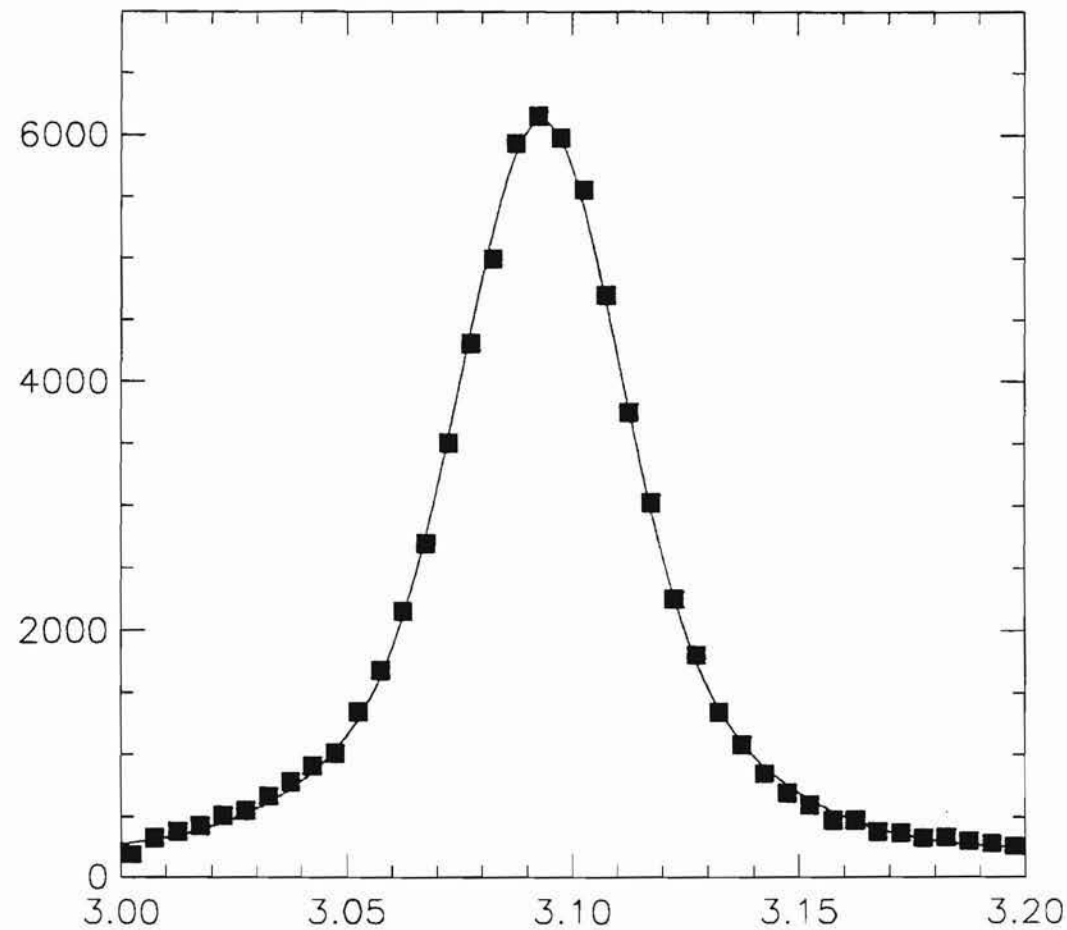

Figure 5.14

J/ψ mass distribution, for J/ψ candidates which have a vertex χ^2 confidence level > 0.005.

third part is the SVX tracking efficiency for tracks that were found in the CTC.

5.3.1 Online Tracking Efficiency

Two methods were used to determine the Level 3 online tracking efficiency. The first method used the data from a Level 3 tagging run (in which all events that pass Level 2 triggers are written out) to measure the fraction of J/ψ events that were identified by the Level 3 tagging. The dimuon invariant mass distribution for muon pairs which passed and failed Level 3 were separately fitted to a Gaussian at the J/ψ mass. A second method consisted of scanning events with an event display and locating CTC hit patterns that follow a circular path, but for which no track was reconstructed at Level 3. Combining the results of the two methods gave an online Level 3 dimuon tracking efficiency of $97 \pm 2\%$.

5.3.2 CTC Offline Tracking Efficiency

Since Level 3 online tracking is a simplified version of the track reconstruction that is done offline, it is assumed that all muons identified by Level 3 can be reconstructed offline. However, it is still necessary to correct for the track-finding efficiencies for the other B decay products. The method uses CTC hits for a track generated by simulation which are overlaid on a real data event. The reconstructed track parameters from one of the J/ψ muons, except for ϕ, are used as input to the detector simulation. ϕ is altered by two different methods. In the first method, the simulated track is flipped in ϕ about the other muon momentum vector. In the second method, the simulated track is flipped in ϕ about the original J/ψ momentum vector. For each of these methods the simulated hits are then embedded in the data event from which the initial muon was taken. The standard track reconstruction is performed, and the fraction of time the embedded track is suc-

cessfully reconstructed is measured. The efficiency determined by this method was 98.9±1.0%, where the uncertainty is derived from the dependence of the measured efficiency on which method of altering ϕ is chosen.

Above a transverse momentum of 1 GeV/c, the CTC tracking efficiency is independent of the charge or mass of a pion or kaon whose track is being reconstructed. So even though the tracking efficiency is determined by using muon tracks, it is still applicable to other particle types, as well. The advantage of this method is that it creates a realistic environment of noise hits and nearby real tracks, and so reproduces the typical demand on the pattern recognition algorithm that occurs in the data.

5.3.3 SVX Tracking Efficiency

In this section, the measurement of the SVX tracking efficiency is described. It should be understood that since CTC tracks are required in the formation of SVX tracks, the efficiencies quoted are relative to the CTC tracking efficiency. The tracking efficiency will be broken down into the individual layer hit efficiencies, which will be shown as functions of p_T, ϕ, and z.

The tracks used for this measurement are the muons forming J/ψ candidates as described in chapter 4. In addition, the Level 1 and Level 2 trigger requirements on the muons are removed for this study. This increases the number of muons available at lower momentum.

As a measure of the intrinsic performance of the detector, the layer hit efficiencies versus p_T for the muon tracks are calculated by evaluating. The hit efficiency is found by evaluating

$$\frac{N_{i+3}}{N_3}$$

where N_{i+3} is the number of tracks for which a hit is found on layer i, as well as

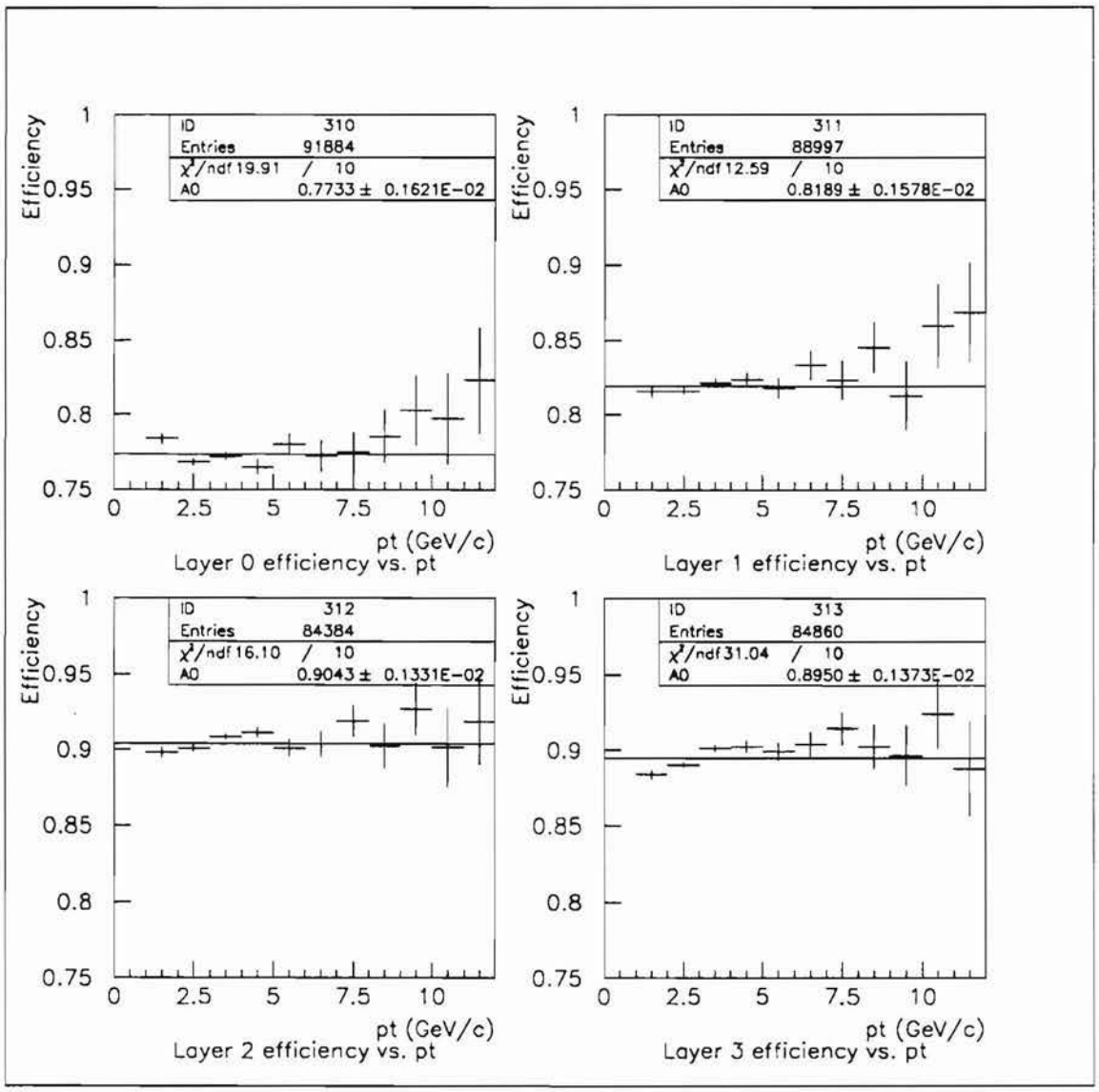

Figure 5.15

SVX layer efficiencies for muons from J/ψ versus the transverse momentum of the muon.

the other three layers, and N_3 is the number of tracks for which the other three layers had hits, but layer i may, or may not, have had a hit. The hit efficiencies are shown in table 5.1 and the p_T dependence is shown in figure 5.15.

Given the individual layer hit efficiencies, the total tracking efficiencies for tracks which are completely contained in the active detector region can be calculated. The results are shown in table 5.2

In figure 5.16, the layer hit efficiencies as functions of ϕ for tracks passing the fiducial cut are shown. The ϕ gaps in layer 0 which were present at the time of construction are clearly visible. The dip in efficiency near $\phi = 0$ in layer 1 is due to a known dead readout chip. In figure 5.17, the layer efficiencies as a function of the z-intercept of the track with the layer are shown.

The overall SVX tracking efficiency as a function of p_T for all muons that pass the SVX selection criteria is shown in figure 5.18. The distribution has been fitted with a straight horizontal line over the p_T range 1.0 to 12.0 GeV/c, resulting in a tracking efficiency of 87.3 $\pm$ 0.1%. The efficiency is lower than that calculated from the individual layer hit efficiencies because it includes tracks that are near the z-boundaries. In order to provide a consistency check on the method, the total efficiency is measured for tracks which pass a tight fiducial cut in the z-intercept of the track with each layer. From figure 5.17 this fiducial cut is determined to be $7 \leq |z| \leq 21cm$, which is 5-6 cm away from the nominal z boundaries of the active regions of the detector. The SVX tracking efficiency for tracks satisfying such a fiducial cut is found to be 96.5 $\pm$ 0.8 %, which is in better agreement with the 2-hit probability of 98.9$\pm$ 0.013 % computed from the individual layer hit efficiencies. The 2% discrepancy can be explained by correlations in the layer hit efficiencies. For example, particles crossing the silicon at shallow angles will deposit more charge in all layers than particles crossing at normal angles, so the

Table 5.1

SVX individual layer hit efficiencies from muon tracks for which the other three layers had hits.

Layer Number	Hit efficiency
0	0.773 ± 0.005
1	0.819 ± 0.006
2	0.904 ± 0.006
3	0.895 ± 0.006

Table 5.2

Probability for an SVX track to be found with 2, 3, or 4 hits, calculated from the individual layer hit efficiencies.

Number of hits	Efficiency
≥ 2	0.989 ± 0.013
≥ 3	0.8937 ± 0.011
4	0.5193 ± 0.008

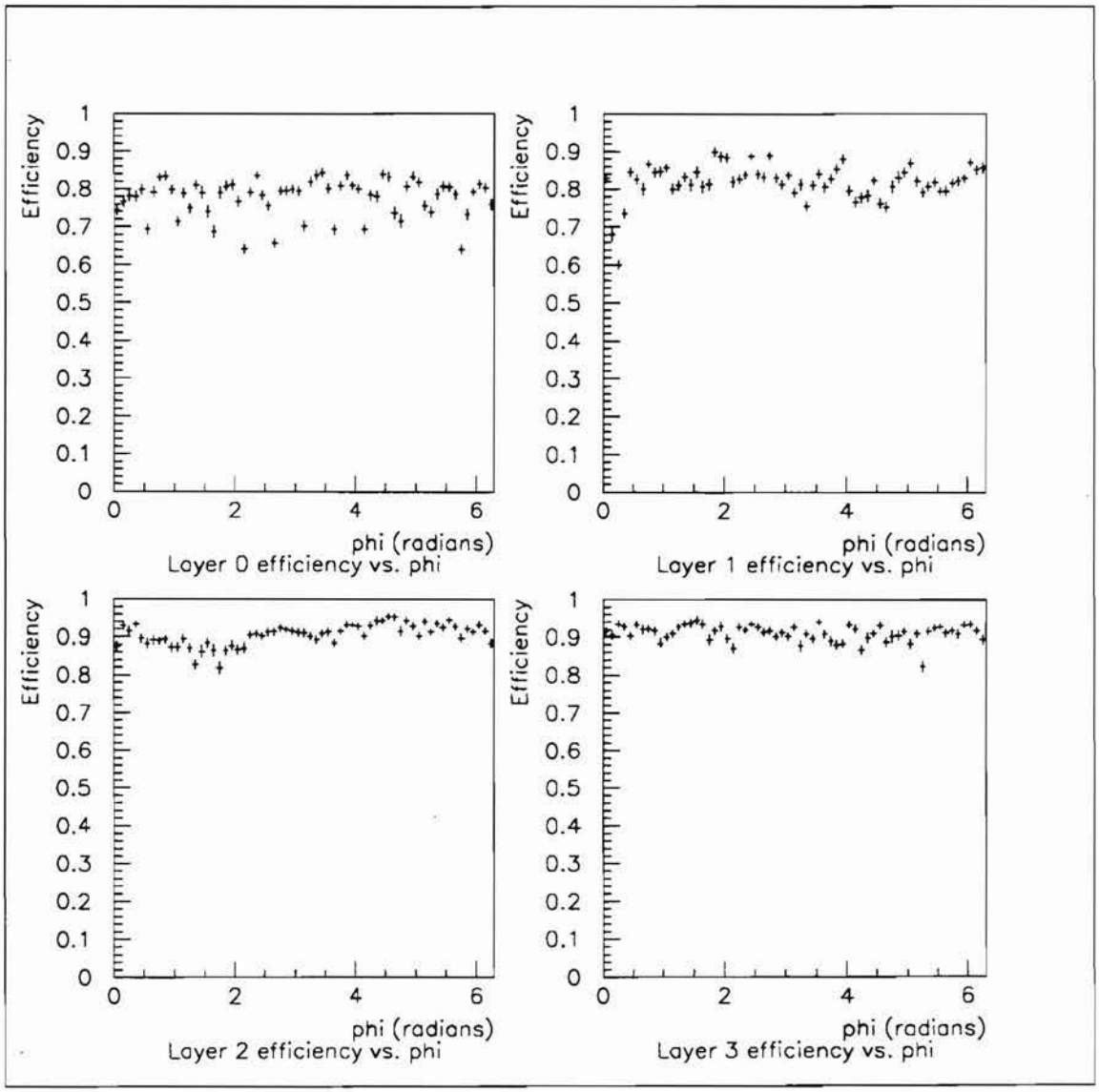

Figure 5.16

Layer hit efficiencies vs ϕ, for tracks passing the z fiducial cut.

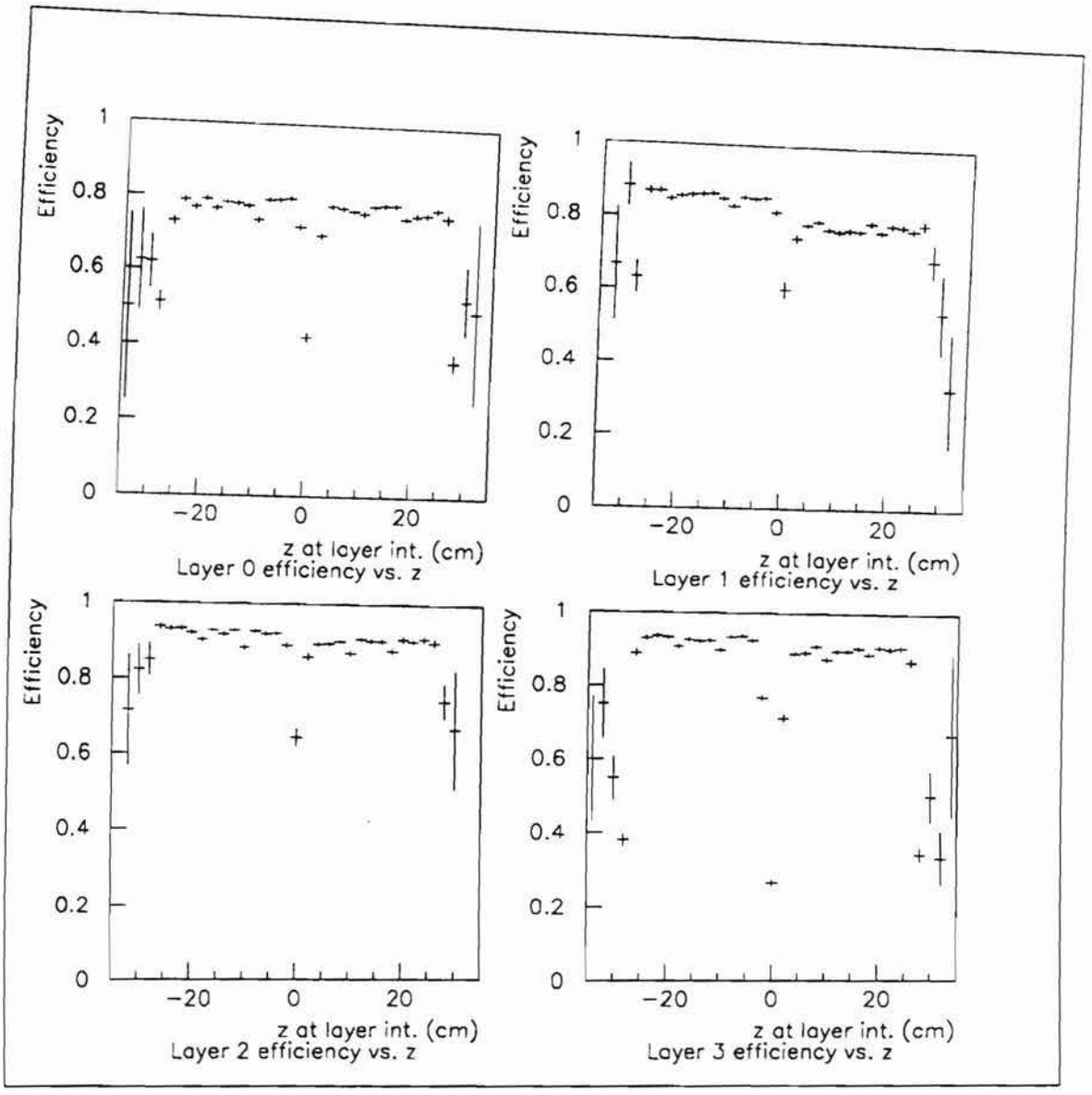

Figure 5.17

Layer hit efficiencies vs z-intercept of the track with the layer.

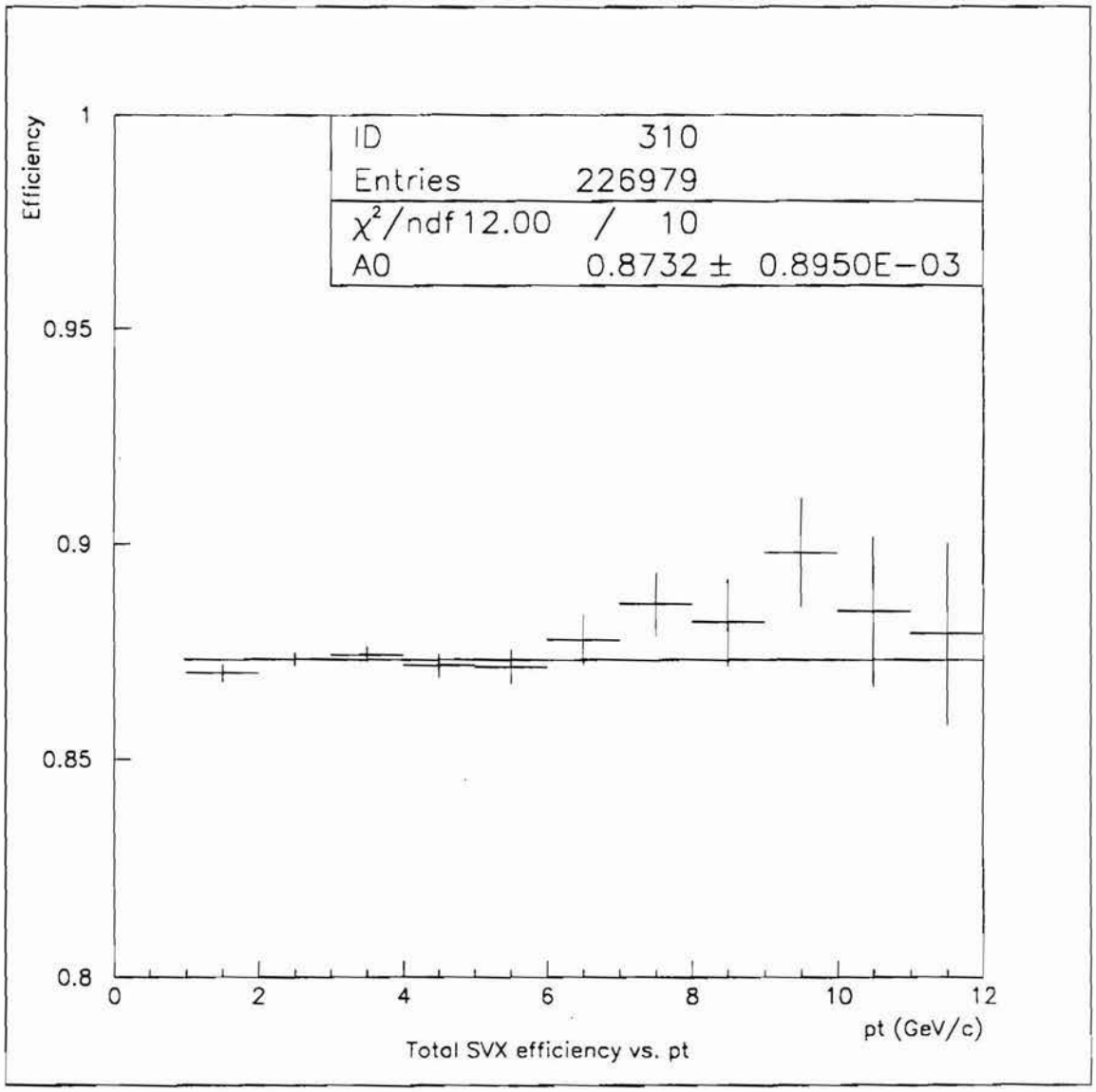

Figure 5.18

SVX tracking efficiency for muons from J/ψ. Fit is made to a constant efficiency, between muon transverse momenta of 1 and 12 GeV/c.

hit efficiency for all layers will be enhanced for such particles. Also for tracks in dense jets, there will be more clusters found on each layer than for isolated tracks, so tracks in dense jets would also have a higher hit efficiency for each layer.

It is possible that the SVX tracking efficiency for a J/ψ muon could depend on the number and distribution of other tracks in the event. The event topology for the inclusive J/ψ sample could be different on average than for the sample of J/ψ from B decays. Any dependence of the efficiency on the event topology should be reflected in a measurement of the efficiency as a function of the projected distance between the primary vertex and the J/ψ vertex, L_{xy}, which is shown in figure 5.19. This is because as L_{xy} increases from 0 to several hundred microns, the background fraction drops and the J/ψ muons will be drawn from events having topologies characteristic of B decays. The efficiency distribution is quite flat over the whole range of ± 4 mm. A horizontal line fit to the data points results in an efficiency of 88.21 ± 0.11 %. A 1% systematic uncertainty is assigned for the difference in the fitted efficiencies versus p_T and L_{xy}, resulting in an SVX tracking efficiency of 87.3 ± 1.0 %. While the efficiency was measured using muons, it should be equally valid for kaons and pions in J/ψ events with momentum greater than 1 GeV/c.

Another possible source of uncertainty comes from how B candidates are reconstructed when SVX information is available for only some of the tracks. As shown in figure 5.20, 12.3% of J/ψ candidates have SVX information for one muon leg, but not for the other. Some quantities, such as the J/ψ mass resolution, could vary depending on which mixtures of tracking information are used.

To study these effects, the subset of J/ψ candidates for which SVX tracks are found for both of the muon legs is used. Various quantities are calculated, then the SVX information is dropped for one, or both, of the muons legs and the same

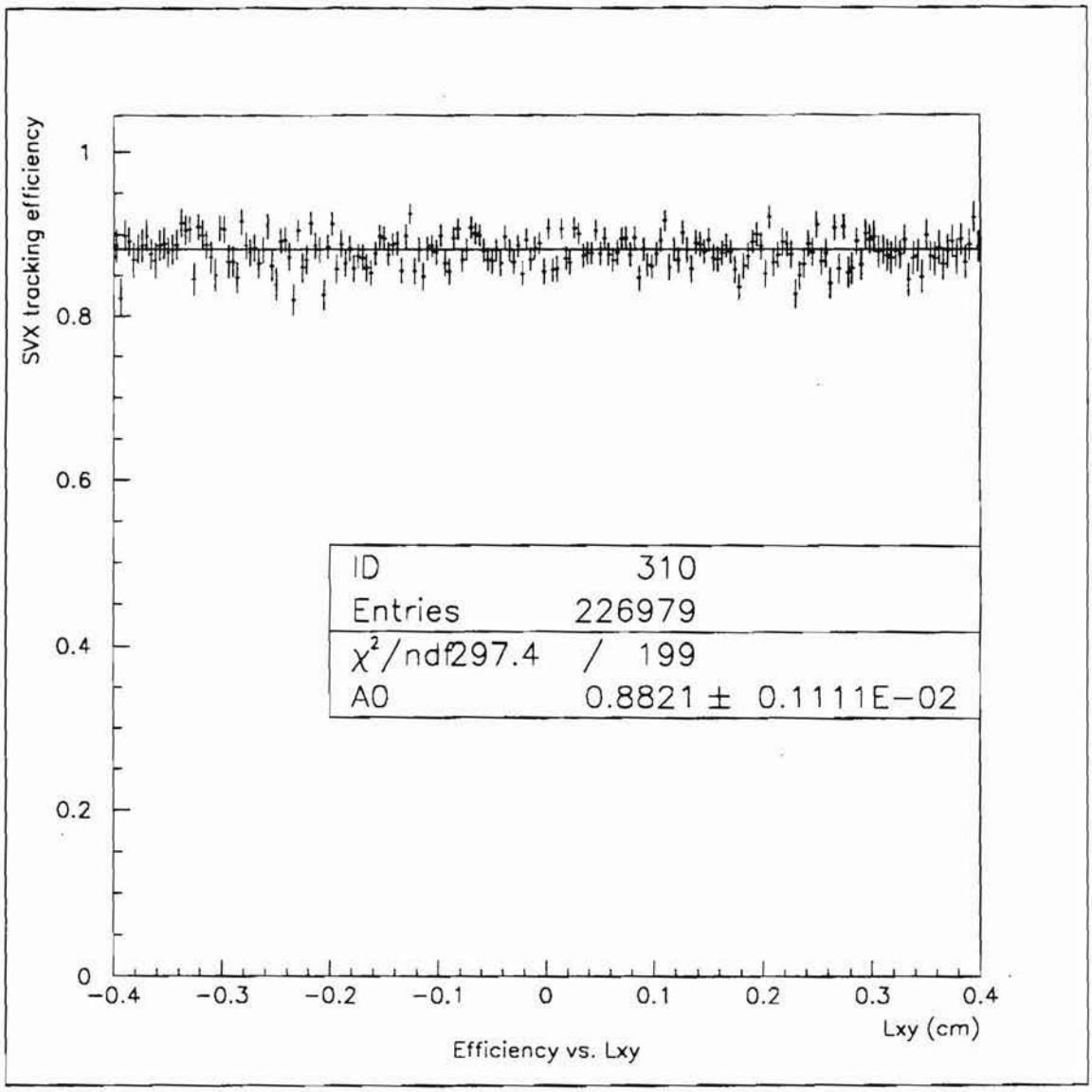

Figure 5.19

SVX tracking efficiency for muons from J/ψ versus L_{xy}, the decay length projected onto the p_T vector.

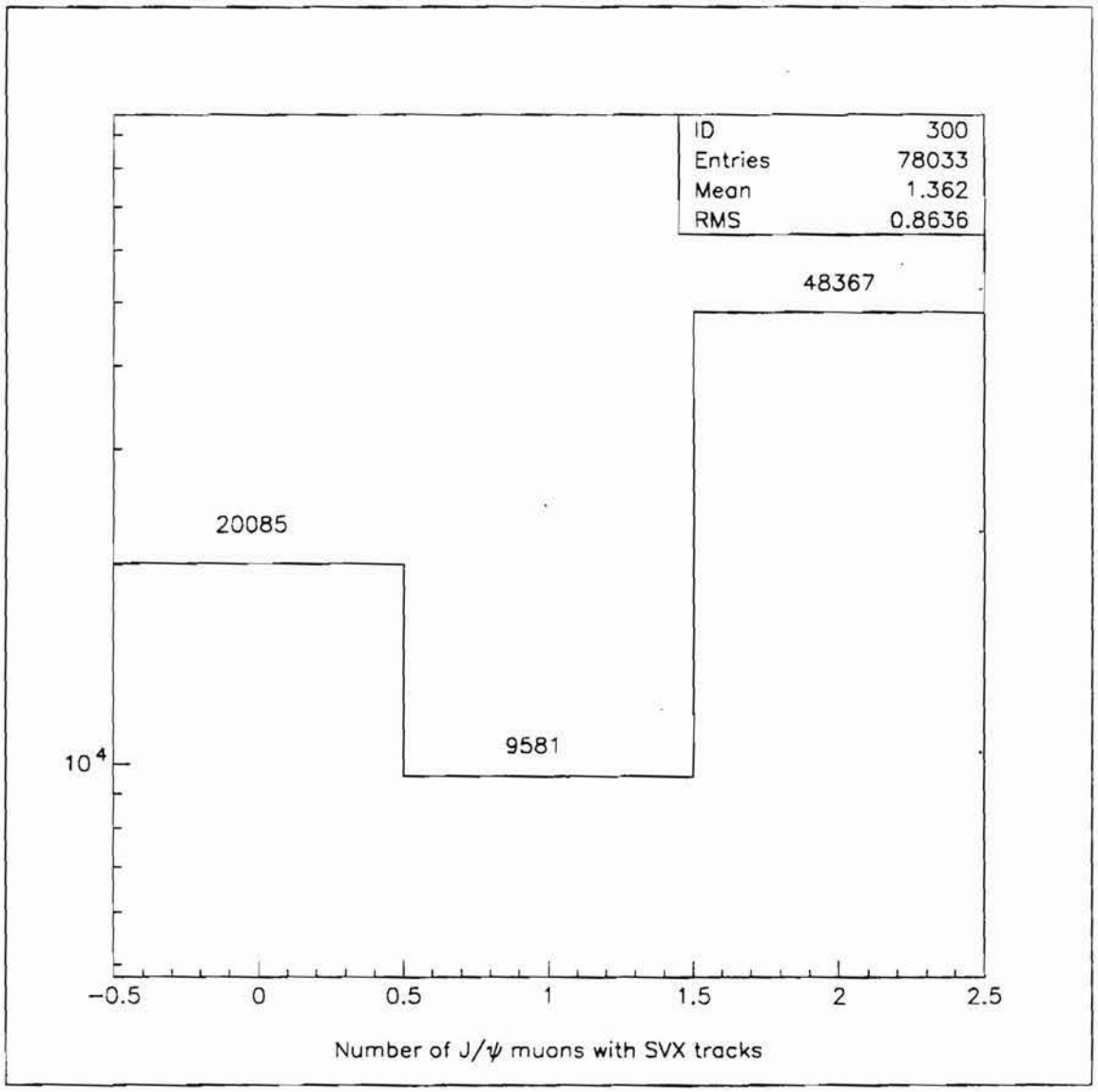

Figure 5.20

Number of muons per pair forming a J/ψ candidate for which an SVX track is found.

quantities are recalculated and compared. For example, the J/ψ decay vertex is found using both SVX tracks, then the vertex displacement is calculated when the SVX information for one or both tracks is dropped. The upper plot in figure 5.21 shows the x and y movement of the vertex when just one SVX track is dropped. For the majority of tracks, the recalculated vertex stays within about 100 μm of the original 2-SVX vertex. The lower plot in figure 5.21 shows the vertex movement when both SVX tracks are dropped. In this case, the smearing of the vertex is much greater. A similar comparison made for the three-track $B^{\pm}$ vertex is shown in figure 5.22, which exhibits similar behavior.

Another comparison is made of the momentum that is measured by using SVX or CTC-only information. Figure 5.23 shows the relative momentum change for muons and kaon candidates having SVX tracks when the SVX information is dropped. The distributions are centered at zero, and hence there is no p_T bias depending on whether or not SVX information is used.

The result of these studies indicates that in the case where only one track has SVX information, that information is still worth keeping, and that the efficiency of momentum cuts does not depend on whether or not SVX information is used. So the B candidates is formed with any combination of SVX and CTC-only tracks, and the selection will be applied to quantities which use the best tracking available.

5.3.4 Muon Chamber Tracking Efficiency

The efficiency for finding a muon chamber track segment was studied using a data sample obtained by triggering the CDF detector on cosmic ray muons. Another method used track segments found in the central muon upgrade chambers which were associated with CTC tracks which pass through the active regions of the central muon detector. From these studies, the muon chamber tracking efficiency

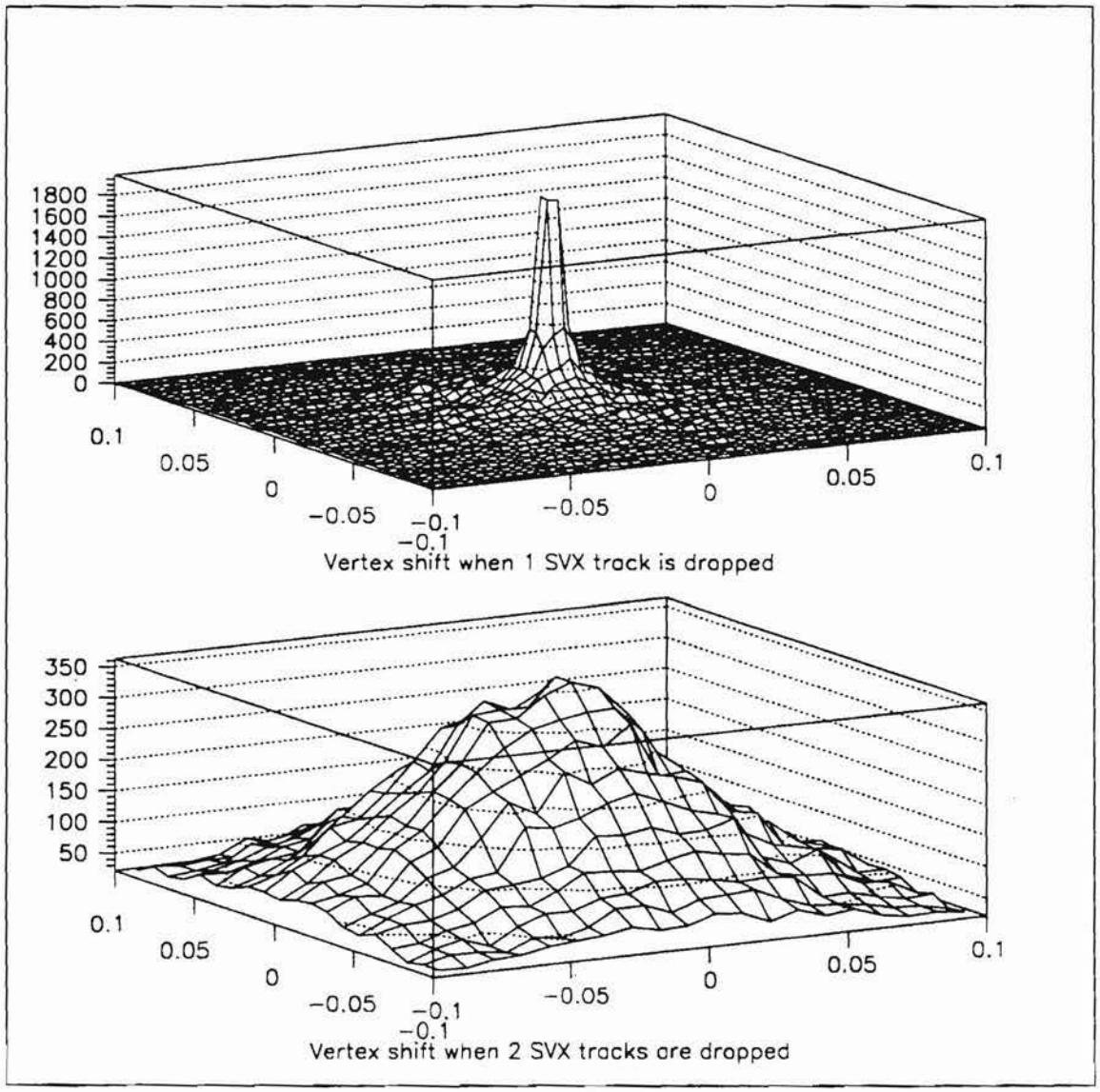

Figure 5.21

Movement of J/ψ vertex when SVX information for one or both muon(s) is dropped.

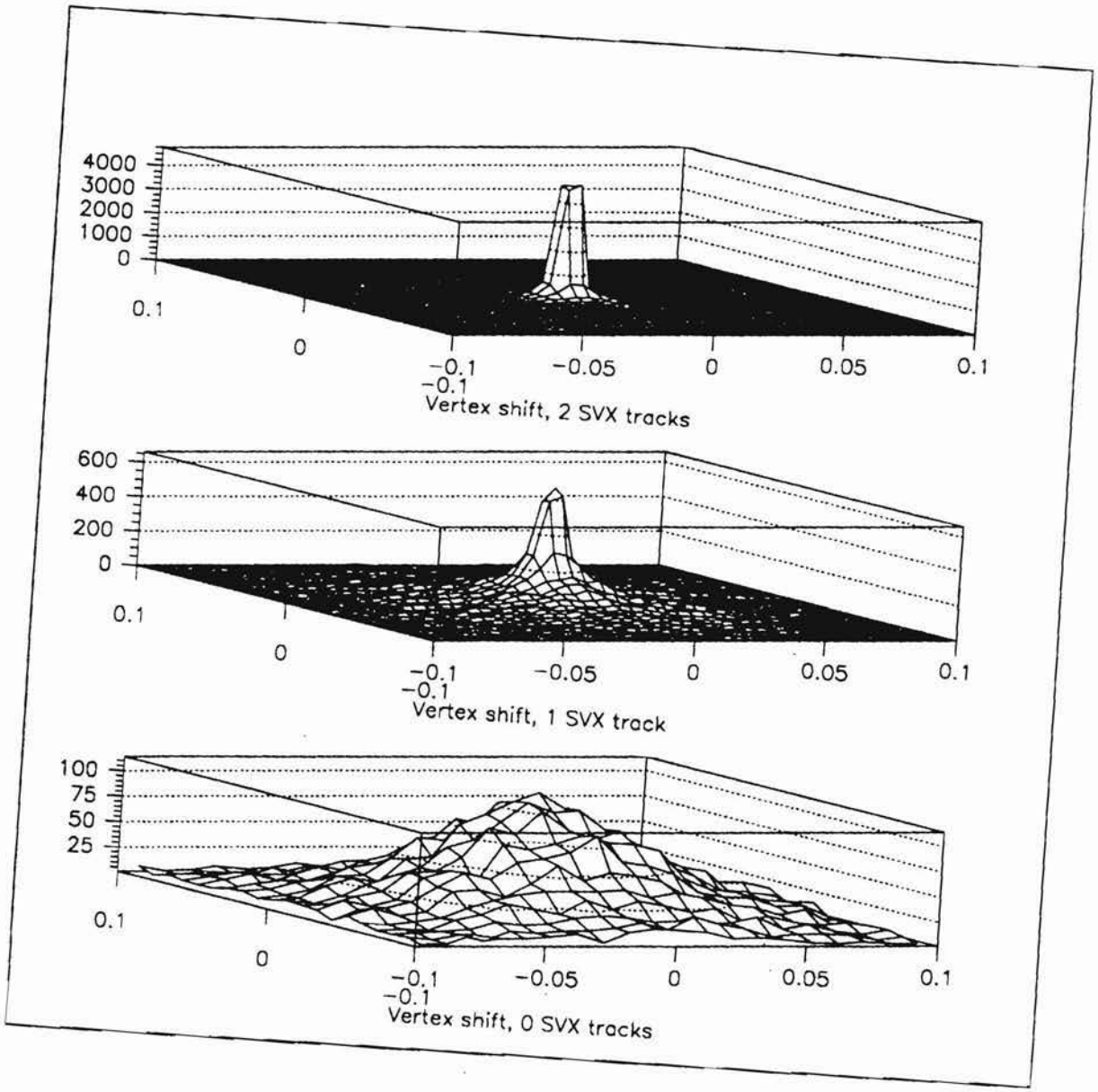

Figure 5.22

Movement of B vertex when SVX information is dropped for one, two, or all three tracks.

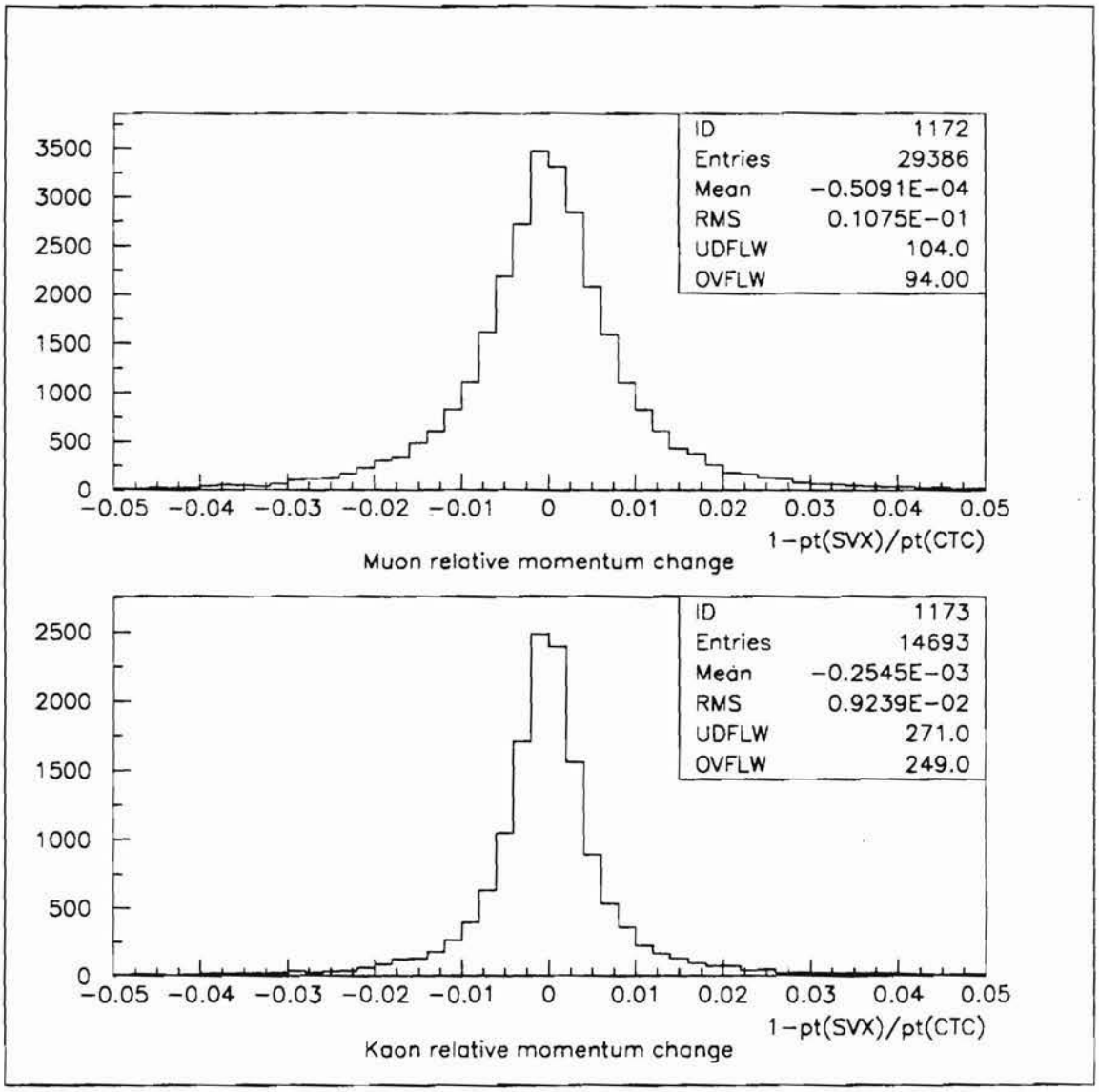

Figure 5.23

Muon and kaon relative transverse momentum change between SVX and CTC tracking.

was determined to be 98±1%. Additional systematic uncertainty is associated with the method of linking a central muon chamber track segment with a CTC track. Some fraction of the time, the wrong CTC track could be linked to a muon track segment, which could result in the J/ψ failing the online level 3 selection requirements. A ±8% contribution to the systematic uncertainty is assigned for this effect [4].

5.4 Summary of the Reconstruction Efficiencies

The reconstruction efficiencies are summarized in table 5.3. For B^- candidates decaying to particles completely contained within the detector acceptance, the reconstruction efficiency is determined to be 86.6 ± 2.7 %. For $\overline{B^0}$ candidates, the reconstruction efficiency is determined to be 85.6 ± 2.8%. In table 5.4 is a summary of the systematic uncertainties, which total 20.9 % for the $B^\pm \to J/\psi K^\pm$ decay and 28.9 % for the $B^0 \to J/\psi K^{*0}$ decay. The largest contribution to the systematic uncertainty comes from the uncertainty in the branching ratios.

Table 5.3

Summary of reconstruction efficiencies for B meson reconstructed using the $B^{\pm} \rightarrow J/\psi K^{\pm}$ and $B^0 \rightarrow J/\psi K^{*0}$ decay channels.

Source	Efficiency	
	$B^{\pm} \rightarrow J/\psi K^{\pm}$	$B^0 \rightarrow J/\psi K^{*0}$
L3 $\mu^+\mu^-$ Tracking efficiency	93.1 ± 2%	93.1 ± 2%
CTC tracking efficiency	98.9 ± 1%	97.8 ± 1.4 %
Muon chamber efficiency	98.0 ± 1%	98.0 ± 1 %
Muon matching cut efficiency	98.7 ± 1%	98.7 ± 1%
B vertex χ^2 cut efficiency	98.6 ± 1 %	98.6 ± 1%
J/ψ vertex χ^2 cut efficiency	98.6 ± 1 %	98.6 ± 1%
Total	86.6 ± 2.7 %	85.6 ± 2.8 %

Table 5.4

Summary of systematic uncertainties in the cross-section measured using the $B^{\pm} \rightarrow J/\psi K^{\pm}$ and $B^0 \rightarrow J/\psi K^{*0}$ decay channels.

Source	Uncertainty	
	$B^{\pm} \rightarrow J/\psi K^{\pm}$	$B^0 \rightarrow J/\psi K^{*0}$
Total reconstruction efficiency	3.1%	3.3 %
$c\tau$ cut efficiency	4%	4%
CTC-muon track association	8%	8%
Trigger efficiency	4%	4%
Structure functions	5%	5%
Fragmentation	7%	7%
J/ψ polarization	—	7%
Kaon decays in flight	4%	4%
Luminosity	4%	4%
Branching ratio	15%	24%
Total	20.9%	28.9%

6. CROSS-SECTION CALCULATION

Now that the process of identifying B mesons and the procedure for determining the reconstruction efficiencies and detector acceptance has been presented, this final chapter presents the cross-section calculations and results.

6.1 Total Cross-section

The B meson integrated cross-section is calculated by the following equation:

$$\sigma = \frac{N/2}{\mathcal{L} \cdot A \cdot \epsilon \cdot Br},$$

N is the number of events observed, determined by fitting the invariant mass distributions. The factor of 1/2 is included because decays of both B and $\overline{B}$ mesons have been reconstructed, but the theoretical cross-section to which the result will be compared is calculated for mesons containing b quarks only. $\mathcal{L}$ is the integrated luminosity of $19.4 \pm 0.8\ pb^{-1}$. A is the combined detector acceptance and reconstruction efficiency that is determined from the Monte Carlo simulation, which is dependent on the B meson momentum. ϵ is the correction for all other efficiencies not accounted for in the simulation, such as the tracking efficiencies. For the $B^{\pm}$ decay, $\epsilon = 0.866 \pm 0.074$, while for the B^0 decay, $\epsilon = 0.856 \pm 0.073$. Br is the combined branching fraction. The branching fraction for the $B^{\pm} \rightarrow J/\psi K^{\pm}$ decay was determined by CLEO [25] to be $(1.12 \pm 0.17) \times 10^{-3}$ and for the $B^0 \rightarrow J/\psi K^{*0}$ decay to be $(1.53 \pm 0.37) \times 10^{-3}$. The branching fraction for $J/\psi \rightarrow \mu^+\mu^-$ is $(5.97 \pm 0.25)\%$ [28], and for $K^{*0} \rightarrow K^+\pi^-$ is 2/3, from isospin. This results in a combined branching fraction of $(6.68 \pm 1.05) \times 10^{-5}$ for the charged B meson

decay mode and $(6.09 \pm 1.49) \times 10^{-5}$ for the neutral B meson decay mode. The integrated cross-section can be calculated for any value of p_{Tmin} by fitting the mass distribution of the subset of reconstructed B candidates which have $p_T > p_{Tmin}$. In addition to the mass distributions shown in chapter 4 for $p_T(B) > 6.0$ GeV/c, figures 6.1-6.5 show the $B^{\pm}$ mass distribution for $p_T(B)$ >9.0, 12.0, and 15.0 GeV/c, and the B^0 mass distribution for $p_T(B)$ >9.0 and 12.0 GeV/c. Tables 6.1 and 6.2 summarize the integrated cross-sections for each of these values of p_{Tmin} for the $B^{\pm} \rightarrow J/\psi K^{\pm}$ and $B^0 \rightarrow J/\psi K^{*0}$ decays, respectively. The integrated cross-sections for the two channels are equal within the errors for each value of p_{Tmin}, as expected from a model in which a produced b quark is equally likely to combine with a $\overline{u}$ or $\overline{d}$ quark.

Table 6.1

B^- meson integrated cross-sections, for selected values of p_{Tmin}.

p_{Tmin} (GeV/c)	Events	Acceptance (%)	$\sigma(p_T \geq p_{Tmin}, \lvert y \rvert < 1.0)$ (μb)
6.0	122 ± 16	2.64 ± 0.02	$2.06 \pm 0.27 \pm 0.43$
9.0	74 ± 11	5.26 ± 0.05	$0.627 \pm 0.092 \pm 0.131$
12.0	44 ± 8	7.23 ± 0.07	$0.271 \pm 0.048 \pm 0.057$
15.0	24 ± 6	9.03 ± 0.08	$0.118 \pm 0.029 \pm 0.025$

The b quark integrated cross-section can be obtained using the same equation, but the value of p_{Tmin} is not directly measured. It is conventional [4, 5] to use a

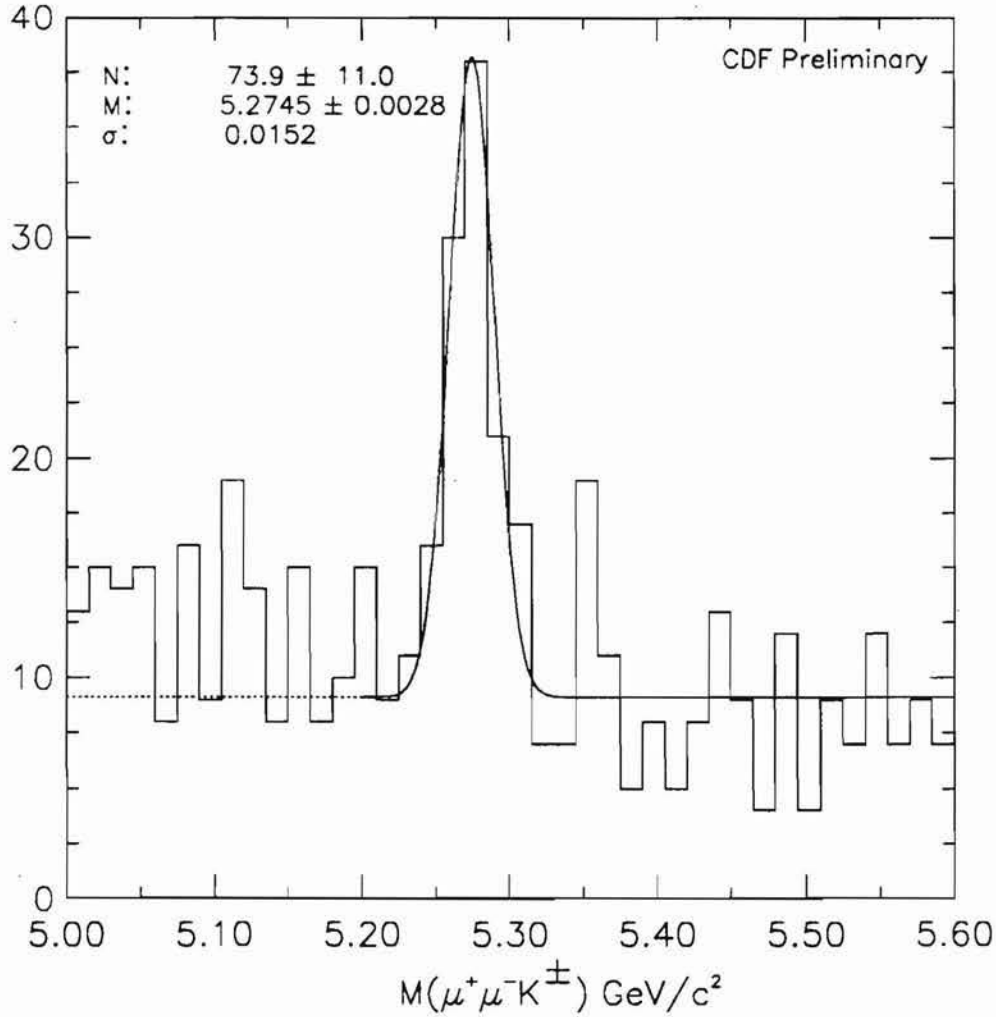

Figure 6.1

$B^{\pm}$ invariant mass distribution for $p_T(B^{\pm}) \geq 9.0$ GeV/c and the results of the fit.

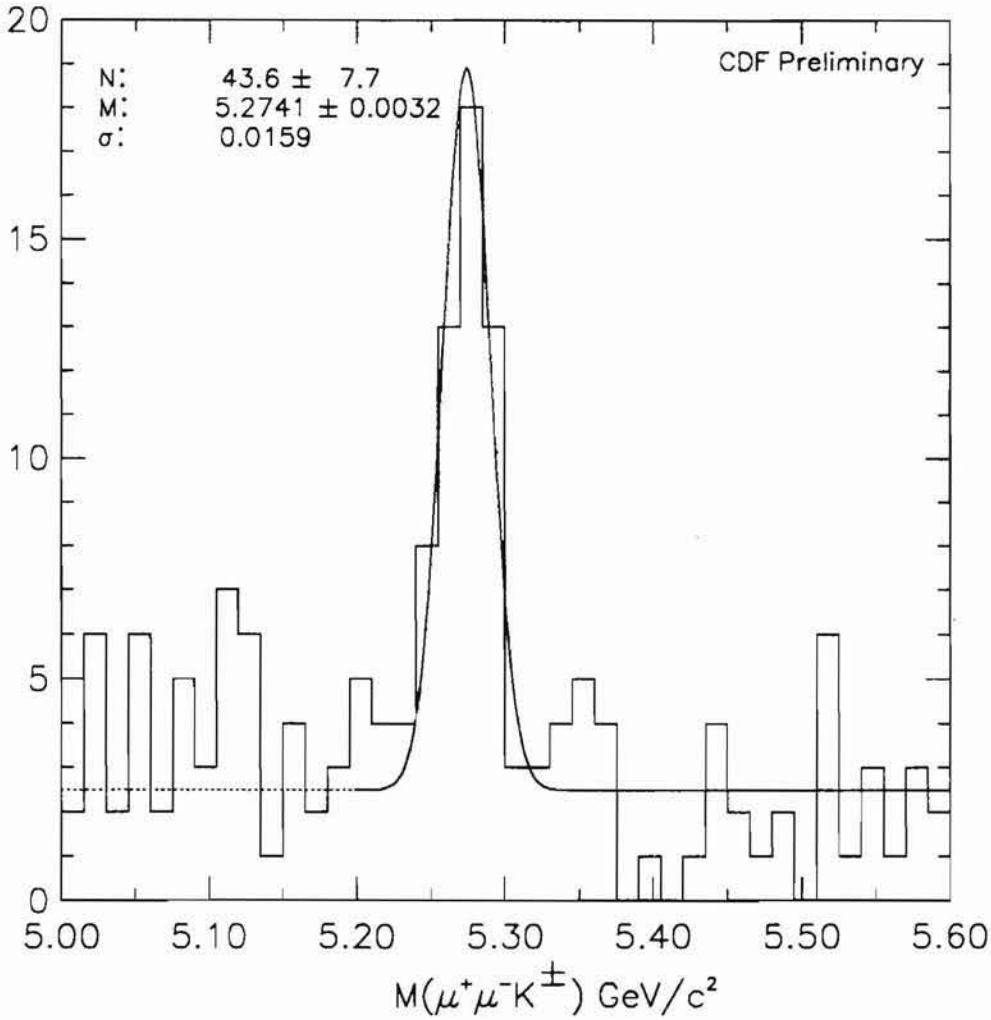

Figure 6.2

$B^{\pm}$ invariant mass distribution for $p_T(B^{\pm}) \geq 12.0$ GeV/c and the results of the fit.

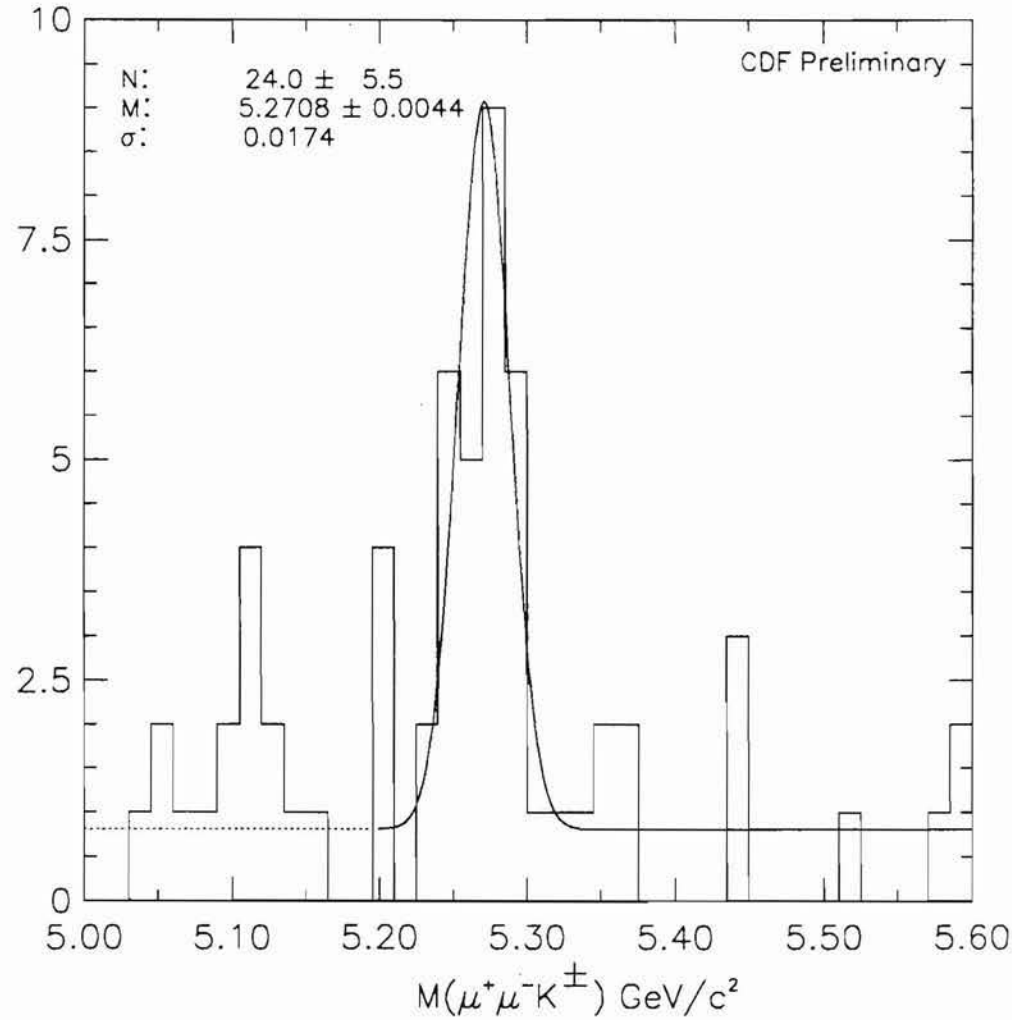

Figure 6.3

$B^{\pm}$ invariant mass distribution for $p_T(B^{\pm}) \geq 15.0$ GeV/c and the results of the fit.

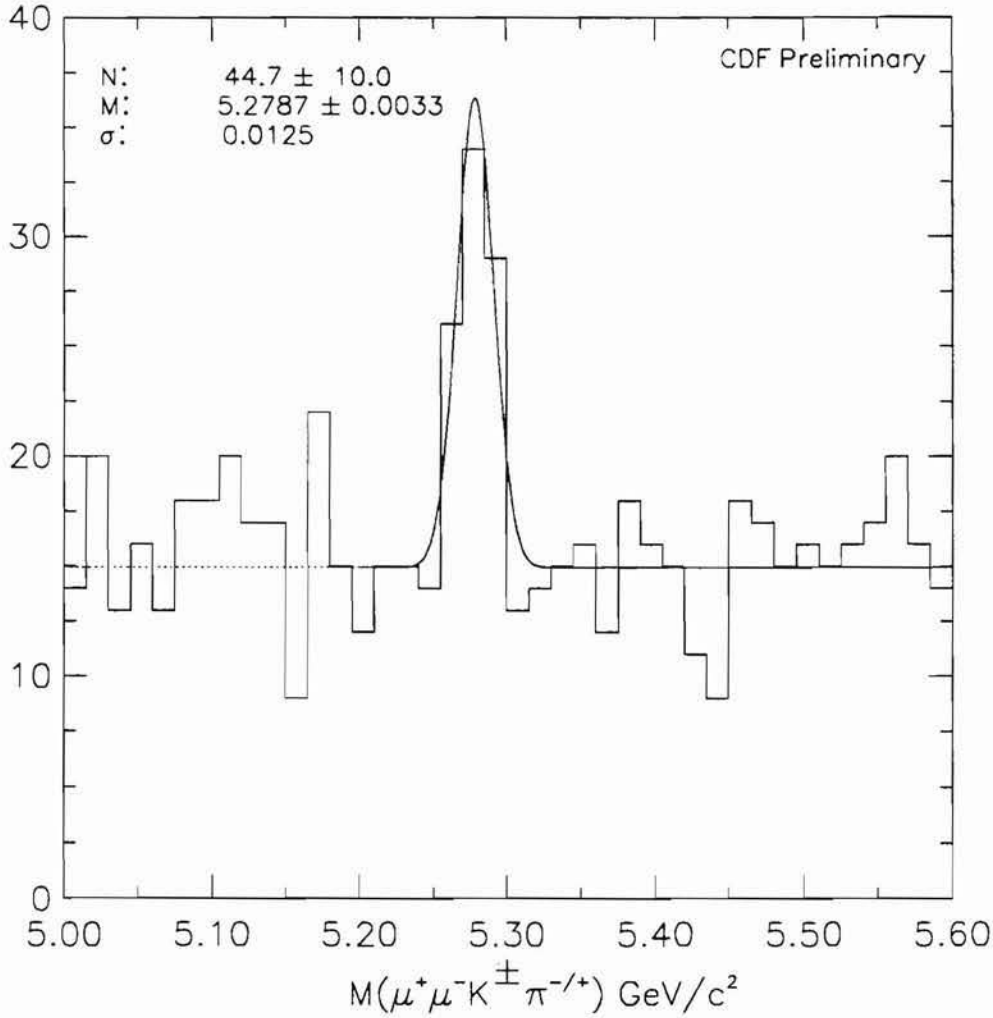

Figure 6.4

B^0 invariant mass distribution for $p_T(B^0) \geq 9.0$ GeV/c and the results of the fit.

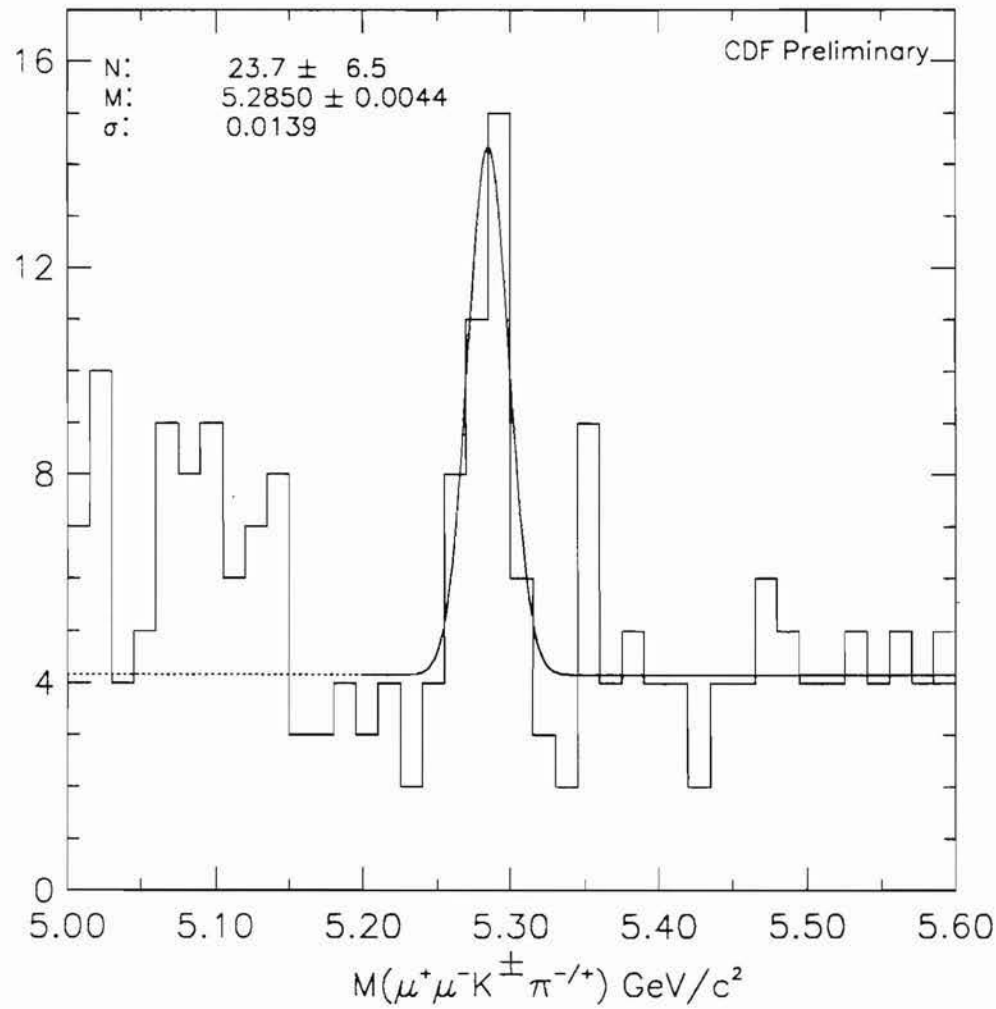

Figure 6.5

B^0 invariant mass distribution for $p_T(B^0) \geq 12.0$ GeV/c and the results of the fit.

Table 6.2

$\overline{B^0}$ meson integrated cross-sections, for selected values of p_{Tmin}.

p_{Tmin} (GeV/c)	Events	Acceptance (%)	$\sigma(p_T \geq p_{T_{min}}, \lvert y \rvert < 1.0)$ (μb)
6.0	75 ± 15	1.67 ± 0.01	$2.22 \pm 0.44 \pm 0.64$
9.0	45 ± 10	3.62 ± 0.03	$0.615 \pm 0.14 \pm 0.17$
12.0	24 ± 7	4.82 ± 0.04	$0.246 \pm 0.075 \pm 0.071$

value of $p_{Tmin}(b)$ (p_T for the b quark) such that 90% of the B mesons in the sample come from b quarks with $p_T(B) > p_{Tmin}(b)$. The Monte Carlo simulation was used to determine the values of p_{Tmin} for each of the B meson samples that were used for the B meson integrated cross-sections. The correspondence between $p_{Tmin}(b)$ and $p_{Tmin}(B)$ is shown is table 6.3. In addition, the combined branching fraction

Table 6.3

Correspondence between $p_{Tmin}(b)$ for the b quark and $p_{Tmin}(B)$ for the B meson.

$p_{Tmin}(b)(GeV/c)$	$p_{Tmin}(B)(GeV/c)$
7.5	6.0
10.5	9.0
13.5	12.0
16.5	15.0

Table 6.4

b quark integrated cross-sections using the $B^{\pm} \rightarrow J/\psi K^{\pm}$ decay channel, for selected values of p_{Tmin}.

p_{Tmin} (GeV/c)	Events	Acceptance (%)	$\sigma(p_T \geq p_{Tmin}, \lvert y \rvert < 1.0)$ (μb)
7.5	122 ± 16	2.45 ± 0.02	$5.92 \pm 0.78 \pm 1.24$
10.5	74 ± 11	4.42 ± 0.03	$1.99 \pm 0.30 \pm 0.41$
13.5	44 ± 8	5.66 ± 0.04	$0.924 \pm 0.17 \pm 0.20$
16.5	24 ± 6	6.37 ± 0.04	$0.447 \pm 0.11 \pm 0.10$

also includes the fraction of b quarks that fragment to B^- and $\overline{B^0}$ mesons. For this part of the branching fraction, the standard assumption made [29] is that b quarks fragment to B^- and $\overline{B^0}$ mesons with equal probability, which is confirmed in our data, and that the two mesons account for 75% of all b hadrons produced. The b quark integrated cross-sections are summarized in tables 6.4 and 6.5. Again, the integrated cross-sections measured using either decay channel are very consistent with one another.

The integrated b quark cross-section measurements are the data points in figure 6.6, where they are compared to QCD next-to-leading order predictions. As was noted in chapter 2, the absolute value of the QCD calculation for the b quark cross section is subject to uncertainty in the renormalization scale, μ; while the p_T dependence of the calculated cross-section is much less sensitive to μ. The solid curve in figure 6.6 corresponds to the use of the natural scale μ_0 and $\lambda_4 = 230$ Mev. The shape is in good agreement with the data but underestimates the magnitude.

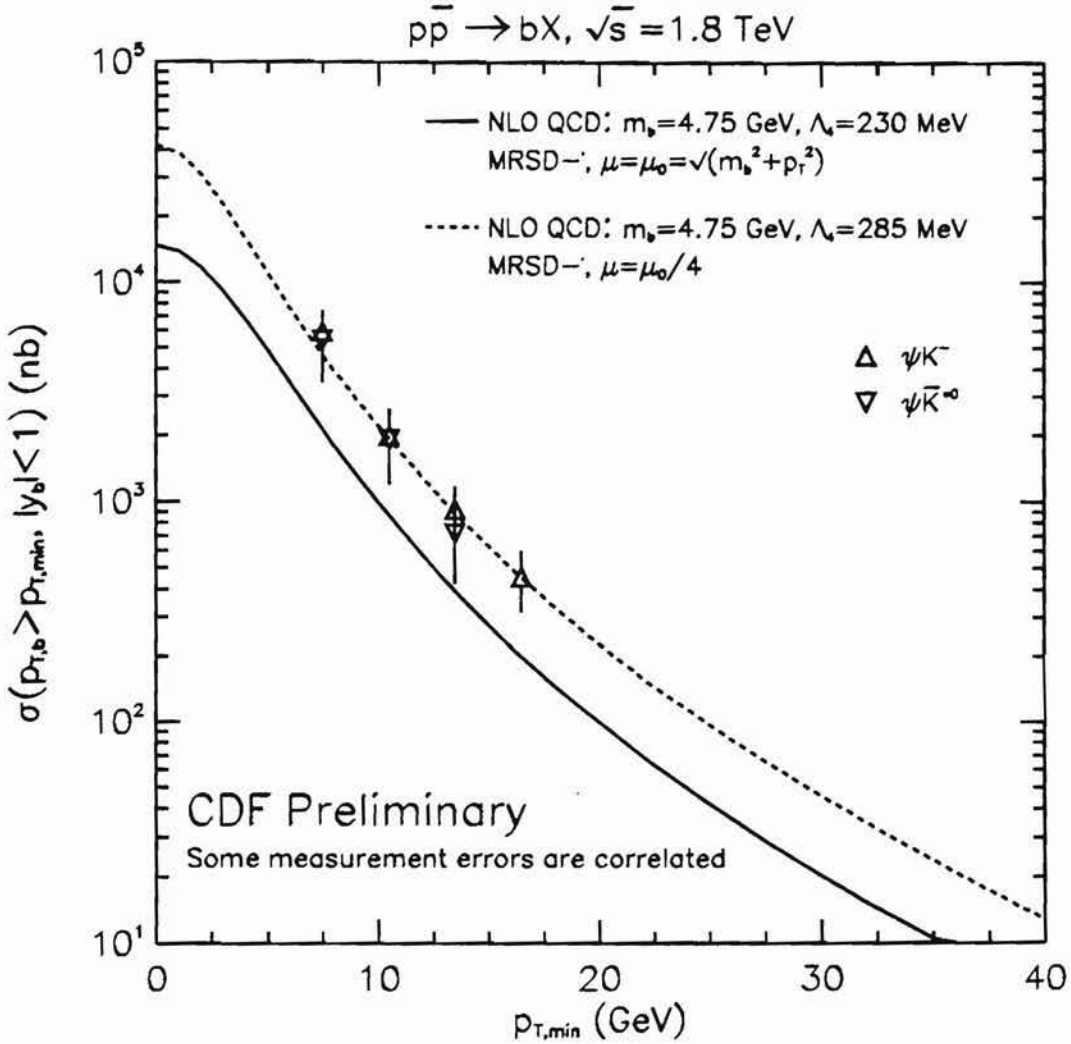

Figure 6.6

b quark integrated cross-section measurements, compared to the next-to-leading order QCD prediction.

Table 6.5

b quark integrated cross-sections using the $B^0 \rightarrow J/\psi K^{*0}$ decay channel, for selected values of p_{Tmin}.

p_{Tmin} (GeV/c)	Events	Acceptance (%)	$\sigma(p_T \geq p_{T_{min}}, \lvert y \rvert < 1.0)$ (μb)
7.5	75 ± 15	1.79 ± 0.01	$5.52 \pm 1.10 \pm 1.60$
10.5	45 ± 10	3.02 ± 0.02	$1.96 \pm 0.45 \pm 0.56$
13.5	24 ± 7	4.23 ± 0.03	$0.748 \pm 0.23 \pm 0.22$

However, it is possible to get excellent agreement both in shape and magnitude by using a scale of $\mu_0/4$ and $\lambda_4 = 285$ MeV.

6.2 Differential Cross-section

Since one expects QCD to do a good job of predicting the p_T distribution, the most sensitive test of QCD can be made by measuring the B meson differential cross-section in p_T. This is more direct than the analysis above, where the process of converting between the directly measured B meson p_T and the b quark p_T depends substantially on the use of Monte Carlo. To measure the B meson differential cross-section as a function of p_T, the B meson candidates are divided into subsets according to p_T. For the measurement using the $B^{\pm} \rightarrow J/\psi K^{\pm}$ decay, the invariant mass distribution is fitted for mesons with p_T in the ranges 6-9 GeV/c, 9-12 GeV/c, and 12-15 GeV/c. For the $B^0 \rightarrow J/\psi K^{*0}$ decay, the ranges are 7-11 GeV/c and 11-15 GeV/c. The p_T ranges were chosen so as to divide the data into distributions with comparable signal-to-noise. Figures 6.7-6.11 show the mass distributions for each of these p_T ranges.

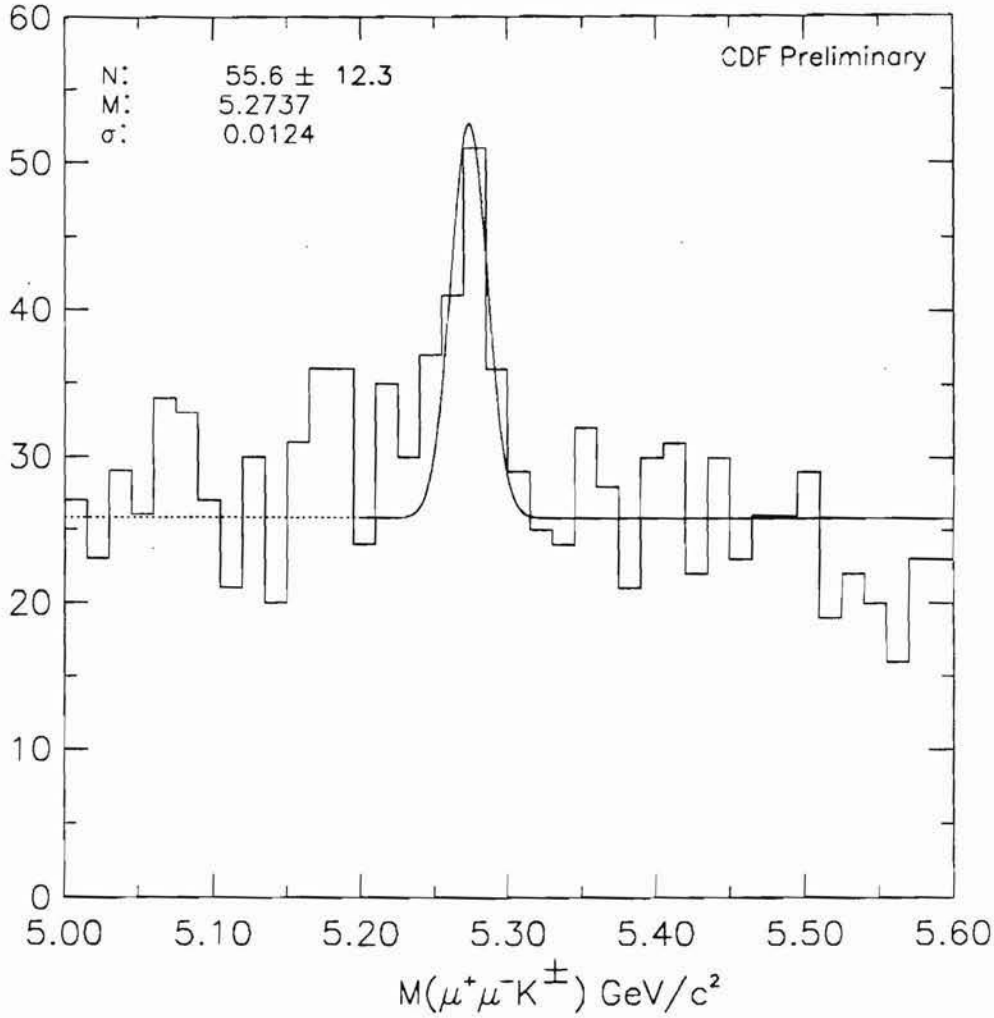

Figure 6.7

$B^{\pm}$ invariant mass distribution for $6.0 < p_T(B^{\pm}) < 9.0$ GeV/c and the results of the fit.

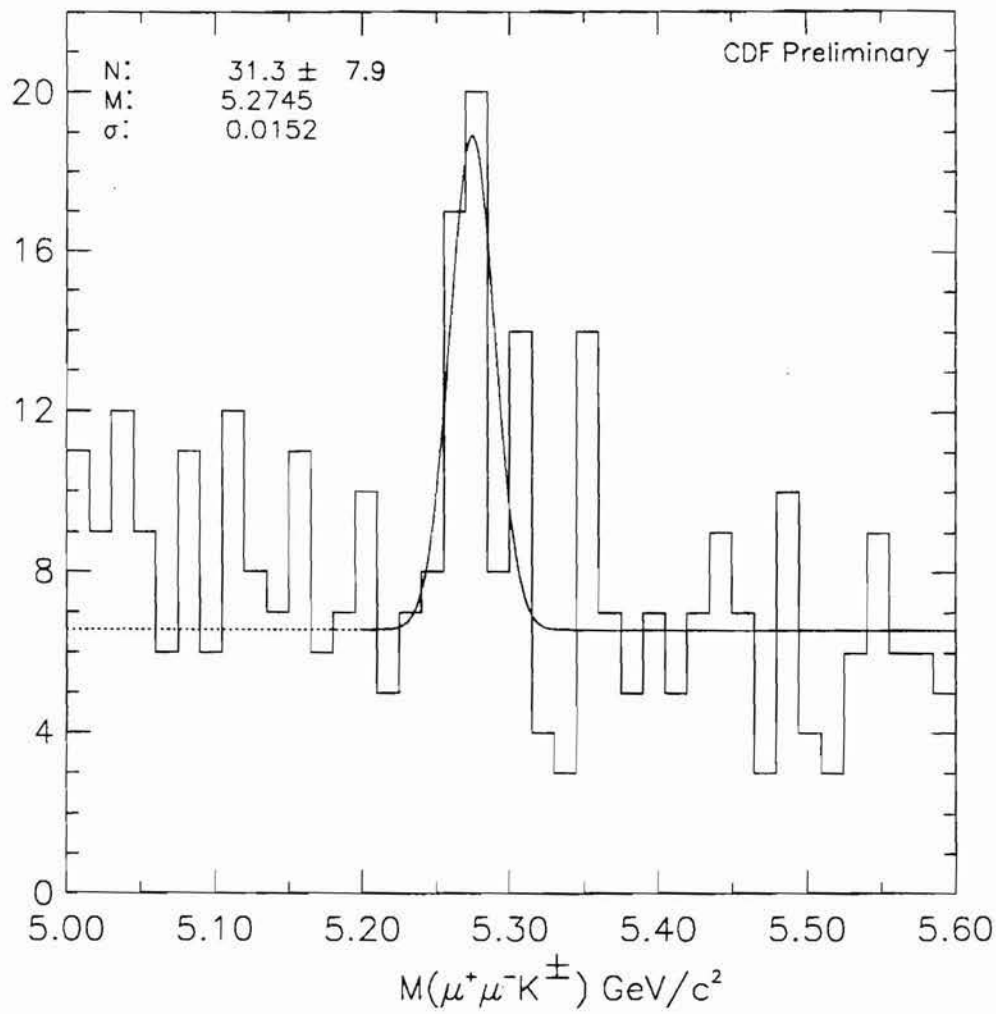

Figure 6.8

$B^{\pm}$ invariant mass distribution for $9.0 < p_T(B^{\pm}) < 12.0$ GeV/c and the results of the fit.

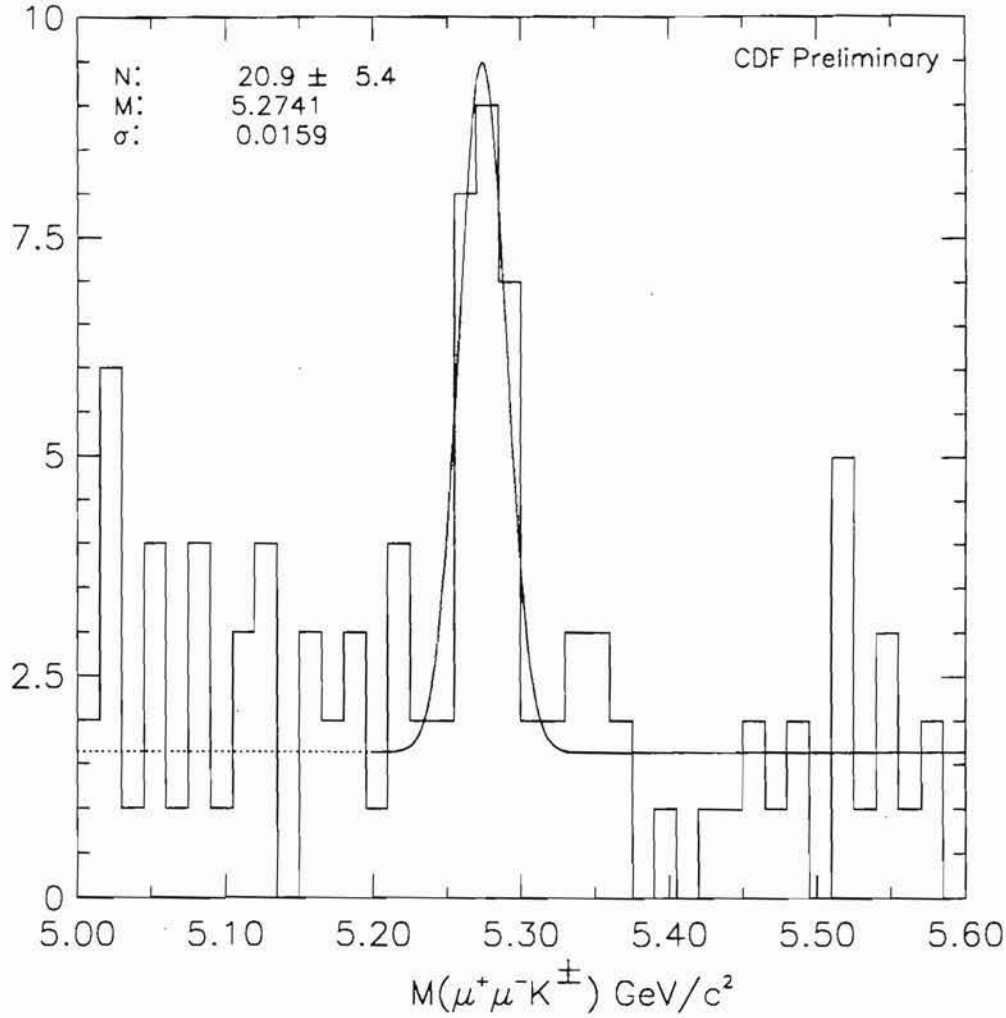

Figure 6.9

$B^{\pm}$ invariant mass distribution for $12.0 < p_T(B^{\pm}) < 15.0$ GeV/c and the results of the fit.

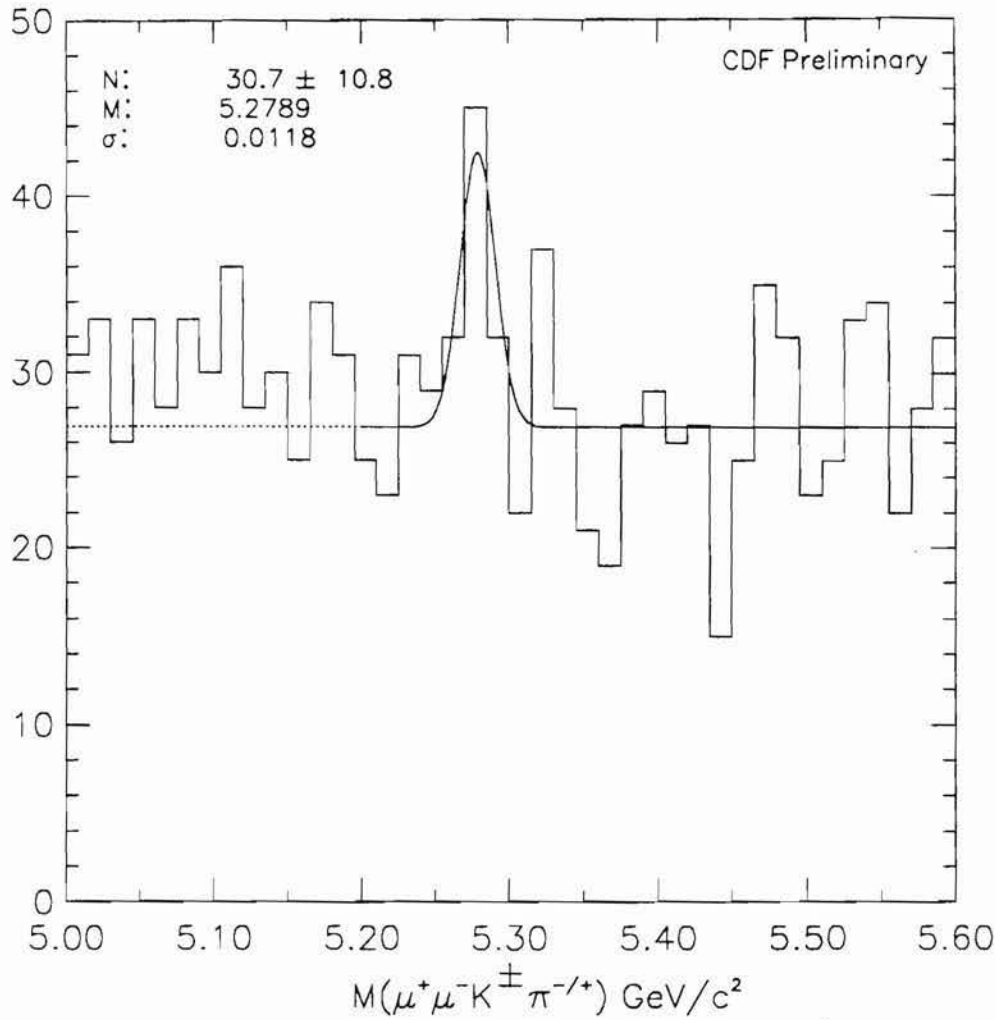

Figure 6.10

B^0 invariant mass distribution for $7.0 < p_T(B^0) < 11.0$ GeV/c and the results of the fit.

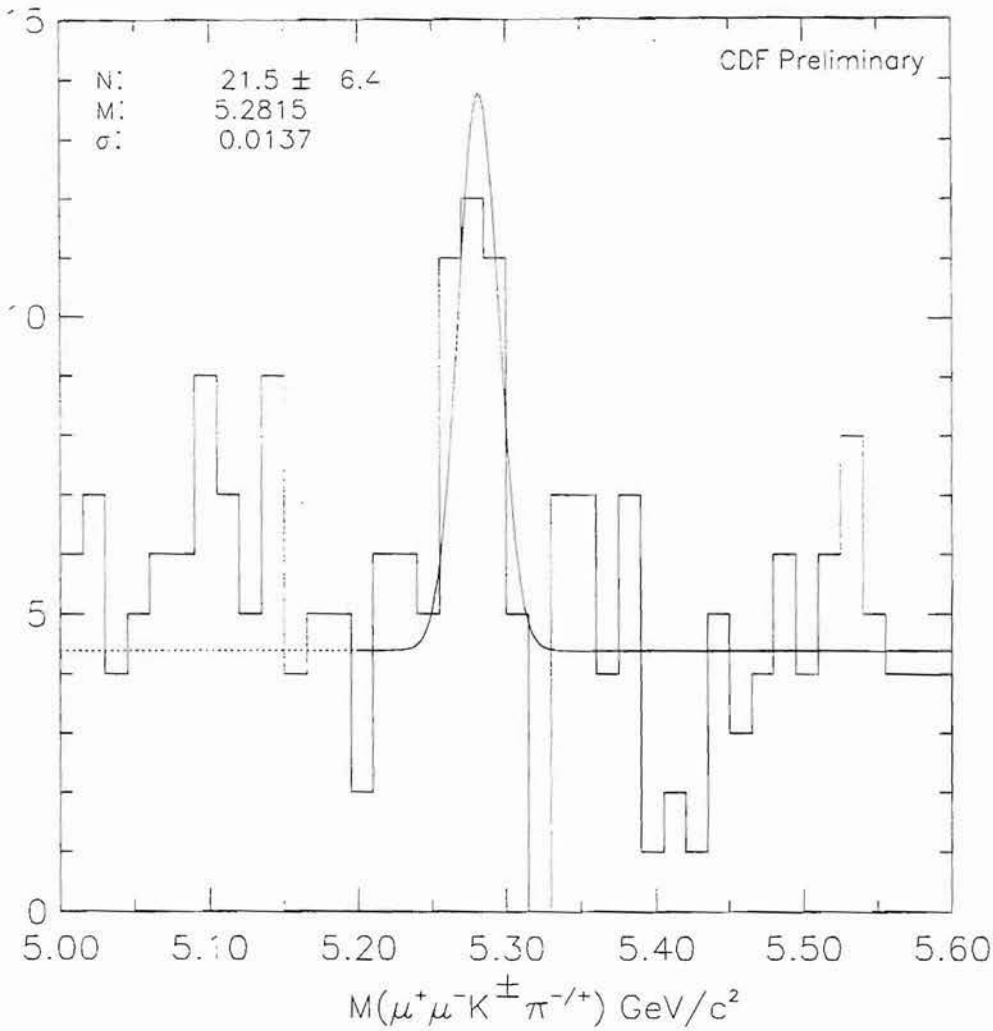

Figure 6.11

B^0 invariant mass distribution for $11.0 < p_T(B^0) < 15.0$ GeV/c and the results of the fit.

Table 6.6

Mean B meson p_T for the five transverse momentum ranges used to determine the differential cross-section

p_T range (GeV/c)	mean p_T (GeV/c)
6-9	7.4
9-12	10.4
12-15	13.4
7-11	8.8
11-15	12.8

The differential cross-section is determined from an equation similar to that used for the integrated cross-section:

$$\frac{d\sigma}{dp_T} = \frac{N/2}{\Delta_{p_T} \cdot \mathcal{L} \cdot A \cdot \epsilon \cdot Br},$$

where Δ_{p_T} is the width of the p_T bin, which is 3 GeV/c for the $B^{\pm}$ mesons and 4 GeV/c for the B^0 mesons. The value of p_T at which the cross-section is quoted is determined by calculating the mean p_T in each of the ranges. Specifically, the p_T distribution for all B candidates within a 60-MeV/c^2 window about the average B mass of 5.279 GeV/c^2 is fit to an exponential, and the result of the fit is used to compute the mean p_T of each range analytically. Table 6.6 shows the mean p_T for each of the p_T ranges. Tables 6.7 and 6.8 summarize the B^- and $\overline{B^0}$ differential cross-section measurements.

Another advantage in measuring $d\sigma(B)/dp_T$ is that the systematic uncertainties for each of the measured points are correlated, so that the shape of the distribution is better determined than is the absolute value of any one of the points taken

Table 6.7

B^- meson differential cross-sections using the $B^\pm \to J/\psi K^\pm$ decay channel.

mean p_T (GeV/c)	Events	Acceptance (%)	$\sigma(p_T \geq p_{T_{min}}, \lvert y\rvert < 1.0)$ (μb)
7.4	56 ± 12	1.29 ± 0.01	$0.644 \pm 0.14 \pm 0.14$
10.4	31 ± 8	3.58 ± 0.04	$0.129 \pm 0.032 \pm 0.027$
13.4	21 ± 5	5.71 ± 0.07	$0.0546 \pm 0.013 \pm 0.011$

Table 6.8

$\overline{B^0}$ meson differential cross-sections using the $\overline{B^0} \to J/\psi \overline{K^{*0}}$ decay channel.

mean p_T (GeV/c)	Events	Acceptance (%)	$\sigma(p_T \geq p_{T_{min}}, \lvert y\rvert < 1.0)$ (μb)
8.8	31 ± 11	1.18 ± 0.01	$0.324 \pm 0.12 \pm 0.094$
12.8	22 ± 6	3.46 ± 0.04	$0.0786 \pm 0.022 \pm 0.023$

separately. In figure 6.12, the differential cross-section for the B^- meson is shown as the filled circles, while the differential cross-section for the $\overline{B^0}$ meson is shown as the crosses. The common systematic uncertainty of 21% for the B^- points and 29% for the $\overline{B^0}$ points has been removed from the error bars. Also shown are Monte Carlo predictions, which employ the next-to-leading order QCD calculation and the fragmentation model that has been described in previous chapters. The data points for both types of B meson are in good agreement with one another.

The QCD calculation using the natural scale factor μ_0 has approximately the right shape but fails to predict the correct magnitude. However, by going to a scale of $\mu_0/4$ and varying λ_4 from 230 to 285 MeV, both the shape and magnitude are correctly predicted with the possible exception of the lowest p_T bin.

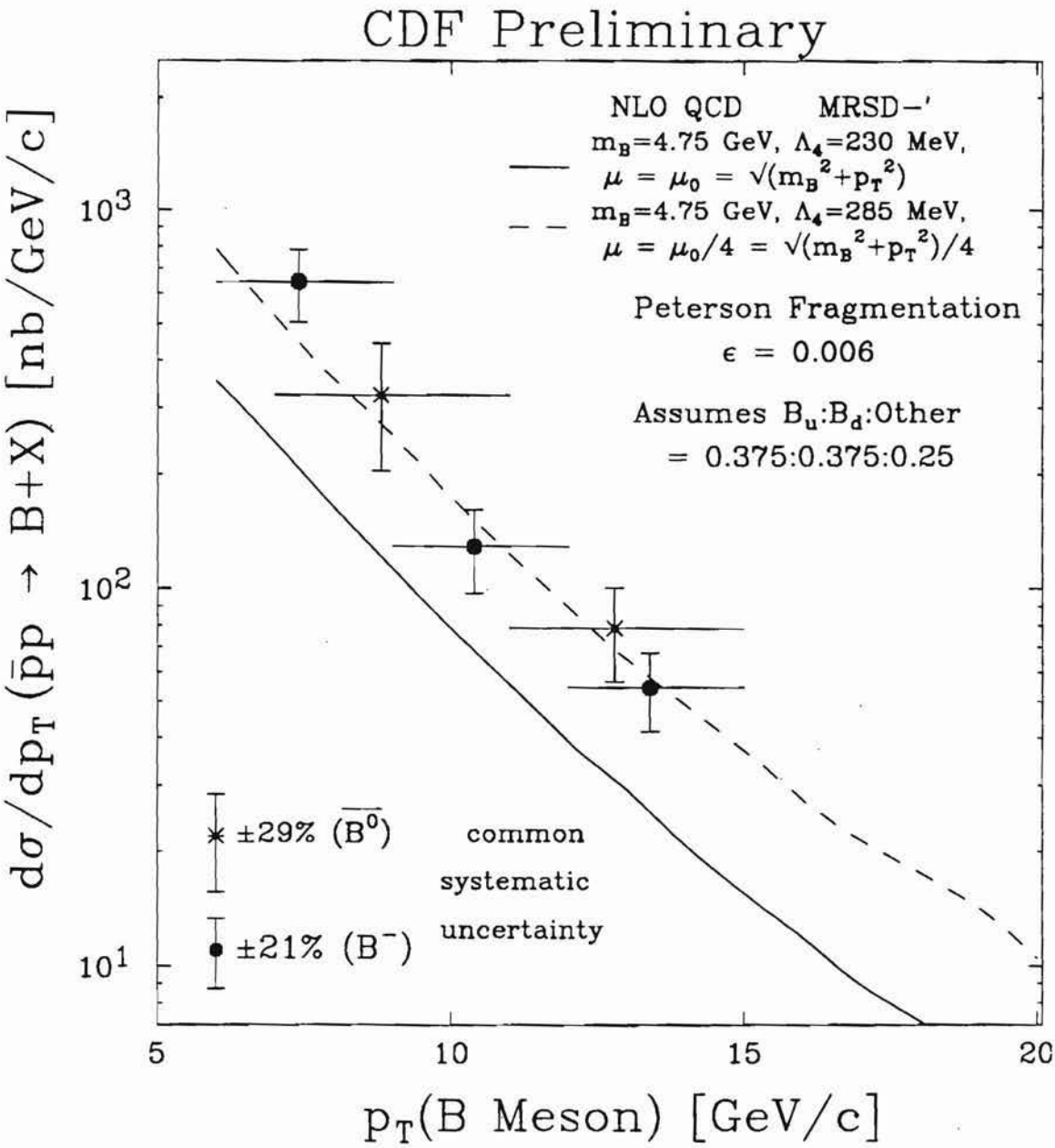

Figure 6.12

B meson differential cross-section measurements, compared to the theoretical prediction.

BIBLIOGRAPHY

BIBLIOGRAPHY

1. P. Nason, S. Dawson, and R.K. Ellis. The total cross-section for the production of heavy quarks in hadronic collisions. *Nucl. Phys*, B303:607–633, 1988.

2. M. Mangano, P. Nason, and G. Ridolfi. Heavy-quark correlations in hadron collisions at next-to-leading order. *Nucl. Phys.*, B373:295–345, 1992.

3. A.D. Martin, W.J. Stirling, and R.G. Roberts. New information on parton distributions. *Phys. Rev. D*, 47:867–882, 1993.

4. F. Abe et al. (The CDF Collaboration). A measurement of the B meson and b quark cross-sections at $\sqrt{s} = 1.8$ TeV using the exclusive decay $B^{\pm} \rightarrow J/\psi K^{\pm}$. *Phys. Rev. Lett.*, 68:3403–3407, January 1992.

5. F. Abe et al. (The CDF Collaboration). Measurement of the bottom quark cross-sections in $p - \overline{p}$ collisions at $\sqrt{s} = 1.8$ TeV using the exclusive decay $B^0 \rightarrow J/\psi K^{*0}$. Technical Report FERMILAB-CONF-92-361-E, Fermilab, November 1992. Submitted to Phys. Rev. D.

6. G. Altarelli and G. Parisi. Asymptotic freedom in parton language. *Nucl. Phys.*, B126:298–318, 1977.

7. R. Brugnera. x_g determination using J/ψ inelastic events. In W. Buchmülee and G. Ingleman, editors, *Physics at HERA, Proceedings of the 1991 Workshop*, pages 557–562, 1991.

8. R. van Woudenberg et al. Gluon density determination from open charm events at HERA. In W. Buchmülee and G. Ingleman, editors, *Physics at HERA, Proceedings of the 1991 Workshop*, pages 739–769, 1991.

9. M. Arneodo et al. (New Muon Collaboration). Quark and gluon distributions and α_s from nucleon structure functions at low x. *Phys. Lett. B*, 309:222–230, 1993.

10. J. Alitti et al. (UA2 Collaboration). Measurement of the gluon structure function from direct photon data at the CERN $\overline{p} - p$ collider. *Phys. Lett. B*, 299:174–182, 1993.

11. A.D. Martin, W.J. Stirling, and R.G. Roberts. Parton distributions updated. *Phys. Lett. B*, 306:145–150, 1993.

12. A.D. Martin, W.J. Stirling, and R.G. Roberts. MRS parton distributions. Technical Report RAL-93-077, Rutherford, October 1993.

13. F. Abe et al. (The CDF Collaboration). Probing the gluon distribution with the SS-OS dijet cross-section ratio. Technical Report FERMILAB-CONF-93-203-E, Fermilab, August 1993. Submitted to 16th International Symposium on Lepton and Photon Interactions, Ithaca, NY, 10-15 Aug 1993.

14. C. Peterson, D. Schlatter, I. Schmitt, and P.M. Zerwas. Scaling violations in inclusive e^+e^- annihilation spectra. *Phys. Rev. D*, 27(1):105–111, 1983.

15. J. Chrin. Upon the determination of heavy quark fragmentation functions in e^+e^- annihilation. *Phys. Rev. Lett.*, 67:2418–2422, July 1991.

16. F. Abe et al. (The CDF Collaboration). The cdf detector: An overview. *Nucl. Instrum. Meth. Phys. Res.*, A271:387–403, 1988.

17. K. Byrum et al. The cdf forward muon system. *Nucl. Instrum. Meth. Phys. Res.*, A268:46–49, 1988.

18. F. Abe et al. (The CDF Collaboration). The Silicon Vertex Detector of the Collider Detector at Fermilab. Technical Report 2398, CDF, February 1994.

19. H. Wenzel. Tracking in the svx. Technical report, CDF, August 1992.

20. P. Derwent. Changes to the svx tracking package. Technical Report 2188, CDF, August 1993.

21. F. Abe et al. (The CDF Collaboration). Measurement of the $\overline{p} - p$ total cross-section at $\sqrt{s} = 546$ gev and 1800 gev. Technical Report FERMILAB-PUB-93-234-E, Fermilab, August 1993. Submitted to Phys. Rev. D.

22. P. Derwent, C. Grosso-Pilcher, and S. Belforte. σ(BBC) derivation, results, and proposal for new normalization. Technical Report 2361, CDF, March 1994.

23. F. Abe et al. (The CDF Collaboration). Measurement of the B^+ and B^0 lifetimes. Technical Report FERMILAB-PUB-94-034-E, Fermilab, January 1994. Submitted to Phys. Rev. Lett.

24. P. Avery et al. QQ MC event generator, June 1991. Fortran code and database table from CLEO collaboration.

25. M.S. Alam et al. (The CLEO Collaboration). Exclusive B decays to charm and charmonium final states. Submitted to Phys. Rev. D, August 1993.

26. F. Abe et al. (The CDF Collaboration). Search for $W' \rightarrow e\nu_e$ and $W' \rightarrow \mu\nu_\mu$ in $\overline{p}-p$ collisions at $\sqrt{s} = 1.8$ TeV. *Phys. Rev. Lett.*, 67:2609–2613, July 1991.

27. C. Anway-Wiese. Offline muon matching cuts. Technical Report 1986, CDF, March 1993.

28. Particle Data Group. Review of particle properties. *Phys. Rev. D*, 45:Part 2, June 1992.

29. F. Abe et al. (The CDF Collaboration). Measurement of $B^0\overline{B^0}$ mixing at the fermilab tevatron collider. *Phys. Rev. Lett.*, 67(24):3351–3355, December 1991.

VITA

VITA

Mark W. Bailey was born in Oklahoma City, Oklahoma on August 17, 1966. He attended Putnam City public schools until graduating in 1984. He was awarded several scholarships and chose to attend Oklahoma State University, where he received a Bachelor of Science degree in May of 1988, with majors in Physics and Mathematics. He then was offered a teaching assistantship at Purdue University and started in the Ph.D. program. After receiving a Masters degree in May of 1990, he joined the CDF collaboration at Fermilab as Arthur Garfinkel's graduate student. He completed his thesis while resident at Fermilab, and received his Ph.D. in May, 1994.